Department of Spatial Sciences

A Remote Sensing Assessment of Anthropogenic-induced Wetland Degradation of the Vietnam Mekong River Delta

Xuan Cuong Cao

This thesis is presented for the Degree of
Master of Philosophy (Surveying and Mapping)
of
Curtin University

September 2016

DECLARATION

To the best of my knowledge and belief this thesis contains no material previously published by any other person except where due acknowledgment has been made.

This thesis contains no material which has been accepted for the award of any other degree or diploma in any university.

Signature: .....

Date: 28/09/2016

ABSTRACT

Wetlands are one of the most important components that shape the natural landscape of the Vietnam Mekong River Delta (VMRD). The assessment of wetlands is important to effectively preserve and manage wetlands in the region. This requires a range of information that is often difficult to collect with ground-based surveys. Instead, remote sensing imagery acquired in the past provides the only existing records in both spatial and temporal dimensions, hence is used in this research to monitor the change of wetland in western VMRD over almost two decades. Synthetic Aperture Radar (SAR) and optical data integrated at a pixel-based level are used for mapping wetlands. In this study, three SAR images, namely ERS-2, ALOS PALSAR, and Sentinel 1, are fused with Landsat data using two hybrid methods of wavelet, namely PCA-wavelet and IHS-wavelet. In addition, full integration and weighted combination models are employed to inject spatial details extracted from SAR into optical data. The fusion results are compared to each other in terms of both statistical and visual analyses. The results of the better method are used to classify the wetland. The advantage of multi-sensor image fusion is confirmed through a comparison between maps of the wetland produced by using fused images and those by original MS images. In order to determine the change of the wetland from 1998 to 2016, the study implements the post-classification comparison method. The study period is divided into two: from 1998 to 2008 and from 2008 to the present. The change of wetland during each period is identified and then the annual rate of change is determined.

Floods play an important role in the formation of natural landscape in the delta. Floods provide water containing fertilized sediments that nurture wetlands in the delta. The question of how the change of wetlands affects natural flood extent is raised as its answer is important to successfully preserve and manage these wetlands. Landsat 5 TM and Landsat 8 OLI imagery, acquired during the flood season in 1999 and 2013 respectively, are employed to map flood-inundated wetland using a modified fuzzy c-means-based approach. The change of flood emergence in the two years is identified by overlaying the two flood inundated area maps. The results contribute to facilitating a thorough understanding of the impact of wetland change on flood extent.

The results show that for multi-sensor data fusion the PCA-wavelet method with full integration model of injection was the best since the fused results' spectral distortion was small with correlation coefficients in the 0.89 - 0.99 range. The classification accuracy of fused images confirmed the advantage of multi-sensor image fusion. Overall accuracy increases by from 2.88 to 13.09% and the kappa coefficient by from 0.11 to 0.14. A subsequent change detection analysis illustrated that grassland has been experiencing a significant loss of 71.9-78.5% of the study wetland since 1998, mainly due to the intensification and diversification of agriculture, forest plantation, and aquaculture. The decrease of grassland in the wetland has been going at an increasing rate from 7.2 to 9.8% corresponding to the conversion from intensification to diversification in agriculture.

It is found that the modified fuzzy c-means-based method produced a higher accuracy map of flood-inundated areas than the Maximum Likelihood method. Overall accuracy improved from 82.4 to 91.1 and the kappa coefficient from 0.6 to 0.9 The results show that the change of wetland due to agricultural activities led to 14.04 % of the wetland area not being inundated by floodwater.

ACKNOWLEDGEMENTS

Firstly, I would like to say thank you to the Australian Department of Foreign Affairs and Trading for generously offering me the Australian Awards Scholarship (AAS). The award gave me a wonderful opportunity to not only study in one of the best University but to also experience life in Australia. Thank you to the staff of AAS office in Vietnam and also to Curtin University's International Sponsored Student Unit for their kind supports throughout my study.

I want to express my gratitude to my supervisors, Dr Ashraf Dewan and Dr Todd Robinson at the Department of Spatial Sciences of Curtin University. Their advice from the beginning helped me in completing the thesis. I would also like to extend my thanks and gratitude to Ashty Salim for his help throughout the project. His provision of technical supports, his welcoming gesture and smiles helped me to solve many difficulties during the study. Through his support, I acquired better understanding of the application of remote sensing and GIS data processing techniques. Without his assistance, I would not have completed this thesis.

I say a big thank you also to Dr Nguyen Van Trung from Hanoi University of Mining and Geology, Nguyen Ba Duy from Vienna University of Technology. They not only provided me with SAR images, but they also supported me in processing the data. Thank you also to Kieu Duy Thong and Le Van Anh Cuong from the Department of Exploration Geophysics of Curtin University for their assistance with Matlab coding. Thank you also to Dr Hoang Cong Tin from Hue University for assisting me in the classification of images.

Finally, I would like to thank my wife Nguyen Thi Trang and my son Cao Truong An. Their patience and encouragement are the motivating factors behind my pursuit of a career in research.

TABLE OF CONTENTS

Declaration i
ABSTRACT ii
ACKNOWLEDGEMENTS iv
TABLE OF CONTENTS v
LIST OF FIGURES vii
LIST OF TABLES ix
Terms and Symbols xi
1. INTRODUCTION 1
1. 1 Background 1
1. 2 Problem statement 2
1. 3 Research objectives 3
1. 4 Study area 3
1.4.1 Description of the study area 3
1.4.2 Wetland vegetation in the study area 4
1. 5 Significances 5
1. 6 Organisation of the thesis 6
2 LITERATURE REVIEW 7
2. 1 Wetland change and flood extent in the study area 7
2.1.1 Wetland change monitoring 7
2.1.2 Flood monitoring 8
2. 2 Multi-sensor data fusion technique for wetland classification 9
2.2.1 SAR data for studying wetland 9
2.2.2 Optical data for studying wetland 10
2.2.3 Optical and SAR data fusion for studying wetland 11
3 DATA AND METHODOLOGY 13
3. 1 Materials 13
3.1.1 Satellite data collection 13
3.1.2 Ancillary data 16
3. 2 Methodology 18
3.2.1 Atmospheric correction of Landsat images 18
3.2.2 SAR image pre-processing 19
3.2.3 Speckle reduction of SAR images 20

3.2.4 Fusion schemes 21
3.2.5 Land cover classification and change detection of wetland 34
3.2.6 Flood mapping method 38
4 RESULTS 43
4. 1 Multi-sensor data fusion 43
4.1.1 Speckle suppression 43
4.1.2 Landsat 5 TM and SAR imagery (ERS-2 and ALOSPALSAR) fused results 46
4.1.3 Pansharpening MS images using the PAN-Sentinel 1 fused image 50
4. 2 Wetland change detection 53
4.2.1 Land cover classification using fused images 53
4.2.2 Wetland change over the period from 1998 to 2016 59
4.2.3 Flood extent change 63
5 DISCUSSIONS 71
6 CONCLUSIONS AND RECOMMENDATIONS 76
6. 1 Conclusions 76
6. 2 Recommendations 77
APPENDIX A 79
IMAGE FUSION MATLAB CODE 79
APPENDIX B 82
THE MODIFIED FUZZY C-MEANS MATLAB CODE 82
APPENDIX C 84
LAND CODES ON CURRENT LAND USE MAPS 84

LIST OF FIGURES

Figure 1.1 Location of the study area 4
Figure 1.2 Vegetation types in the Vietnamese Mekong River Delta..... 5
Figure 3.1 The research area overlaid by the footprints of satellite imageries 15
Figure 3.2 The DEM of the study area (data: SRTM) 16
Figure 3.3 Land use of Kien Giang province 2010 17
Figure 3.4 Flowchart of the study design..... 18
Figure 3.5 The processing flowchart for pixel-based fusion method (Pohl and Van Genderen, 1998)..... 21
Figure 3.6 Flowchart of the IHS fusion method 24
Figure 3.7 Flowchart of the PCA fusion method 25
Figure 3.8 IHS and Wavelet fusion method (modified after Hong et al., 2009)..... 28
Figure 3.9 PCA and Wavelet fusion method 30
Figure 3.10 Flowchart showing working procedure for mapping 1999 flood 41
Figure 3.11 Flowchart showing working procedure for mapping 2013 flood 42
Figure 4.1 Three test areas in SAR images 44
Figure 4.2 Speckle suppressed ALOS PALSAR image using the Gamma filter..... 45
Figure 4.3 Speckle suppressed Sentinel 1 image using the Gamma filter 45
Figure 4.4 Speckle suppressed ERS-2 image using the Median filter 46
Figure 4.5 Fused images of ERS-2 and Landsat 5 TM data 47
Figure 4.6 Fused images of ALOS PALSAR and Landsat 5 TM data 49
Figure 4.7 PAN-Sentinel 1 result fused by the ‘a trous’ wavelet method..... 51
Figure 4.8 Pansharpening results by the PCA-wavelet method using the PAN-Sentinel 1 fused image 52
Figure 4.9 Land cover classification 1998 (a) Fused ERS-2 and Landsat 5 TM data (b) Original Landsat 5 TM..... 56
Figure 4.10 Land cover classification 2008 (a) Fused ALOS PALSAR and Landsat 5 TM image (b) Original Landsat 5 TM 57
Figure 4.11 Land cover classification 2016 (a) Fused Sentinel and Landsat 8 OLI fused image (b) Original Landsat 8 OLI..... 58
Figure 4.12 Change of grassland: (a) 1998 - 2008 period (b) 2008 - 2016 period 62
Figure 4.13 Differences in NDVI..... 64
Figure 4.14 MNDWI calculated from Landsat 8 OLI images 65

Figure 4.15 Water cluster by MFCM 65
Figure 4.16 (a) Histogram of MNDWI and (b) MFCM-MNDWI results 66
Figure 4.17 Flood peaks in Tan Chau gauging stations during 1977-2000 (Le et al., 2007) 67
Figure 4.18 Peak flood inundation maps (a) 1999 and (b) 2013..... 68

LIST OF TABLES

Table 3.1 Characteristics of images used in this study 15
Table 3.2 Classification theme (Funkenberg et al., 2014) 34
Table 3.3 The sample of classes from ERS-2, Landsat 5 TM, and fused data 35
Table 3.4 The sample of classes from ALOS PASAR, Landsat 5 TM, and fused data 36
Table 3.5 The sample of classes from Sentinel 1, Landsat 8, and fused data 37
Table 4.1 Comparison of speckle suppression using different filtering techniques for SAR images 43
Table 4.2 Statistical evaluation of ERS-2 and Landsat 5 fusion 48
Table 4.3 Statistical evaluation of ALOS PALSAR and Landsat 5 TM fusion 50
Table 4.4 Statistical evaluation results of Sentinel 1 and Landsat 8 fusion 52
Table 4.5 Entropy information of images 53
Table 4.6 Confusion matrix 1998 – Classification using Landsat 5 TM images 54
Table 4.7 Confusion matrix 1998 – Classification using fused images 54
Table 4.8 Confusion matrix 2008 - Classification using Landsat 5 TM images 54
Table 4.9 Confusion matrix 2008 – Classification using fused images 55
Table 4.10 Confusion matrix 2016 - Classification using Landsat 8 images 55
Table 4.11 Confusion matrix 2016 – Classification using fused images 55
Table 4.12 Annual rate of land cover change (%) 59
Table 4.13 Land cover conversions between 1998 and 2008 (%) 60
Table 4.14 Land cover conversions between 1998 and 2008 (km^2) 60
Table 4.15 Land cover conversions between 2008 and 2016 (%) 61
Table 4.16 Land cover conversions between 2008 and 2016 (km^2) 61
Table 4.17 Flood-inundated matrix showing the change of flooded area during peak flood of 1999 and 2013 (%) 67
Table 4.18 Flood-inundated matrix showing the change of flooded area during peak flood of 1999 and 2013 (km^2) 67
Table 4.19 Confusion matrix of classifying flooded area by using the Maximum Likelihood method (%) 69
Table 4.20 Confusion matrix of classifying flooded area using the modified fuzzy c-mean MNDWI based approach 70

Table 4.21 Validation of the flood map of 1999 using the flood map produced by classifying pansharpened Landsat 7 ETM as reference 70

TERMS AND SYMBOLS

ALOS PALSAR	ALOS Phased Array Type L-band Synthetic Aperture Radar
AWT	'A trous' Wavelet Transform
BM	Bias of Mean
CC	Correlation Coefficient
CF	Calibration Factor
CS	Component Substitution
CSFCM	Conditional Spatial Fuzzy c – means
DEM	Digital Elevation Model
DN	Digital Number
ENVI	Environment for Visualising Images
ERS-2	European Remote Sensing satellite 2
FCM	Fuzzy c-mean
FI	Full Integration
IHS	Intensity-Hue-Saturation
Landsat OLI	Landsat 8 Operational Land Imager
Landsat ETM	Landsat Enhanced Thematic Mapper
Landsat TM	Landsat Thematic Mapper
LULC	Land Use and Land Cover
MBF	Modulation-Based Fusion
MFCM	Modified Fuzzy c-means
ML	Maximum Likelihood
MNDWI	Normalized Difference Water Index
MRA	Multiresolution Analysis
MRC	Mekong River Commission
MS	Multispectral
NDVI	Normalized Difference Vegetation Index
NDWI	Normalized Difference Water Index
NIR	Near-Infra Red
NM	Normal Mean
PAN	Panchromatic
PBSIA	Pixel-Based Spectral Image Analysis
PCA	Principle Component Analysis
RGB	Red, Green, and Blue
SAR	Synthetic Aperture Radar
SDD	Standard Deviation Difference
SI	Speckle Index
SLC	Single Look Complex
SRTM	Shuttle Radar Topography Mission
ToA	Top of Atmosphere
UTM	Universal Transverse Mercator
VMRD	Vietnam Mekong River Delta
WC	Weighted Combination
WGS-84	World Geodetic System 84

1. INTRODUCTION

1. 1 Background

Wetlands constitute one of the most productive environmental resources on the Earth's surface (Secretariat, 2013). They play a vital role in biodiversity (Secretariat, 2013) and make a large contribution to the water cycle and in regulating local water supply and quality (Russi et al., 2013). While wetlands cover 6% of the Earth's surface, they are disappearing at an alarming rate around the world (Mitsch, 2007). As a result, increasing attention is now being directed at recognising the importance of wetland ecosystems (Islam, 2008). Unfortunately, changes in the distribution of wetlands are not well recorded in many countries (Gong, 2010), which hinders effective management, protection and other intervention strategies (Wang et al., 2011). However, spatial analyses of their changing distribution through time can help recreate, restore and explain the potential anthropogenic impacts on these natural wetland systems (Zhou, 2010).

In Vietnam, the largest wetlands are in the Mekong River Plain, comprising an area of 4.9 million hectares (Do and Bennett, 2009). These wetlands are one of the most important components of the VMRD, because they provide a favourable environment for agricultural (e.g. rice), fishery, aquaculture and tourism activities (Renaud and Kuenzer, 2012). Agricultural production is considered to be the primary activity in the delta on which 17 million people depend for their livelihoods (Renaud and Kuenzer, 2012). Since the introduction of the reform program "Doi Moi" by the Government of Vietnam in 1986, the intensification of agriculture in VMRD has accelerated to ensure the nation's food security (Renaud and Kuenzer, 2012). However, the process of agricultural intensification, including the extension of canal systems and the changes in cropping pattern, from single crop to multiple systems, strongly influence the distribution of the wetlands (Renaud and Kuenzer, 2012). This is amplified by the Mekong Delta's flood protection system, which has caused a myriad of problems, including riverbank erosion, plant diseases, and a decline in soil fertility (Hung et al., 2014; Le et al., 2007). In addition, the delta is experiencing increased urbanization (Renaud and Kuenzer, 2012) which leads to the degradation of wetlands. While an obvious effect of these development activities are visible in VMRD area's wetlands distribution, relatively little is known about their qualification.

Annual floods from the Mekong River are one of the most crucial factors that contribute to the formation of landscape in the VMRD. Natural floods, which are neither extreme nor drought, are desirable as floodwaters contain nutrient-rich sediment fertilizing wetlands (Kuenzer et al., 2013). On the other hand, wetlands, considered as a giant sponge, absorb the extra floodwater and then mitigate the damage of floods. Moreover, they can protect land from erosion due mainly to floods (Chadde, 2006). It is clear that wetlands and floods have an interrelationship.

1. 2 Problem statement

Wetlands are an important component of the VMRD. Failure to protect wetlands will negatively affect the sustainable development of the region. Information about the change of wetlands in both spatial and temporal dimensions is required to support conservation and management activities of wetlands. Conventional methods such as ground survey and field data can be used to map wetlands in various settings; however, they are time consuming, costly, and labour-intensive. In contrast, remotely sensed imagery is a potential source for obtaining full coverage, repeatable, up-to-date and archived information that can be analysed at different periods to identify changes (Finlayson et al., 1998; Garg, 2013). Mapping wetlands using optical sensors requires cloud free images, which are difficult to obtain in tropical countries, such as Vietnam, and this problem is compounded by requiring multiple images for change detection. In addition, such environments as wetlands are complex as they concern generally small size vegetation patterns with low-spectral contrast among plant species (Moffett and Gorelick, 2013). This influences on the accuracy of classification. SAR, is not hindered by cloud cover and contains texture features, but lacks the spectral detail of optical sensors. Fusion of the two image sources is an effective way to incorporate the benefits from each data (Töyrä, 2002; Trung et al., 2013). However, there are various multi-sensor fusion methods and each of them produces results with different levels of quality. It is, thus, necessary to identify an appropriate fusion method.

Due to the reciprocal relationship between floods and wetland, the change of wetlands might affect the extent of flood. Remote sensing offers an effective approach for monitoring wetlands, mapping the inundation extent, and clarifying the impacts of wetland changes on the flood extent.

1. 3 Research objectives

Based on the above statement, the main objectives of this study are:

a. Identify and implement a suitable algorithm to fuse optical and radar imagery for improving the accuracy of classifying wetlands;
b. Quantify the spatial and temporal distribution of wetlands over the last two decades and identify the causes; and
c. Examine the impacts of wetland changes on the flood extent of the study area.

1. 4 Study area

1.4.1 Description of the study area

The study area is a part of the Ha Tien Plain, which belongs to the Kien Giang province located in the Western VMRD, shown as the red rectangular area in Figure 1.1. The site covers an area of about 1000 km^2, is known as the last remaining seasonally inundated grassland in the VMRD, and the area is designated as a Ramsar site (Buckton et al., 1999). Ha Tien is the border-gate economic town, so it plays an important role in the socioeconomic development of the region. There are many beautiful landscapes, such as Thach Dong Mountain, Dong Ho lagoon, Mui Nai Steep Stones, Mac Cuu village, Thien Tien Tu pagoda, Phu Dung pagoda, which are recognised as cultural relics by the Vietnamese State and UNESCO. In addition, the Dong Ho estuarine lagoon in the region constitutes the most important part of the western sea drainage program which is to drain flooding water from the Mekong River.

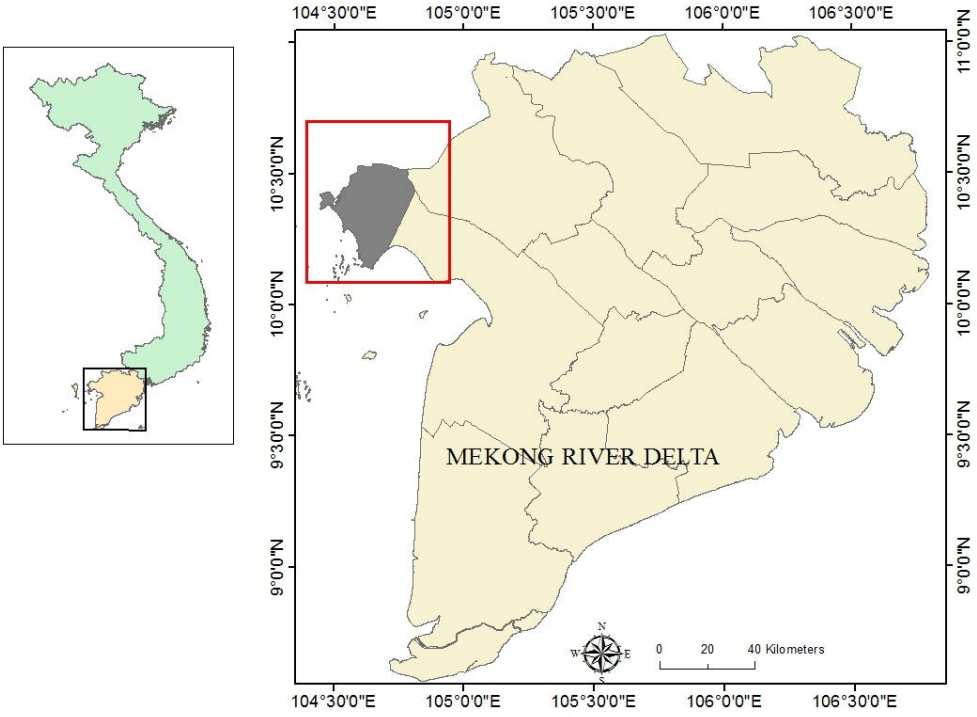

Figure 1.1 Location of the study area

The main topographic characteristic of the study area is that its terrain gently slopes towards the coast and covers the floodplain with up to 2 m water depth. The climate is characterized by the subtropical type with two seasons: dry season (from January to June) and rainy season (from July to December). Precipitation for the area averages from 1500 to 2500 mm per year.

1.4.2 Wetland vegetation in the study area

The study area is considered as a wetland with a high biodiversity consisting of brackish water lagoons, forests, karst hills and seasonally flooded pasture - a migration home for valuable and rare birds and animals.

In terms of wetland vegetation, the seasonal inundated grassland, one of main vegetation types in the area, comprises more than 90 grass and sedge species building a diversity of plant. *Eleocharis dulcis* community dominates the grassland (Fig 1.2 a), followed by a *Lepironia articulate* community (Fig 1.2 b). *Melaleuca* scrub is also popular in the site (Fig 1.2 c); this community includes 2-4 m tall trees which locally reach 10-12 m tall. In the brackish water zone, the aquatic palm *Nypa fruticans* dominated, reaching up to 8 m in height (Fig 1.2 d). Associated species include

Acanthus ebracteatus, *Derris trifolia*, *Clerodendrum inerme*, *Phoenix paludosa*, *Acrostichum aureum*, *Aglaodora griffithii* and *Cyperus malaccensis* (Buckton et al., 1999).

a. *Eleocharis dulcis*

b. *Lepironia articulate*

c. *Melaleuca forest*

d. *Nypa fruticans*

Figure 1.2 Vegetation types in the Vietnamese Mekong River Delta

(Source: (a) Richard A. Howard Photograph Collection; (b) Coromandel Native Nursery; (c) by Sinh Le; and (d) Hossain and Islam (2015))

The above ecosystem is home to many globally threatened bird species such as White-shouldered Ibis, Bengal Florican, Spot-billed Pelican, and the globally near-threatened Painted Stork. With the role of nurturing many globally vulnerable species, the seasonally inundated grassland becomes more valuable and highly conservative.

1. 5 Significances

This study is expected to contribute to the following areas:

1. Development of a technique for fusing optical and microwave remote sensing data applicable for accurate mapping of wetland areas;

2. The results of the research will provide accurate information on the spatiotemporal dynamics of wetland in VMRD. Further, the effect of human activities such as urbanization and agricultural intensification will be used to determine the factors driving such changes; and
3. The findings of the study are expected to significantly contribute to policy-making and sustainable development of wetlands.

1. 6 Organisation of the thesis

The thesis has six chapters with five main contents: introduction, literature review, data and methodology, results, and discussion and conclusion. The first chapter presents research background, objectives, significance, and thesis structure. In this chapter, the description of the study area is also provided. Chapter two provides an overview on previous studies on wetlands and floods employing remote sensing techniques. Several studies in which optical and SAR data were used individually or in combination are reviewed and referenced for proposing the methodology of this study. Chapter three has two main parts: data collection and methodology. The first part of this chapter consists of the characteristics of data, and acquisition date. In addition, ancillary data such as land use map, a Digital Elevation Model (DEM), and water level record are included. The methodology part presents optical and SAR image fusion methods, the classification of wetland using fused products, wetland change detection, and methods for mapping floods. For each section, a comparison between methods is undertaken in order to determine the best one. Chapter four presents the results of the study. Chapter five presents analyses and findings of the study. Chapter six concludes the thesis, restating the findings, significances and contributions. Recommendations for the future study complete the chapter.

2 LITERATURE REVIEW

2. 1 Wetland change and flood extent in the study area

Floods from Mekong River are important to wetlands in the region as they transpose water as well as nutrient-rich sediments and fertilisers contained in the floodwater. Wetlands also play an important role in mitigating the flood hazard. Therefore, investigations into the relationship between wetlands and floods in the VMRD is a very important issue.

2.1.1 Wetland change monitoring

Accurately mapping the distribution of wetlands and detecting their changes in both spatial and temporal dimensions have been a goal shared by science, management, restoration, and conservation. In the past, these activities were undertaken manually through laborious field surveys and manual techniques. Recently, information on wetlands can be obtained much more efficiently by using modern remote sensing technologies (Moffett and Gorelick, 2013). Wetlands in the VMRD play an important role in the sustainable development of the region. Therefore, monitoring the Mekong River's wetlands using remote sensing data has been attracting many scientists and managers. Phan and Jacques (2007) used topographical maps and SPOT data to determine the change of mangrove forests in the VMRD over 36 years (1965-2001). These authors pointed out that there was a decrease of 50% in the total coverage of mangrove forest over this period due to war, collection of firewood and clearing for agriculture, and shrimp farming. Another study conducted by Tong et al. (2004) utilized SPOT data to assess the evolution of mangrove forest in relation to extensive shrimp farming. The Mekong River Commission launched the project of mapping all wetlands in the lower Mekong River Basin, made up in part by Lao, Thailand, Cambodia, and Vietnam, using Landsat ETM + imageries (MacAlister and Mahaxay, 2009). Overall accuracy ranges from 77 to 94 % including wetland and non-wetland classes, but for the Vietnam's wetlands, including Tram Chim and Lang Sen, the classification accuracy is 75.8 % as the selection of a limited number of training areas was based on the analysts' experience. Funkenberg et al. (2014) determined the change of land cover types in the Ha Tien Plain using Landsat TM images. Their study shows that there was a significant loss of the area of seasonally inundated grassland in the Ha

Tien Plain over almost two decades from 1991. It was noted that the spatial resolution of Landsat 5 TM is not high enough to allow for the differentiation of land cover types with more details classes. In addition, the method used in above-mentioned studies was pixel-based classification which creates classes based on the spectral signature of each pixel. As wetlands normally contain many small size areas of vegetation with low-spectral contrast among plant species (Moffett and Gorelick, 2013) it is difficult to achieve high classification accuracy. The accuracy of change detection is questionable as the input images were acquired in different seasons. Normally, there are many changes in land cover types in different seasons.

2.1.2 Flood monitoring

In order to gain a deep insight about the impact of wetland changes on the flood extent, there is a need for mapping floods. With cost-effective and fast processing characteristics over a large area, remote sensing constitutes one of the most reliable and effective methods for observing the extent of floods and providing information for assessing the level of the damage caused compared to other methods such as ground-based surveys, hydrodynamic model prediction and statistics (Dao and Liou, 2015). Both optical and radar sensors are the main equipment used to collect remotely sensed data for flood monitoring (Feng et al., 2015). To some extent, radar data, such as SAR, has the advantage of weather independence to acquire and offers users clear scenes of the inundation extent (Henry et al., 2006; Mallinis et al., 2013). However, a limitation on the use of SAR images makes them expensive and unavailable for public use (Dao and Liou, 2015). In addition, it is difficult to map a peak flood utilizing SAR data as the data is rarely available at the time. Thus, detected inundated areas are either smaller or larger than those at the flood peak (Brivio et al., 2002).

In the VMRD, several studies were conducted to determine the flood regime and pattern using SAR data. Kuenzer et al. (2013) employed 60 ENVISAT ASAR Wide Swath Mode datasets from 2007 to 2010 to enable a deeper understanding of the flood patterns in the region. Although the study presented several findings on flood occurrence and flood progression over a large region, the accuracy of flood pattern derived from 150 m resolution images was not high enough to provide a deep insight into the relationship between a wetland area and floods. This is because many objects

such as small flooded patches within urban areas, agricultural areas, and aquaculture ponds could not be identified.

Optical data over flooded regions during peak flood is often covered with thick cloud which, in turn, makes it difficult to map the flood. However, cloud free images acquired several days after the receding of flood water can be used to identify previously inundated regions by assessing the differences in the spectral properties of the images acquired before and after the flood (Sakamoto et al., 2007). With rich spectral information, temporal optical data in cloud free conditions can be used to extract water accurately which in turn improves the accuracy of flood delineation. There are many common techniques used to derive water bodies such as digitizing through visual interpretation, density-slicing of a single band, supervised and unsupervised classification, and water index. Among these approaches, water index is the most common method for water extraction (Fisher and Danaher, 2013). Because of the enhancement of the discrepancy between water pixels and their neighbourhood pixels, water indices can enable differentiation of water and non-water surfaces (Yang et al., 2015). Meanwhile, mixed pixels are the main reasons for a decrease in the contrast between water and their various adjacent backgrounds. These pixels are common in the optical data of wetlands. It is necessary to tackle this problem in order to improve the accuracy of water detection if one uses the water index method. Among numerous optical data, Landsat series i.e., Thematic Mapper and OLI are great candidates to map floods as they are easily accessible and free of charge. There have been many studies in which Landsat data were used successfully to delineate flood events (Dao and Liou, 2015; Wang., 2004).

2. 2 Multi-sensor data fusion technique for wetland classification

2.2.1 SAR data for studying wetland

SAR data has been proven to be a useful and reliable source to obtain ground surface information on wetlands in all conditions of weather (Ozesmi and Bauer, 2002). Wetness and roughness, two important parameters for mapping wetlands, can be derived effectively from SAR imagery (Castañeda and Ducrot, 2009). Research on wetland has shown that SAR data are sensitive to biomass and the structure of flooded vegetation. There is a significant correlation between the back-scattering coefficient

in SAR images and leaf area index (LAI) as well as Normalized Difference Vegetation Index (NDVI) (Hirooka, Homma, Maki, & Sekiguchi, 2015). Inoue et al. (2002) pointed out that there is a strong correlation between LAI and fresh biomass with HH- and cross-polarization of the C-band and those of the L-band, respectively. Based on the result of rice mapping using ENVISAT ASAR, Yang et al. (2008) noted that HH polarization is more sensitive to the plant water content, and VV polarization is more sensitive to the plant structure and other attributes such as leaf, plant area, and vigour.

However, classification of a complicated environment like wetland using a single SAR image can often produce low accuracy due to the effect of speckle and the limited number of SAR wavelengths and polarizations in a single SAR scene (Hess et al., 1995).

2.2.2 Optical data for studying wetland

Optical remote sensing is suitable for monitoring changes in various land covers, particularly wetlands, owing to its crucial characteristics such as multiple resolution and multiple wavelengths (e.g., visible to near-infrared). Because of strong absorption of light in the near-infrared portion (800-1100 nm) of the electromagnetic radiation (EMR) by waterbodies, this portion of EMR is found to be highly useful to separate waterbody from other land covers such as dry soil, and vegetation. Also, mid-infrared (1600 – 1700 nm) is sensitive to the water content level in plants.

Several methods of combination such as the principal component analysis (PCA) and spectral indexes method have been common. For detecting the change of wetlands, the application of PCA to Landsat images was proven to be very useful (Munyati, 2004). Band 2, 4, and 5 of Landsat TM data were also used successfully for the assessment of the change of wetland in Kuala Terengganu (Ibrahim and Jusoff, 2009). Another example is the combination of band 2, 3 and 4 of ASTER data which has constituted one of the ideal band combinations for land use and land cover mapping (Mendoza et al., 2004). Index-based methods such as NDVI (Bartsch et al., 2009; Hope et al., 2003; Pelkey et al., 2003), Enhanced Vegetation Index (EVI), Vegetation Health Index (VHI), Soil Adjusted Vegetation Index (SAVI) (Ferreira and Huete, 2004), Normalized Difference Water Index (NDWI), the Water Index (WI) (Behera et al.,

2012; Ouma and Tateishi, 2006), and Modified Normalized Difference Water Index (MNDWI) (Sun et al., 2012; Xu, 2006) have been applied to extract wetlands from Landsat, SPOT and IRS data.

However, the drawback of optical data is that they depend on the weather, and cannot penetrate through the canopy of vegetation or cloud to observe surface conditions. Therefore, the calculation of these indices from optical sensors requires cloud free images, which are rarely achieved in tropical countries, including Vietnam.

2.2.3 Optical and SAR data fusion for studying wetland

While above disadvantages of both radar and optical data are inherent, the integration of them is an alternative approach because optical and SAR sensors obtain complementary information by working at discrete sections of the electromagnetic spectrum. One can obtain more accurate information for landscape classification through this multi-sensor fusion (Pohl and Van Genderen, 1998; Zhang, 2010).

Research on wetlands using optical and SAR fused products has been conducted. For example, the integration of Landsat ETM+ and Radarsat-1 was used to generate a detailed map of coastal wetlands of the Amazon region (Rodrigues and Souza-Filho, 2011). By comparing with the map produced using only Landsat ETM + data, the study reported that the integrated product provided additional information, which permits efficient identification and mapping of tropical mangrove wetlands. Another study comparing land cover classifications for Lago Grande de Curuai floodplain (Amazon, Brazil) based on single sensor images (Landsat TM or Radarsat-2) with multi-sensor dataset classification (Landsat TM and Radarsat-2) and image fusion classification (Landsat TM and Radarsat-2 fused images) was undertaken by Furtado et al. (2015). They noted that the multi-sensor classification method performed better than the fusion-based method due to the nature of the classification process. However, the reasons for this can be that the date of optical and SAR image acquisitions were much far from each other; and the fusion methods used in the study including the Intensity-Hue-Saturation (IHS) and Principal Component Analysis (PCA) based fusion methods were probably not appropriate or optimal to the given data.

In terms of grass-dominated wetlands, Castañeda and Ducrot (2009) found that fusion based methods obtained more accurate classifications than the optical and SAR integration using a multi-sensor approach. It is noted that the both methods' success possibly comes from the variances in hydrological patterns and the structure of vegetation in different study areas (Furtado et al., 2015).

Available literature suggests that IHS and PCA are useful fusing algorithms for these image types (Gonzalez-Audicana et al., 2004a). The rationale behind this is that both techniques linearly transform spectral information to new axes, and thus are suitable for separating the spatial information of multi-spectral images. While the IHS method has the disadvantage of only applying to three optical bands, PCA can be applied to all bands included in optical data. In addition, the latter can subdue redundant information present in multispectral data (Amolins et al., 2007). However, the high spectral distortion occurring in the resultant image is a drawback of both methods. Wavelet-based fusion methods are developed from the high pass filter method and can minimize the spectral distortions, but these methods are computationally intensive. Gonzalez-Audicana et al (2004) proposed to combine IHS and PCA images with the wavelet methods to fuse multispectral (MS) and panchromatic (PAN) data which are believed to result in a better outcome compared to any individual method.

3 DATA AND METHODOLOGY

3. 1 Materials

3.1.1 Satellite data collection

The multi-temporal, multisource and different resolution satellite images were used in this study to identify the spatial distribution and changes of protected wetland in the study area. A significant limitation on accessing optical data is due to the subtropical and maritime location of the study. For radar data, one ERS-2 band C image, one ALOS PALSAR, and one Sentinel 1 scene of the study area were acquired for three years 1998, 2008, and 2016, respectively (Table 3.1 and Figure 3.1). For optical data, Landsat 5 scenes recorded by the Thematic Mapper (TM) sensor and Landsat 8 scene were collected for 1998, 1999, 2008, 2013, and 2016. These images were saved in GeoTIFF format, in the UTM projection with WGS-84 datum.

3.1.1.1 ERS-2 data

The European Remote Sensing satellite 2 (ERS-2) launched in 1995 contains one synthetic aperture radar sensor using C- band frequency (5.3 GHz, bandwidth 15.5 ± 0.06 MHz) with VV polarization with the incident angle of 23^0. In this study, an ERS-2 image acquired in January 1998 (representing dry season) was merged with Landsat 5 TM. The fused product was used to classify wetland.

3.1.1.2 ALOS PALSAR data

The Phased Array Type L-band Synthetic Aperture Radar (PALSAR) carried by ALOS satellite is the L-band frequency microwave sensor to obtain all weather condition land observation. There are three modes in the PALSAR sensor namely Fine mode, Polarimetric mode, and ScanSAR mode.

The ALOS PALSAR image of this study is a raw image obtained from JAXA. The image is HH single polarization FBS mode with a spatial resolution of 15 metres acquired on 17^{th} May 2008 in the end of the dry season.

3.1.1.3 Sentinel 1 data

Another C-band data used in this research is Sentinel 1 image. Sentinel 1 is an initiative for the Copernicus by the combined forces of the European Space Agency (ESA) and

the European Commission (EC). The mission consists of two satellites, Sentinel 1A and Sentinel 1B, with the same orbit (European Space Agency, 2014).

In this study one Sentinel 1 image over the study area was collected and utilized with the purpose of wetland classification. The scene acquired on 2nd January 2016 was merged with Landsat 8 OLI.

3.1.1.4 Landsat data

Landsat TM imagery consists of seven multispectral bands with a spatial resolution of 30 metres. Landsat 8 Operational Land Imager (OLI) was launched in 2013. Its product consists of eight multispectral images, one panchromatic band, and two thermal bands with 30, 15, and 100 metres spatial resolution, respectively. In this study, while Landsat 5 TM scenes were used for two aims: mapping flood of 1999 and wetland classification for the years 1998 and 2008, Landsat 8 OLI imagery were used for the same aims but for 2013 and 2016.

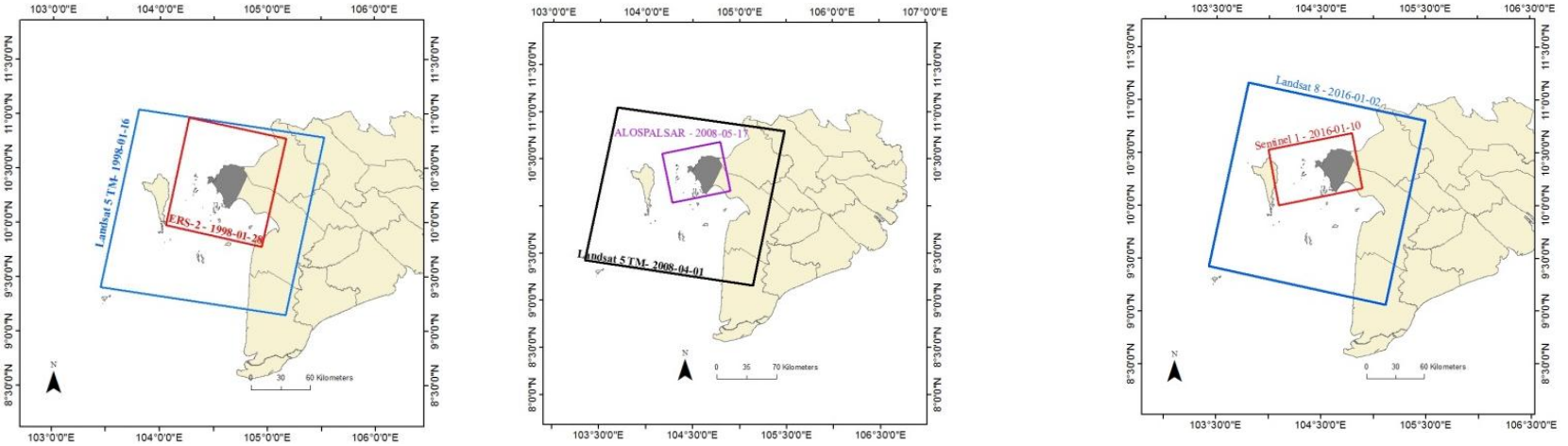

a. Year 1998 b. Year 2008 c. Year 2016

Figure 3.1 The research area overlaid by the footprints of satellite imageries

Table 3.1 Characteristics of images used in this study

	1998		2008		2016	
	Landsat 5 TM	ERS-2	Landsat 5 TM	ALOSPALSAR	Landsat 8	Sentinel 1
Acquired Date	16th Jan	28th Jan	1st April	17th May	10th Jan	2nd Jan
Sensor	Thematic Mapper	ERS-2	Thematic Mapper	PALSAR/FBS	Operational Land Imager	C-SAR
Spatial resolution	30 m	25 m	30 m	12 m	30 m	20
Flight direction		Descending		Ascending		Descending
Polarization		VV		HH		VV-VH
Swath	185 km	100 km	185 km	80 km	185 km	250 km
Incident angle	98.2°	23°	98.2°	41.5°		98.18°

3.1.2 Ancillary data

Further to the abovementioned satellite data, a Digital Elevation Model (DEM) (Figure 3.2) derived from the Shuttle Radar Topography Mission (SRTM) with a resolution of approximately 90 m, version 4.1, in Geotiff format and featured in the UTM projection with WGS-84 datum was used to mask out non-flood area, and remove terrain effect error in SAR data. The SRTM DEM was resampled to a spatial resolution of 30 m to extract flood-water. Weekly water levels recorded during the rainy season in 1999 and 2013 at the Tan Chau and Chau Doc gauging stations were provided by the Mekong River Commission (MRC). The data were measured as above the mean sea level in Ha Tien.

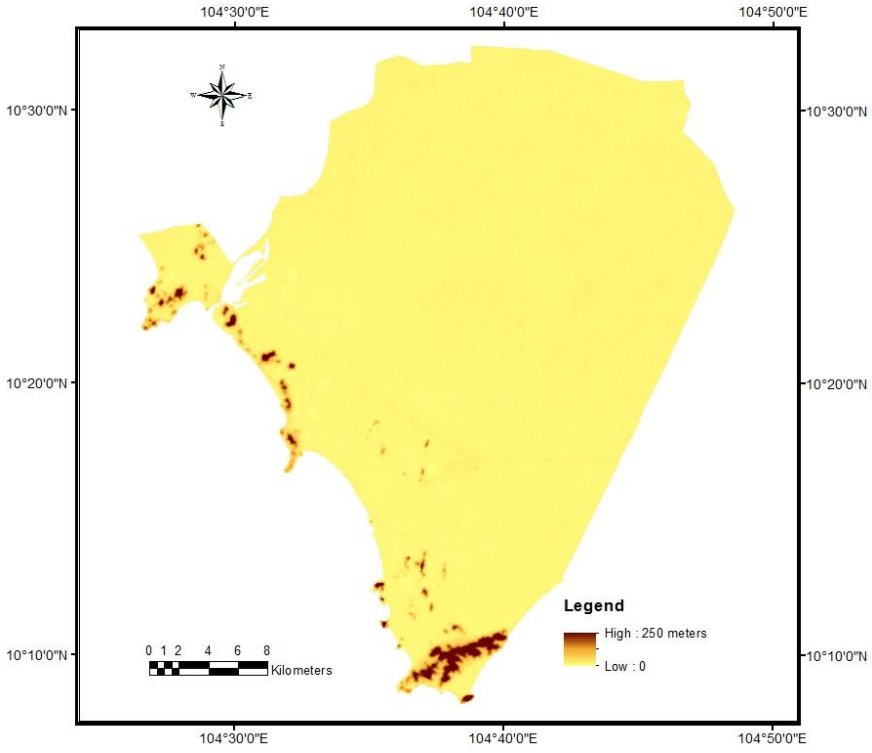

Figure 3.2 The DEM of the study area (data: SRTM)

The high resolution Google Earth images and the land use map of Kien Giang province in 2010 with a scale of 1:100,000 (Figure 3.3) provided by the Department of Environment and Natural Resources in Kien Giang were used to define areas of interest that represented the main types of land cover in the study area. The data was also employed for the validation of land cover classification and flood mapping.

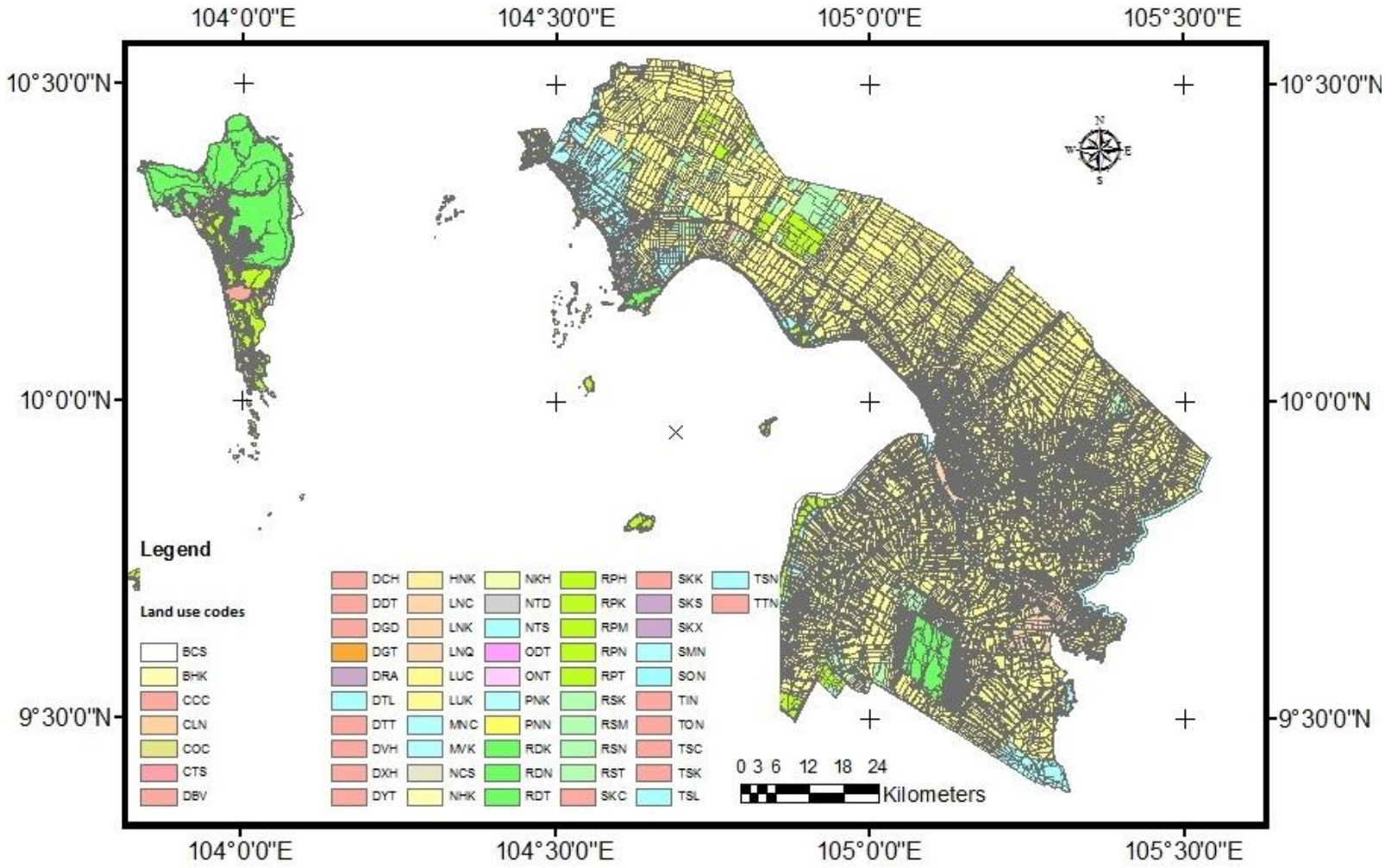

Figure 3.3 Land use of Kien Giang province 2010

3. 2 Methodology

The general process of workflow of this study is described below (Figure 3.4).

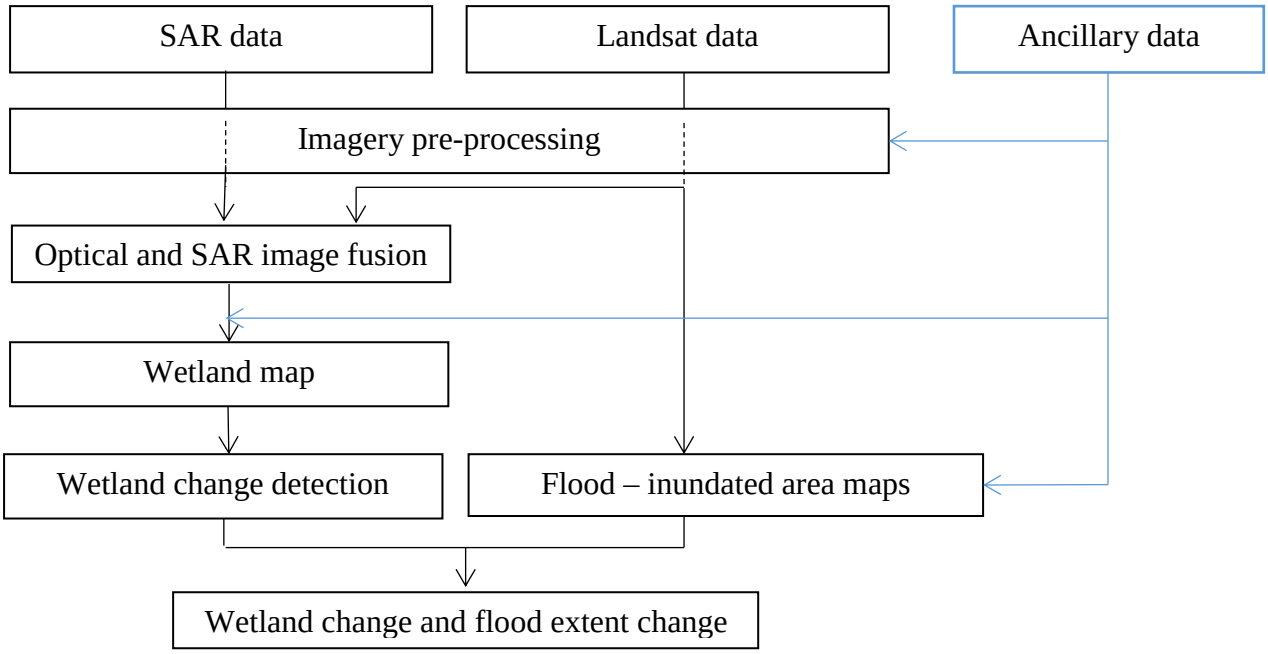

Figure 3.4 Flowchart of the study design

3.2.1 Atmospheric correction of Landsat images

As a large percentage of Landsat images normally suffers from significant contamination due to aerosols, clouds, and cloud shadows (Liang et al., 2001), the removal of these effects are necessary (Pohl and Van Genderen, 1998). There have been many techniques used in the atmospheric correction such as dark-object, histogram matching, and invariant-object methods. The dark-object constitutes the most common method in atmospheric correction (Kaufman and Sendra, 1988; Kaufman et al., 1997; Liang et al., 1997; Popp, 1995; Teillet and Fedosejevs, 1995; Thome et al., 1998). In this research, the dark-object method is implemented for the atmospheric correction of Landsat 5 TM and Landsat 8 OLI images using ENVI software (v.5.0). Before performing atmospheric calibration, all images are geocoded to UTM projection (zone 48) and transformed to digital numbers.

Atmospheric calibration contains two steps: (1) Converting Landsat digital number (DN) to Top of Atmosphere (ToA) reflectance; (2) Dark-object subtraction.

The process of converting DN to the ToA reflectance is to minimize the variance caused by differing solar zenith angles and incident solar radiation with the assumption

of Lambertian surface (Danaher et al., 2001). The equations of DN to ToA reflectance conversion are given as:

$$L_\lambda = \alpha_\lambda DN + \beta_\lambda \; W/(m^2 sr \mu m) \quad (3.1)$$

Where L is radiance values, α_λ and β_λ are calibration coefficients.

$$\rho_\lambda = \pi d^2 L_\lambda / E_{0\lambda} \; cos\theta_S \quad (3.2)$$

Where ρ is the reflectance,

L_λ radiance as a function of bandwidth,

$E_{0\lambda}$ exoatmospheric irradiance,

θ_s solar zenith angle.

3.2.2 SAR image pre-processing

For initially processing raw SAR data, there were several steps, i.e., focusing, multi-looking, noise suppression, and radiometric and geometric calibration. In the first step, the energy of a point target response is compressed in both azimuth and range directions. The result of this step is a single look complex (SLC) data. The two following steps are to reduce noises in the SLC data. The final step is to perform the absolute image calibration and derive the radar backscattering coefficient.

There are three backscattering coefficients, namely beta nought (β^o), sigma nought (σ^o) and gamma nought (γ^o). The latter best expresses the amount of ground actually visible to a radar antenna. The formula of gamma nought is given as follows:

$$\gamma^o = 10. log_{10}\langle I^2 + Q^2 \rangle + CF - A \quad (3.3)$$

where I and Q are the real and imaginary parts of the SLC product. A is the conversion factor. CF is calibration factor.

Geometric calibration for SAR data is the conversion of SAR data either slant range or ground range geometry into a map coordinate system. It is noted that the only way to geocode SAR data is by applying a range-Doppler approach. One might choose ellipsoidal geocoding without the use of Digital Elevation Model (DEM) data or terrain geocoding with the use of DEM data. For precise geocoding the following information were employed:

- Ground control points
- Orbital parameters (positions and velocities)

- Processed parameters (i.e Doppler, range delay, pixel spacing)
- DEM

All the SAR data in this study were processed through the SARScape software.

3.2.3 Speckle reduction of SAR images

SAR images are the result of coherent processing of the scattered signals which also causes speckle effects. Speckle is a multiplicative noise which has a negative impact on the image interpretation and target classification (Nyoungui et al., 2002). In the process of fusing SAR and optical imageries, many techniques are used to despeckle the SAR image to circumvent the integration of speckle noise into optical images. Multiple-look processing is a well-known method in the reduction of speckle, but this method leads to the degradation of spatial resolution for the resulting images. Digital image processing-based methods such as Median filter (Richards, 2013), Local Region filter (Nagao and Matsuyama, 1979), Lee's sigma filter (Lee, 1983), Frost (Frost et al., 1982), and Gamma (Lopes et al., 1990) have been used frequently in suppressing speckle of the SAR image. In order to find an appropriate filter for the SAR data in this study, a critical survey and comparison of above-mentioned methods were undertaken.

Filters were implemented on each SAR image. The normalized mean (NM) and speckle index (SI) were used to observe the preservation of mean and the speckle suppression performance (Huang et al., 2009; Nyoungui et al., 2002). The normalized mean is formulated as:

$$NM = \frac{\mu_{filter}}{\mu_{ori}} \tag{3.4}$$

where μ_{ori} and μ_{filter} are the mean of the original and filtered image, respectively.
The ideal value of *NM* is one, which means the filter obtains a perfect preservation of mean in homogeneous area.
The SI is computed by the following equation:

$$SI = \frac{\sigma}{\mu} \tag{3.5}$$

where σ and μ are the mean and standard deviation of the filtered image. The smaller the *SI* is, the better speckle removal.

3.2.4 Fusion schemes

Multi-sensor image fusion, known as the process of combining information acquired from different image sensors, is to get a more comprehensive interpretation of scene than either of the input data (Zhang, 2010). According to Pohl and Van Genderen (1998), pixel based fusion is the most common method. The pixel-based multi-source fusion technique, is the integration of the most original data from multiple sensors into single resolution data, and has the advantage of avoiding loss of information. The purpose of pixel-level fusion is to boost the textural and structural detail, improve the spatial resolution and maintain the original data's spectral fidelity concurrently (Zhang, 2010). Figure 3.5 shows the overall processing flowchart for merging images at pixel level.

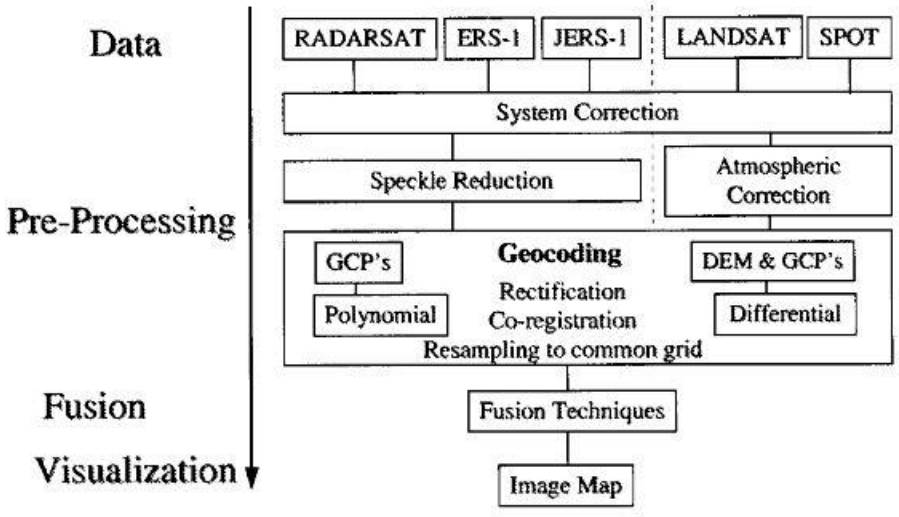

Figure 3.5 The processing flowchart for pixel-based fusion method (Pohl and Van Genderen, 1998)

In general, there are three categories of the pixel-based fusion: modulation-based fusion (MDF), multiresolution analysis-based fusion (MRA), and Component substitution (CS) (Zhang, 2010). In the CS method, firstly, linear transformation of the MS data set into more uncorrelated vector space is implemented. In the second step, one transformed band is replaced by a high resolution image. Finally, fused images are the result of the inverse transformation into the original space. Several well-known CS techniques are the Intensity-Hue-Saturation (IHS), principle component analysis (PCA), and Gram-Schmidt (GS). The fused MS image using the MDF method is computed by the following equation (Zhang, 1999):

$$MSP_i = Pan_H \frac{MS_{Li}}{Pan_{LSyn}} \quad (3.6)$$

Where MSP_i is the band i of the fused high resolution image, Pan_H is the high resolution image; Pan_{LSyn} is the low resolution version of the Pan_H simulated to the low resolution MS bands.

There are several examples of the MDF method such as high-pass filter, Brovey and synthetic variable ratio. Regarding the MRA method, the input images are decomposed with different levels, and then the spatial details are derived and injected into finer scales of the MS images. The fusing process ends with the inverse multiresolution transform to get fused MS images. There are several multiscale decompositions such as wavelet, Laplacian pyramids, and bi-dimensional empirical mode.

It is worth noting that because of increasingly complicated high resolution and multi-source data, individual fusion technique cannot achieve good results. Therefore, many hybrid methods of above-mentioned techniques have been developed to improve fusion performance (Zhang, 2010). These include the hybrid methods of wavelet transform and IHS (Chibani and Houacine, 2003; Gonzalez-Audicana et al., 2004b; Hong et al., 2009), or PCA transform (Gonzalez-Audicana et al., 2004b; Shah et al., 2008).

3.2.4.1 Intensity – Hue – Saturation (IHS) fusion scheme

The IHS colour space consists of three components: Intensity, Hue and Saturation. Intensity is a measure of brightness, ranging from 0 to 1. Hue is the colour, measured as the angle around a colour wheel, while saturation is the amount of colour with the value ranges from 0 to 1 (Amolins et al., 2007). The IHS fusion method is based on the IHS transform to convert a spectral image from Red, Green, and Blue (RGB) space to IHS colour space before the Intensity band is replaced by the high spatial resolution image, i.e., panchromatic (PAN), histogram matched to the Intensity band. The method ends with the application of inverse transformation. There are several IHS models, but in general the best one is with the intensity calculated as (Nunez et al., 1999):

$$I = (R+G+B)/3 \quad (3.7)$$

Two scenes over the same location, obtained under different atmosphere conditions or global illumination, or different sensors, can be normalized through a technique called histogram matching (Gonzalez and Woods, 2002). This process is undertaken on the PAN image to match its mean and standard deviation to those of the intensity (Byun et al., 2013).

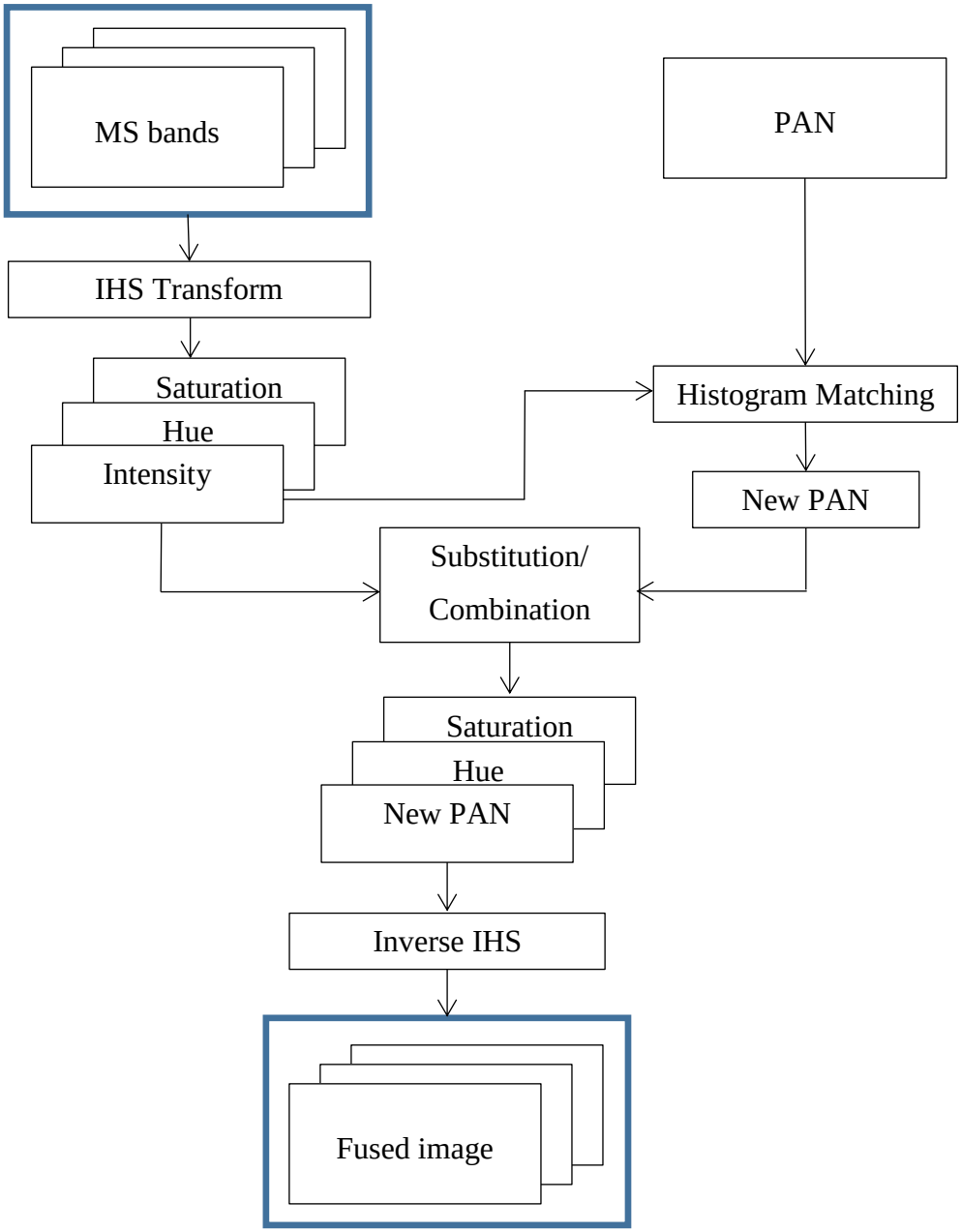

Figure 3.6 Flowchart of the IHS fusion method

3.2.4.2 Principle Component Analysis (PCA) fusion scheme

While the IHS method can be implemented to only three spectral bands at a time, the PCA can be utilized to merge more than three bands. In addition, redundant information due to the similar behaviour of land cover types in adjacent spectral bands can be organized in the way that all output bands are uncorrelated (Amolins et al., 2007).

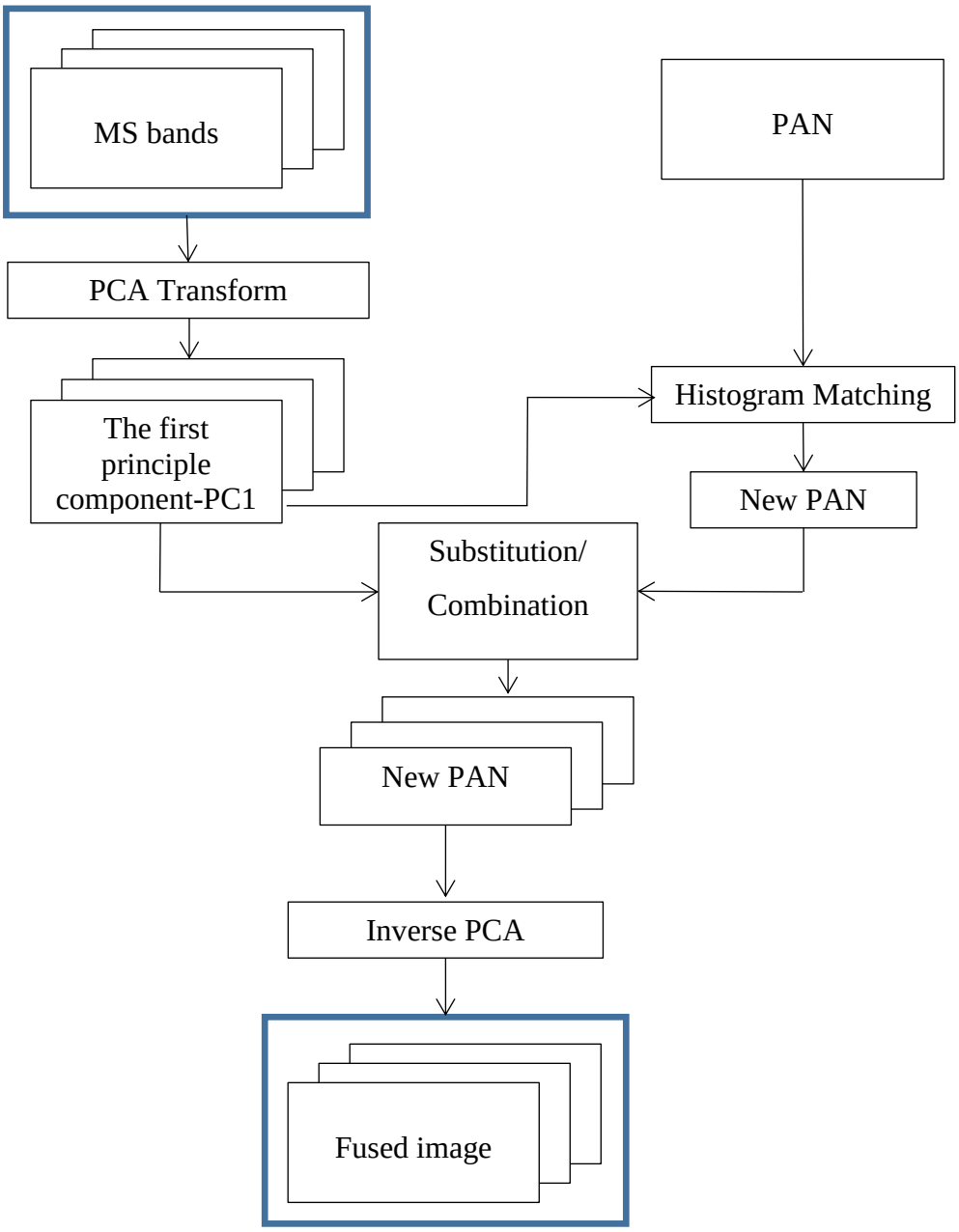

Figure 3.7 Flowchart of the PCA fusion method

The flowchart (Figure 3.7) shows that the PCA method is very similar to the IHS method but the PC1, which contains most of the information, is replaced or combined with a PAN image.

3.2.4.3 Wavelet fusion scheme

The wavelet fusion method is a technique based on multi-resolution analysis. The method utilises a wavelet transform to split each image's spatial information into many bandpass channels. Spatial information is contained in high-frequency channels. The wavelet transform is used to decompose multispectral (MS) images and the PAN image. The spatial information is then extracted from the PAN decomposition and is injected into that of MS decomposition prior to applying an inverse transform. One might be using one of the two algorithms to apply the wavelet transforms: decimated algorithm or un-decimated algorithm. After each level of decomposition, the decimated algorithm downsamples an image which is a two-dimensional signal to half the original resolution and a quarter of the original size. If the un-decimated algorithm is used, instead of down-sampling like the decimated one, after each level of transformation this algorithm up samples the image by inserting zeros between wavelet coefficients. This helps to keep the transformed results the same size as the original image. The injection of the spatial information of the PAN image into MS images might be performed by using an addition or a substitution model. Research on different wavelet algorithms and injection models has supposed that the un-decimated algorithm and additive models are better with no addition of artifacts and better preservation of original images' information (Amolins et al., 2007; Nunez et al., 1999).

In this study, 'a trous' wavelet transform (AWT) (Dutilleux, 1989), the un-decimated algorithm, is implemented for image fusion. In the process of decomposing the signal having finite energy into multiple chanels, the transform offered good localization in both frequency and space domains (Nunez et al., 1999). It uses a single wavelet function which creates a single wavelet plane at each scale (Chibani, 2007). As the AWT is performed on the image without decimation, the original image's dimensions are retained in the sucessive wavelet planes. The AWT allows the low-frequency information (approximation) of an image F to be separated from high-frequency information (wavelet coefficients or details) (Chibani, 2007):

$$F = F_N + \sum_{j=1}^{N} w_j\,(f) \tag{3.8}$$

Where F is an image. F_N corresponds to the last approximation plane and $w_j(f)$ is the wavelet coefficient computed at scale j. N represents the number of decomposition scales. The primary benefit of the AWT is in the computation of the wavelet coefficients for each location, which permits a better characterization of an image's features.

3.2.4.4 Hybrid image fusion methods based on wavelet transform for Landsat 5 TM and SAR imageries

a) IHS - Wavelet fusion method

The IHS and wavelet fusion method proposed by (Hong et al., 2009) is implemented to merge SAR and Landsat 5 TM imageries. However, instead of using decimated algorithm the 'a trous' algorithm is used to apply the wavelet transform action. The process is shown in Figure 3.8:

Step 1: perform co-registration of both images, resample the Landsat 5 TM to get the spatial resolution equal to that of the SAR image;
Step 2: apply the IHS transform to the Landsat 5 TM images to get the intensity band, then perform histogram matching between the intensity and the SAR image;
Step 3: apply 'a trous' wavelet decomposition to both the intensity and histogram matched SAR images. As a result, from each the intensity or histogram matched SAR, one approximation plane (A) and three detail planes (D_i) are obtained;
Step 4: inject wavelet coefficients extracted from the SAR decomposition into the intensity band by a weighted combination model; and
Step 5: perform inverse AWT and inverse IHS to achieve the fused images.

The weighted combination model can be expressed as:

$$A^{I+S} = w_1.A^I + w_2.A^S \quad (3.9)$$

where A^{I+S} is the new approximation band of the histogram-matched SAR. A^I and A^S are the approximation band of the intensity and the histogram-matched SAR, respectively, and w_1 and w_2 are the corresponding weight coefficients, which are expressed as follows:

$$w_1 = corr(\frac{A^I}{A^S}) \text{ , } w_2 = 1 - w_1 \quad (3.10)$$

where $corr(\frac{A^I}{A^S})$ is the correlation coefficient between A^S and A^I.

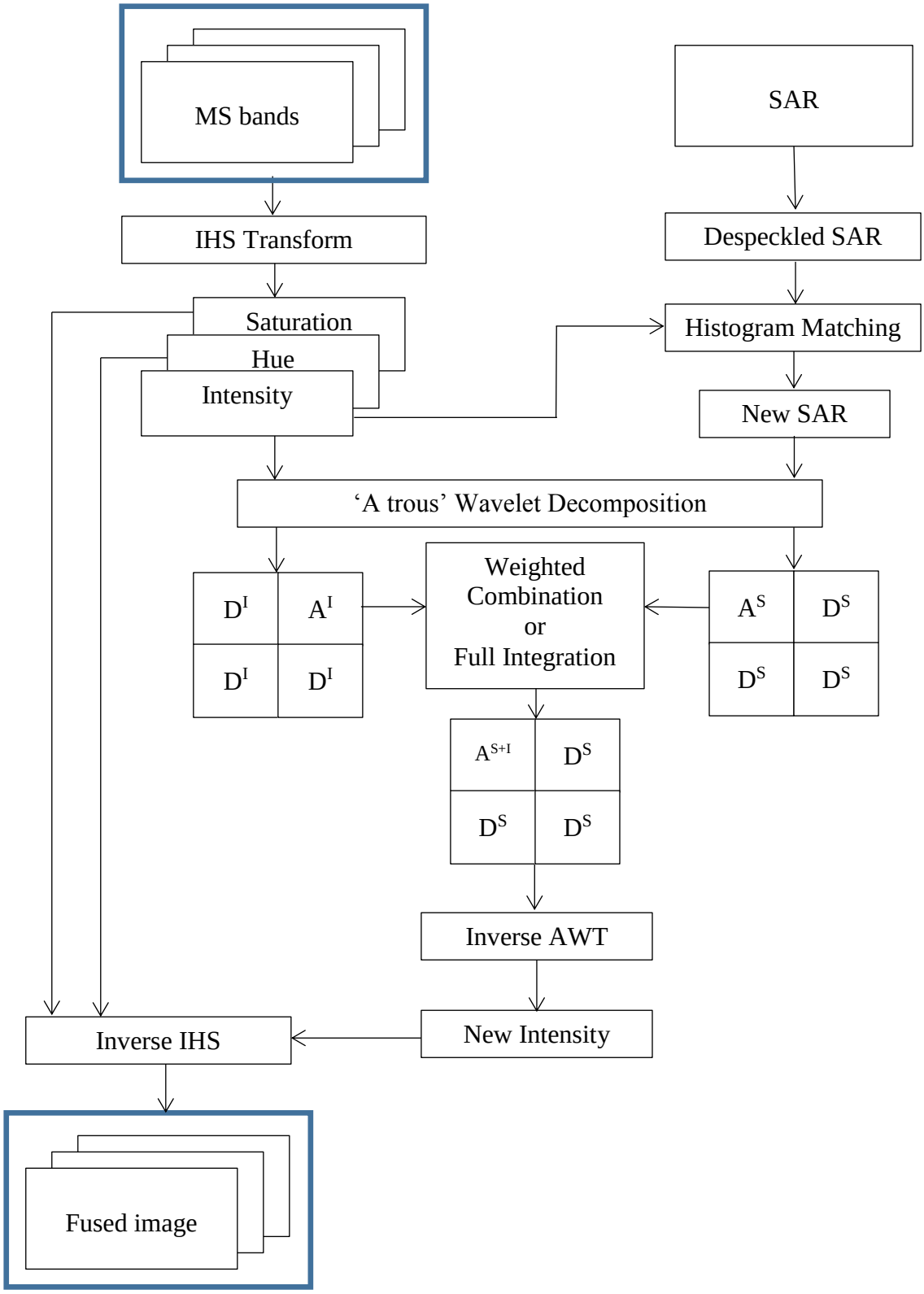

Figure 3.8 IHS and Wavelet fusion method (modified after Hong et al., 2009)

b) PCA - Wavelet fusion method

The PCA and wavelet fusion scheme proposed by (Gonzalez-Audicana et al., 2004b) is used in this study. There are several steps to fuse SAR and Landsat 5 TM images:

Step 1: perform co-registration of both images, resample the Landsat 5 TM to get the spatial resolution equal to that of the SAR image;

Step 2: apply the PCA transform to the Landsat 5 TM images to get the PC1 image, and then perform histogram matching between PC1 and SAR images;

Step 3: apply 'a trous' wavelet decomposition to both the PC1 and histogram matched SAR images. As a result, from each of the PC1 or histogram matched SAR image, one approximation plane (A) and three detail planes (D_i) are obtained;

Step 4: inject wavelet coefficients extracted from the SAR decomposition into the PC1 band by a weighted combination model or a full integration model. The former is to avoid an over injection of the PC1 information, whereas the latter is to improve the separability of classes;

Step 5: perform inverse AWT and inverse PCA to achieve fused images.

The weighted combination model can be expressed as:

$$A^{PC1+S} = w_1 . A^{PC1} + w_2 . A^S \quad (3.11)$$

where A^{PC1+S} is the new approximation band of the histogram-matched SAR, and A^{PC1} and A^S are the approximation band of the PC1 and the histogram-matched SAR, respectively, and w_1 and w_2 are the corresponding weight coefficients, which are expressed as follows:

$$w_1 = \frac{S_2^2}{S_1^2+S_2^2}, w_2 = \frac{S_1^2}{S_1^2+S_2^2} \quad (3.12)$$

where S_1, S_2 are standard deviation of A^{PC1} and A^S, respectively.

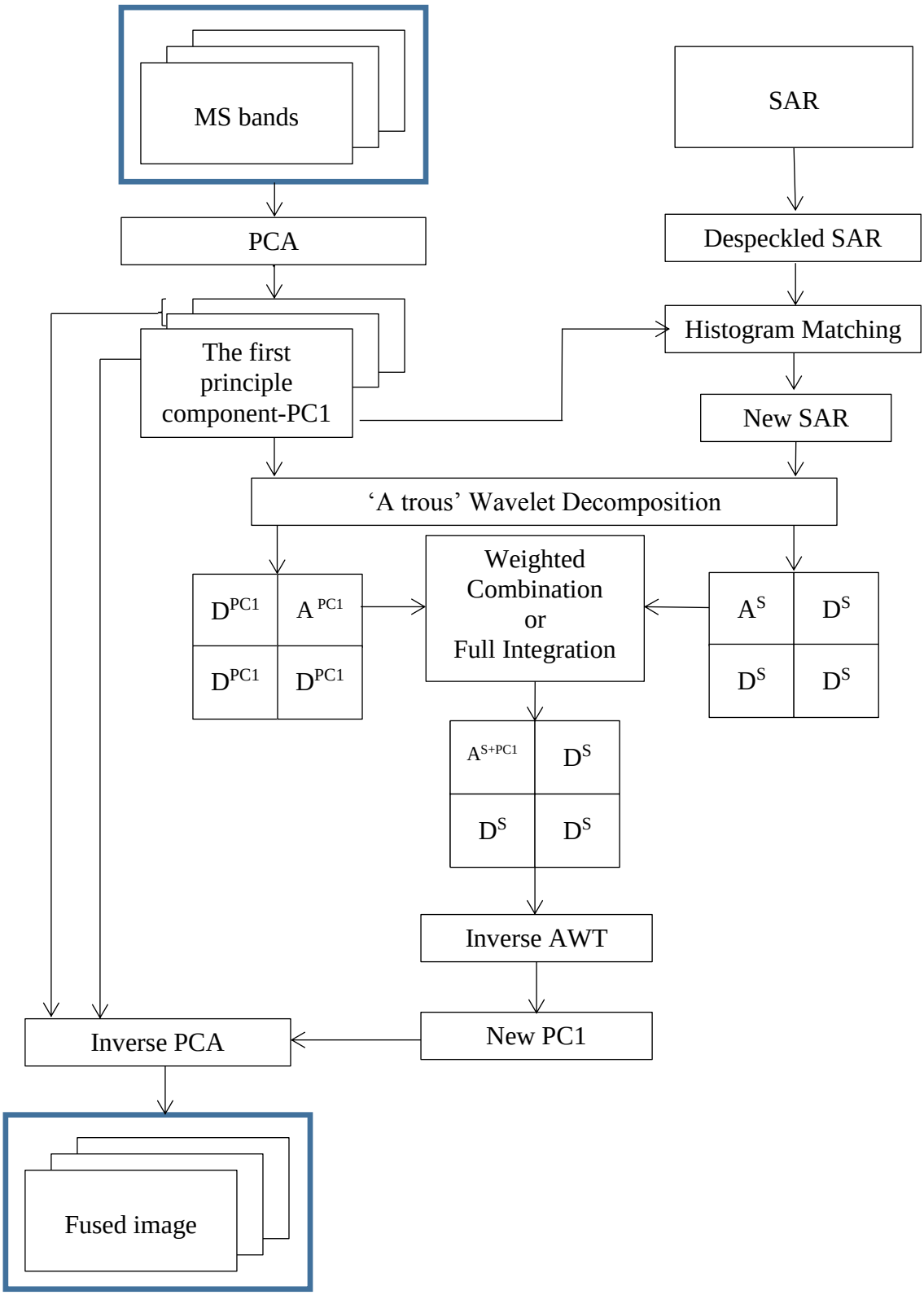

Figure 3.9 PCA and Wavelet fusion method

3.2.4.5 Hybrid image fusion method based on wavelet transform for Landsat 8 and Sentinel 1 images

Landsat 8 has one panchromatic band with the spatial resolution of 15 m, so the integration of Landsat 8 and Sentinel 1 images includes two major steps as follows:

- PAN and Sentinel 1 combination
- Pansharpening the MS images using the PAN-Sentinel 1 fused image

a) Integration scheme of PAN and Sentinel 1 images

The PAN and Sentinel 1 images are merged using the 'a trous' wavelet fusion method. The whole procedure contains several steps given as follows:

- Firstly, apply histogram matching using the formula 3.20 to match the histogram of the Sentinel 1 to that of the PAN image.
- Secondly, apply the AWT to decompose both Sentinel 1 and PAN images, with two levels of decomposition.
- Thirdly, perform an integration of the approximation band of Sentinel 1 and that of the PAN using one of two models such as the weighted combination model expressed by formula 3.13, and the full integration model.
- Finally, apply an inverse AWT to achieve a fused image.

As the result of 'a trous' wavelet decomposition, four planes are obtained including the last approximation and three detail plains. The last approximation plane (A) is the smoothest version of the input image as all details have been filtered out by repeated averaging (Chibani and Houacine, 2003). Firstly, the construction of the approximation plane of the fused image (A^{PAN+S}) is undertaken. This is an integration of PAN and Sentinel 1 approximation planes including A^P and A^S respectively, using an appropriate choice. Chibani and Houacine (2003) proposed three choices:

- $A^F = A^{PAN}$ for improvement of the PAN image.
- $A^F = A^S$ for improvement of the Sentinel 1 image.
- $A^{PAN+S} = ½(A^{PAN} + A^S)$ for the case that both input images are taken by the same sensor, but it cannot be applied for this situation as PAN and Sentinel 1 are acquired from different sensors.

In order to achieve an improvement of both the PAN and Sentinel 1 images, this study used a model based on the standard deviation of input images. The model can be expressed as follows:

$$A^{PAN+S} = w_1.A^{PAN} + w_2.A^S \quad (3.13)$$

where w_1 and w_2 are the corresponding weight coefficients, which are expressed as follows:

$$w_1 = \frac{S_2^2}{S_1^2+S_2^2}, w_2 = \frac{S_1^2}{S_1^2+S_2^2} \quad (3.14)$$

where S_1, S_1 are standard deviation of A^S and A^{PAN}, respectively.

Secondly, the construction of fused images' detail planes is performed using a suitable integration rule. The fusion rule plays a key role as it defines the quality of the fusion (Chibani and Houacine, 2003). The construction of fused images' detail planes is expressed:

$$D_j(PAN+S) = Rule(D_j(PAN), D_j(S)) \quad (3.15)$$

where D_j is wavelet coefficients in detail planes.

There are several rules such as full integration and the weighted wavelet coefficients (Chibani, 2007).

The full integration consists of injecting concurrently features extracted from both PAN and SAR into the fused result. Its formula is quite simple as follows:

$$D_j(PAN+S) = D_j(PAN) + D_j(S) \quad (3.16)$$

If one wants to avoid a bias in the fusion, the weighted wavelet rule is an appropriate choice. This rule takes into account of the relative importance of PAN and Sentinel 1 features. This can be formulated as follows:

$$D_j(PAN+S) = \alpha_j.D_j(PAN) + (1-\alpha_j).D_j(S) \quad (3.17)$$

where the parameter α_j indicates the relative importance of PAN and Sentinel 1 features. It can be expressed as:

$$\alpha_j = \frac{M_j(PAN)}{M_j(PAN)+M_j(S)} \quad (3.18)$$

M_j is an importance measure computed within a window (R) sliding cross whole each detail plane. It can be formulated as:

$$M_j(D_j) = \frac{1}{\#R}\sum_{(x,y)\in R} D_j^2(x,y) \quad (3.19)$$

Histogram matching's formula is expressed as:

$$S_H = \frac{\delta_{PAN}}{\delta_{Sen}}(Sen - \mu_{Sen}) + \mu_{PAN} \quad (3.20)$$

where S_H is the histogram-matched Sentinel 1 image; Sen is Sentinel 1 image; μ_{Sen} and μ_{PAN} are the standard deviations of the Sentinel 1 and PAN images, respectively.

3.2.4.6 Statistical evaluation of fusion performance

The evaluation of fusion performance is in both visual and quantitative (Alparone et al., 2007). Two of the most crucial criteria in fusion assessment are the spectral and spatial effects of the fused products. The closer the colour of the fused image is to that of the original MS image, the better performance of the fusion approach in terms of the spectral effect and the more details the fused image illustrates, the better the spatial effect of the fusion method (Zhang, 1999).

Three statistical indices, namely Bias of mean (BM), correlation coefficient (CC) and standard deviation difference (SD), are used in the quantitative assessement of fusion performances (Amarsaikhan et al., 2012; Wald et al., 1997). The equations of these indices are expressed as follows:

- Bias of mean: $BM = \mu_{ori} - \mu_f$ (3.21)

- Correlation coefficient: $CC = \frac{\sum_i (I_i - \mu_{ori})(F_i - \mu_f)}{\sqrt{\sum_i (I_i - \mu_{ori})^2}\sqrt{\sum_i (F_i - \mu_f)^2}}$ (3.22)

- Standard deviation difference: $SD = \sigma_{ori} - \sigma_f$ (3.23)

where μ_{ori} andμ_f are the mean of original spectral image (I) and the fused image (F), respectively. σ_{ori} and σ_f are the standard deviation of original spectral image (I) and the fused image (F), respectively.

The ideal value of *BM* and *CC* are zero and one, respectively, while the lower value of *SD* is better. The closer to one the *CC* value is, the less spectral distortion the fused image is.

In order to estimate the amount of information injected into multispectral images, the entropy information (EI) is utilized. The formula of EI is expressed as:

$$EI = \sum_{n=0}^{255} P_n log P_n \quad (3.24)$$

where P_n is the histogram distribution of the image.

3.2.5 Land cover classification and change detection of wetland

3.2.5.1 Image classification method

The pixel-based spectral image analysis (PBSIA) is the most common technique for mapping landscape features using information from remote sensing (Moffett and Gorelick, 2013). The method uses the spectral signature of each pixel to automatically decide its class. This automated approach places each image pixel in a class. PBSIA is useful for its broad spatial coverage, non-invasiveness, repeatability, analytical speed, and ease of automation (Adam et al., 2009; Ozesmi and Bauer, 2002). These advantages have led to much recent use of PBSIA to map wetlands (Moffett and Gorelick, 2013).

In this study, the classification of the optical and SAR fused images is performed using the maximum likelihood (ML) method. Supervised implementation of ML was used. The procedure of ML includes predefinition of classes, calculating the probability that a pixel belongs to each class in the predefined set, and assigning the pixel to the class to the class with the highest probability (Tso and Mather, 2009).

Table 3.2 Classification theme (Funkenberg et al., 2014)

Code	Spectral classes	Information classes	Description
1	Forest	Forest	Nypa palm, vegetation on limestone hills, mangroves, fruit trees
2	Grassland	Grassland	Grass communities: salinity and soil type
3	Artificial surface	Artificial surface	Urban areas, construction sites, quarries, dikes, and bare areas.
4	Agriculture	Agriculture	Paddy fields and crops
5	Water	Water	Coastal and inland water bodies, canals, and rivers.

In the study area, the sample set for training the classifier (Figures 3.3, 3.4, and 3.5) and validating classification results were based on the classification theme defined by Funkenberg et al. (2014), a land-use map of 2010 with 60 classes, and high resolution satellite images from Google Earth. Five classes were chosen for the classification (Table 3.2).

In order to evaluate the resulting classified maps, a random sampling scheme was implemented. Through comparison between classified maps and reference information, such as high resolution images and land-use maps, accuracy evaluation was obtained via confusion matrices and corresponding kappa coefficient. Land use and land cover (LULC) changes were identified as anthropogenic. For example, Phan and Jacques (2007) and Tong et al. (2004) were able to relate significant decrease in mangrove forests in the VMRD to an expansion of shrimp aquaculture.

Table 3.3 The sample of classes from ERS-2, Landsat 5 TM, and fused data

Item	Class name	Gamma backscatter coefficients		Sample of ERS-2	Sample of Landsat	Sample of fused data
		Average	Standard deviation			
1	Forest	-8.3 dB	± 0.7 dB	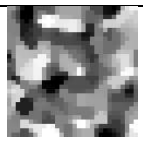		
2	Artificial Surface	-5.1 dB	± 3.4 dB	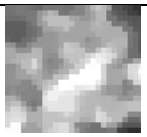		
3	Water	-21.7 dB	± 0.9 dB	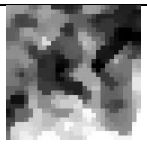	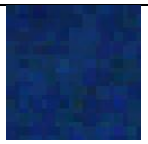	
4	Agriculture	-11.9	± 1.1 dB	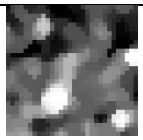		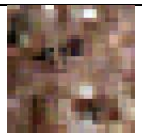
5	Grassland	-7.1	± 0.9 dB	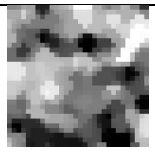		

Table 3.4 The sample of classes from ALOS PASAR, Landsat 5 TM, and fused data

Item	Class name	Gamma backscatter coefficients		Sample of ALOS PALSAR	Sample of Landsat 5	Sample of fused data
		Average	Standard deviation			
1	Forest	-12.0 dB	± 1.3 dB	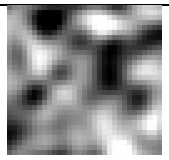	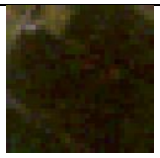	
2	Artificial Surface	-3.5 dB	± 7.5 dB	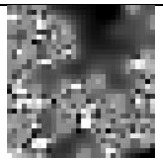	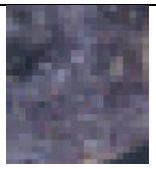	
3	Water	-42.2 dB	± 2.0 dB	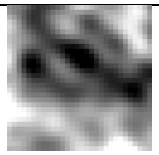		
4	Agriculture	-33.9	± 6.9 dB	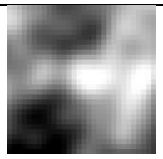		
5	Grassland	-31.8	± 5.4 dB		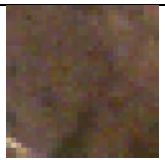	

Table 3.5 The sample of classes from Sentinel 1, Landsat 8, and fused data

Item	Class name	Gamma backscatter coefficients		Sample of Sentinel 1	Sample of Landsat 8	Sample of fused data
		Average	Standard deviation			
1	Forest	-12.9 dB	± 0.7 dB		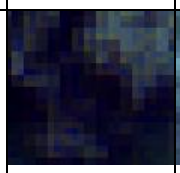	
2	Artificial Surface	-10.6 dB	± 2.6 dB	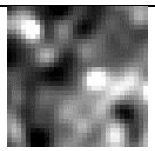		
3	Water	-22.2 dB	± 1.3 dB	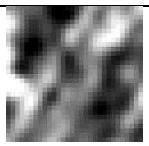		
4	Agriculture	-15.9	± 0.7 dB	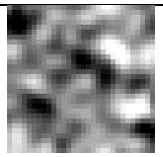		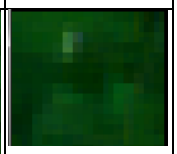
5	Grassland	-14.6	± 0.9 dB	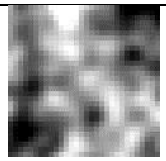		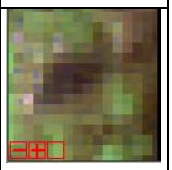

3.2.5.2 Change detection method

For the detection of changes in the distribution of the wetlands over time, a post-classification comparison was used. This is the most widely used approach which has many advantages such as the capability of comparing data from a variety of sources and dates (Jensen, 2005), identifying the nature of change, as well as its location and amount (Dewan et al., 2012). A LULC transition matrix and change statistics that will be computed per pixel (on a pixel-by-pixel basis), provide both quantitative and qualitative information on the gain, loss, and stability of each land cover type.

3.2.6 Flood mapping method

There are several steps implemented to identify the flood extent in 1999 (Figure 3.10). Firstly, two pre- and post-flood Landsat TM scenes were pre-processed to obtain atmospheric corrected products. Then, they were used to calculate the Modified Normalized Difference Water Index (MNDWI) before applying a modified fuzzy c-means (MFCM) to achieve MFCM-MNDWI. In the next step, water and non-water classes were obtained by implementing OSTU method (Otsu, 1979) to the MFCM-MNDWI derived from both pre- and post-flood images. The OSTU method is an automated threshold method and it is optimal for bimodal data. Therefore, this method was applied to remove the independent threshold. The water class extracted from the pre-flood image was the permanent water which was employed with the water class derived from the post-flood image to identify flood water and permanent water in the post-flood image. The changes in Normalized Difference Vegetation Index (NDVI) value and in Normalized Difference Water Index (NDWI) between the pre- and post-flood images were used to detect previously flood-inundated areas. Moreover, the 30 metre SRTM DEM was used to mask out non-flood water at an elevation higher than six metres. Finally, the images were categorized into three classes: flood, non-flood, and permanent water classes.

For mapping the flood extent in 2013, Landsat 8 OLI images were used, and the first four steps of the method implemented were the same as those of the flood mapping procedure for the year 1999 (Figure 3.11). However, cloud free Landsat 8 OLI images over the study area were not available in the dry season of this year. Therefore, one Landsat 8 image collected in the early dry season of year 2014 was used to extract permanent water. Meanwhile, two images acquired at the flood peak and three weeks later were used to solve minor cloud cover in the two images. The final map contains three categories: flood, non-flood, and permanent water.

3.2.6.1 Modified fuzzy c-means method

As discussed previously, mixed pixels are one of the main reasons for image heterogeneity and ambiguity, which in turn is responsible for classification uncertainty (Yang et al., 2015). However, mixed pixels are significantly common in images over wetlands. Several traditional hard clustering methods implemented to extract water

surfaces in wetland conditions cannot separate them to achieve satisfactory results (Comber et al., 2012; Foody et al., 2005). Fuzzy c-means (FCM), one of the fuzzy clustering techniques, is suitable for fixing the problem related to ambiguity as it can manipulate the ambiguity in feature space (Kersten et al., 2005; Yang et al., 2015). However, the traditional FCM is sensitive to noise and imaging artefacts because it has no consideration of the local spatial context (Adhikari et al., 2015). This limits the extensive application of the traditional FCM to satellite images characterized by reflectance complexity (Wang and Bu, 2010). Thus, a MFCM that takes into account the information on the local context can significantly compensate for the heterogeneous reflectance and the poor spectral contrast of an image (Yang et al., 2015).

a. Traditional FCM clustering

The FCM algorithm allows partitioning of an image as a set of N pixels X = (x_1, x_2, …, x_N) into c clusters, by computing the cluster centre v and the membership matrix U, and by iterative optimization that minimizes an objective function defined as follows:

$$J = \sum_{i=1}^{C} \sum_{j=1}^{N} \mu_{ij}^{m} \left\| x_j - v_i \right\|^2 \qquad 3.25$$

Where *N* is the number of pixels, *C* is the number of clusters; *m* is a constant that controls the fuzziness of the resulting partition. μ_{ij} is the degree of fuzzy membership of pixel x_j in the ith cluster, and ||.|| a norm metric.

By assigning large membership values to pixels that are close to the centroid and low membership values to pixel that are far from the centroids the cost function can be minimised. This is done normally with the use of the Euclidean distance measure. Formula 3.26 below is use to update the membership functions and cluster centre.

$$\mu_{ij} = \frac{1}{\sum_{k=1}^{c} \left(\frac{\left\| x_j - v_i \right\|}{\left\| x_j - v_k \right\|} \right)^{\frac{2}{m-1}}} \qquad 3.26$$

and

$$v_i = \frac{\sum_{j=1}^{N} \mu_{ij}^{m} x_j}{\sum_{j=1}^{N} \mu_{ij}^{m}} \quad 3.27$$

b. The conditional spatial fuzzy c-means clustering

In this study, a conditional spatial fuzzy c – means algorithm (CSFCM) proposed by Adhikari et al. (2015) was used. It is started from the notion that the probability of pixel belonging to a cluster is higher if more of its neighbourhood pixels belong to this cluster. Thus, the algorithm takes the level of involvement of a pixel into a cluster by considering its neighbourhood. A local membership function is defined as follows:

$$u_{ij} = \frac{f_{ij}}{\sum_{k=1}^{c} \left(\frac{\|x_j - v_i\|}{\|x_j - v_k\|} \right)^{\frac{2}{m-1}}} \quad 3.28$$

and

$$f_{ij} = \frac{\sum_{k=1}^{Nw} \mu_{ij}}{M} \quad 3.29$$

where f_{ij} is the conditioning variable which defines the level of involvement of pixel x_j into the ith cluster by considering its neighbourhood in a spatial domain. N_w is the square box having the pixel x_j as its centre and M is the number of pixels in the box. The membership value function of the CSFCM is the combination of the global membership values μ_{ij} and the local membership values u_{ij} as following:

$$z_{ij} = \frac{(\mu_{ij})^p (u_{ij})^q}{\sum_{k=1}^{c} (\mu_{kj})^p (u_{kj})^q} \quad 3.30$$

and the centre values function is defined as follows:

$$w_i = \frac{\sum_{j=1}^{N} z_{ij}^{m} x_j}{\sum_{j=1}^{N} z_{ij}^{m}} \quad 3.31$$

where p and q are the parameters to control the relative importance of both global and local membership functions.

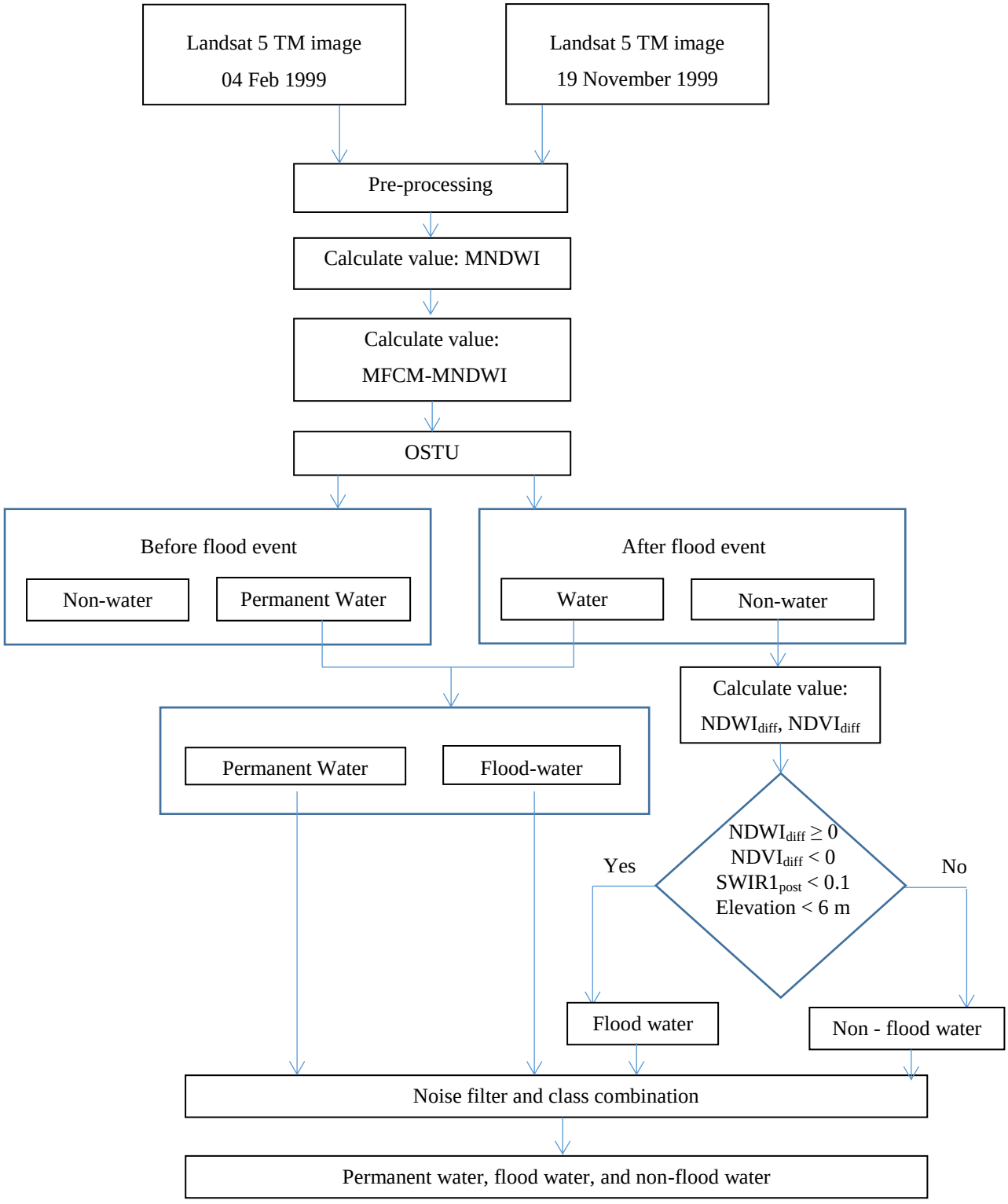

Figure 3.10 Flowchart showing working procedure for mapping 1999 flood

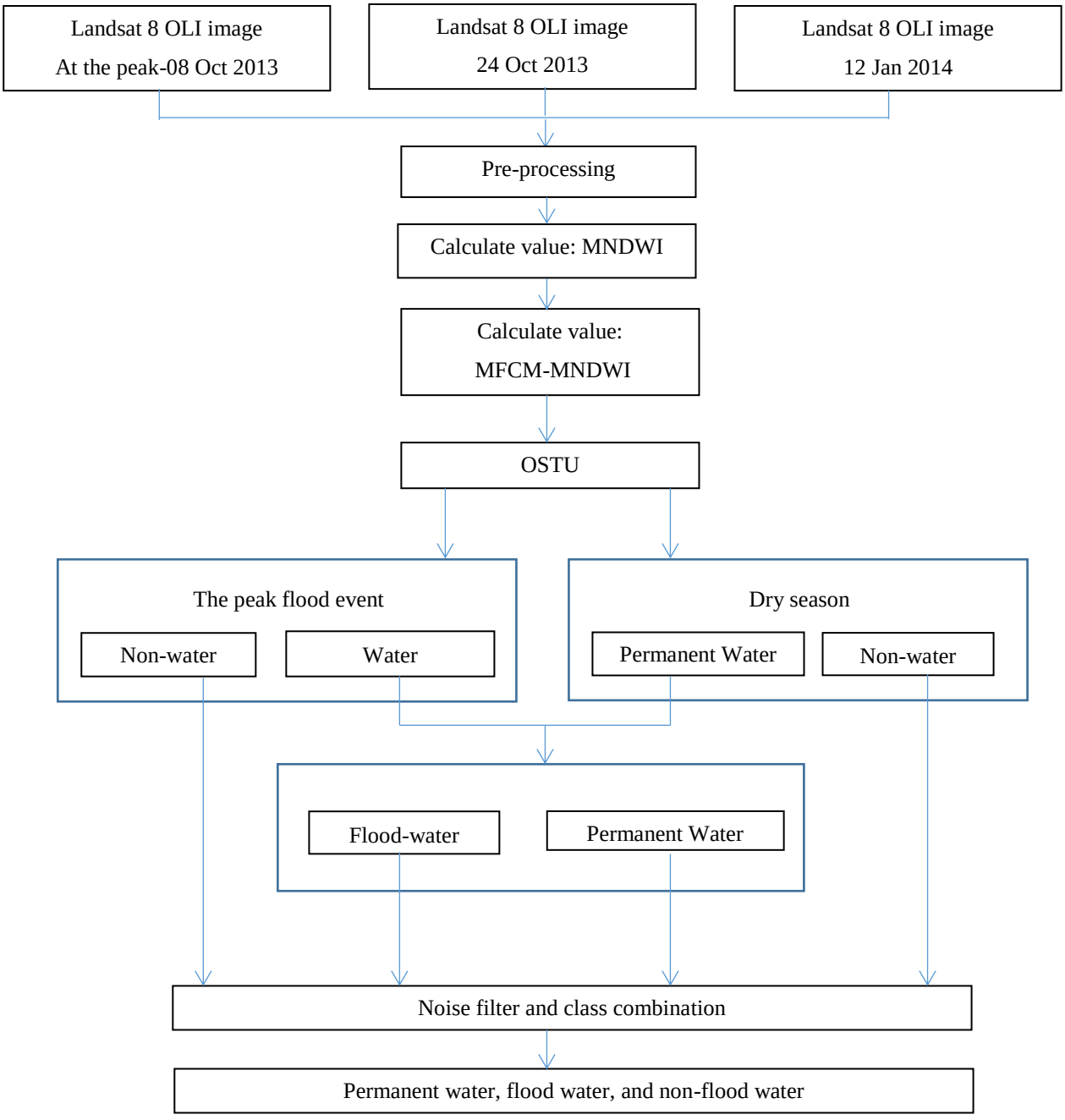

Figure 3.11 Flowchart showing working procedure for mapping 2013 flood

4 RESULTS

4. 1 Multi-sensor data fusion

4.1.1 Speckle suppression

Table 4.1 demonstrates the results of the preservation of the mean (NM) and speckle suppression (SI). Generally, five filters perform well on the preservation of mean. It is observed (Table 4.1) that Gamma is the best method for mean preservation of all three images, followed by Lee method and the Frost with a 7x7 window is the least presentative one with a NM value of 0.824. In terms of removing speckle, as the smaller the SI, the better the speckle suppression, the results prove that when window size increases the SI decreases. The Gamma performs the best, followed by the Median method, Lee, Local region, and Frost method. However, by visually inspecting despeckled results, increased smoothing also leads to the loss of some details.

Table 4.1 Comparison of speckle suppression using different filtering techniques for SAR images

Window Size	Filter	ERS-2		ALOSPALSAR		Sentinel 1	
		NM	SI	NM	SI	NM	SI
Original image		**1.000**	**0.338**	**1.000**	**0.313**	**1.000**	**0.182**
3x3	Median	0.979	0.203	0.980	0.175	0.999	0.166
5x5		0.980	0.147	0.979	0.137	0.999	0.147
7x7		0.981	0.122	1.000	0.180	0.999	0.133
3x3	Local Region	0.979	0.256	0.983	0.207	0.999	0.179
5x5		0.978	0.194	0.983	0.165	0.997	0.169
7x7		0.986	0.160	0.983	0.207	0.996	0.155
3x3	Lee	0.999	0.251	1.000	0.180	0.999	0.165
5x5		0.999	0.220	1.000	0.180	0.997	0.152
7x7		1.000	0.209	1.000	0.180	0.997	0.144
3x3	Frost	0.939	0.318	1.000	0.268	0.999	0.164
5x5		0.880	0.397	1.000	0.180	0.999	0.148
7x7		0.824	0.482	1.000	0.180	0.999	0.136
3x3	Gamma	1.000	0.184	1.000	0.157	1.000	0.129
5x5		1.000	0.135	1.000	0.125	1.000	0.142
7x7		1.000	0.113	1.000	0.109	1.000	0.129

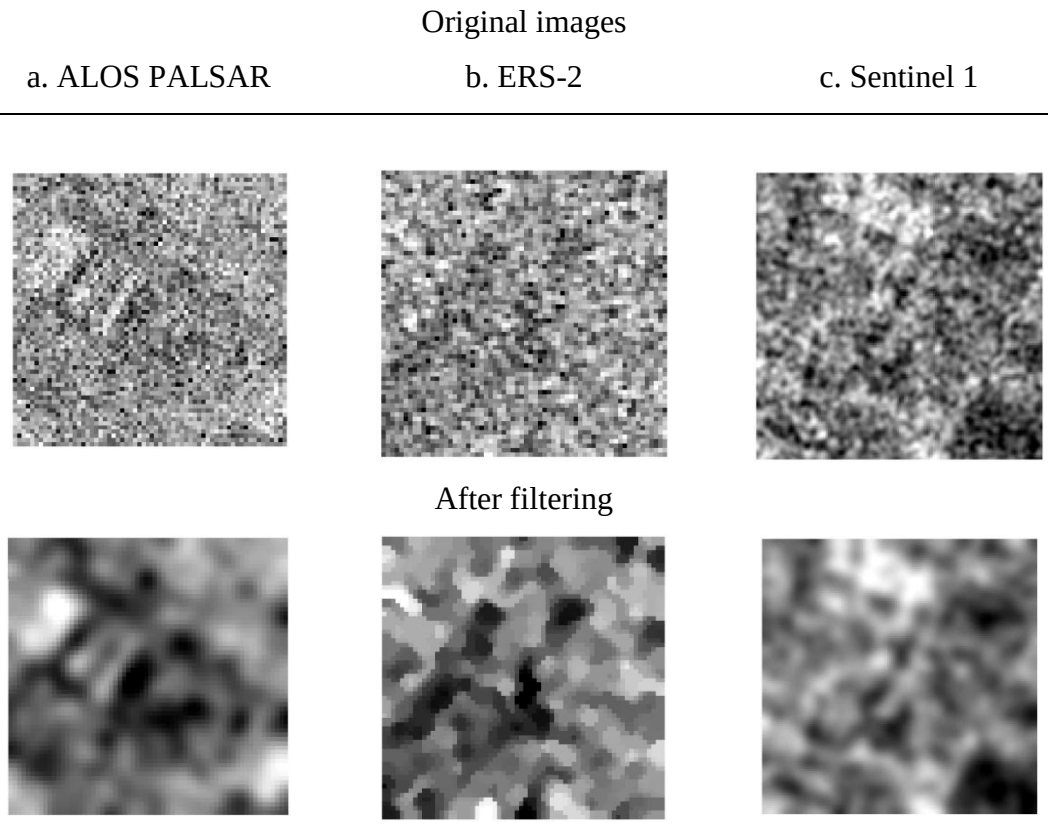

Figure 4.1 Three test areas in SAR images

It is worth noting that one normally has to make a trade-off between reduction of speckle and preservation of detail (Nyoungui et al., 2002). For removing speckle of the ALOS PALSAR and the Sentinel 1 data, based on the result of speckle suppression (Table 4.1) and visual evaluation, the Gamma filter was selected, while the best filter for ERS-2 data was the median filter. The size of the sliding window was 3 x 3 pixels. The filtering is repeated five times. Figures 4.2, 4.3, and 4.4 demonstrate the speckle suppressed images.

Figure 4.2 Speckle suppressed ALOS PALSAR image using the Gamma filter

Figure 4.3 Speckle suppressed Sentinel 1 image using the Gamma filter

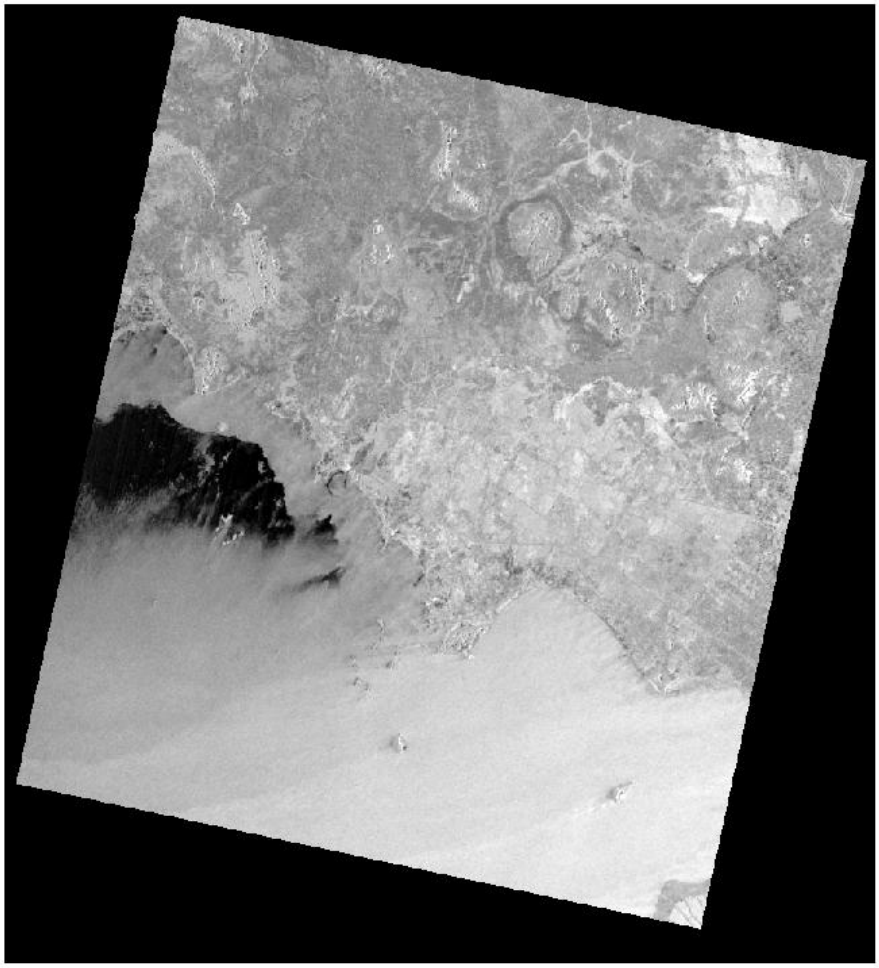

Figure 4.4 Speckle suppressed ERS-2 image using the Median filter

In order to find the most appropriate fusion method for integrating Landsat 5 TM and ALOSPALSAR, Landsat 5 TM and ERS-2, and Landsat 8 and Sentinel 1 imagery, two hybrid image fusion methods of wavelet transform, IHS and wavelet method and PCA and wavelet, were applied. Their fused results were assessed using statistical indices such as correlation coefficient (CC), bias of mean (BM), and standard deviation difference (SDD) (Abdikan et al., 2014).

4.1.2 Landsat 5 TM and SAR imagery (ERS-2 and ALOSPALSAR) fused results

In this study, two pairs of images, ERS-2 and Landsat 5 TM, and ALOSPALSAR and Landsat 5 TM, were merged using the two above-mentioned hybrid fusion methods. The Landsat 5 TM images have 30 m spatial resolution, while the ERS-2 and ALOS PALSAR images have 20 m and 12 m spatial resolution, respectively. Therefore,

before image fusion, the MS images of Landsat TM were resampled by using the nearest neighbour method to have the same spatial resolutions as the SAR images. The performance of the two fusion methods was evaluated using statistical indices to find the best one. The fused data of the best one was used for classifying the study area.

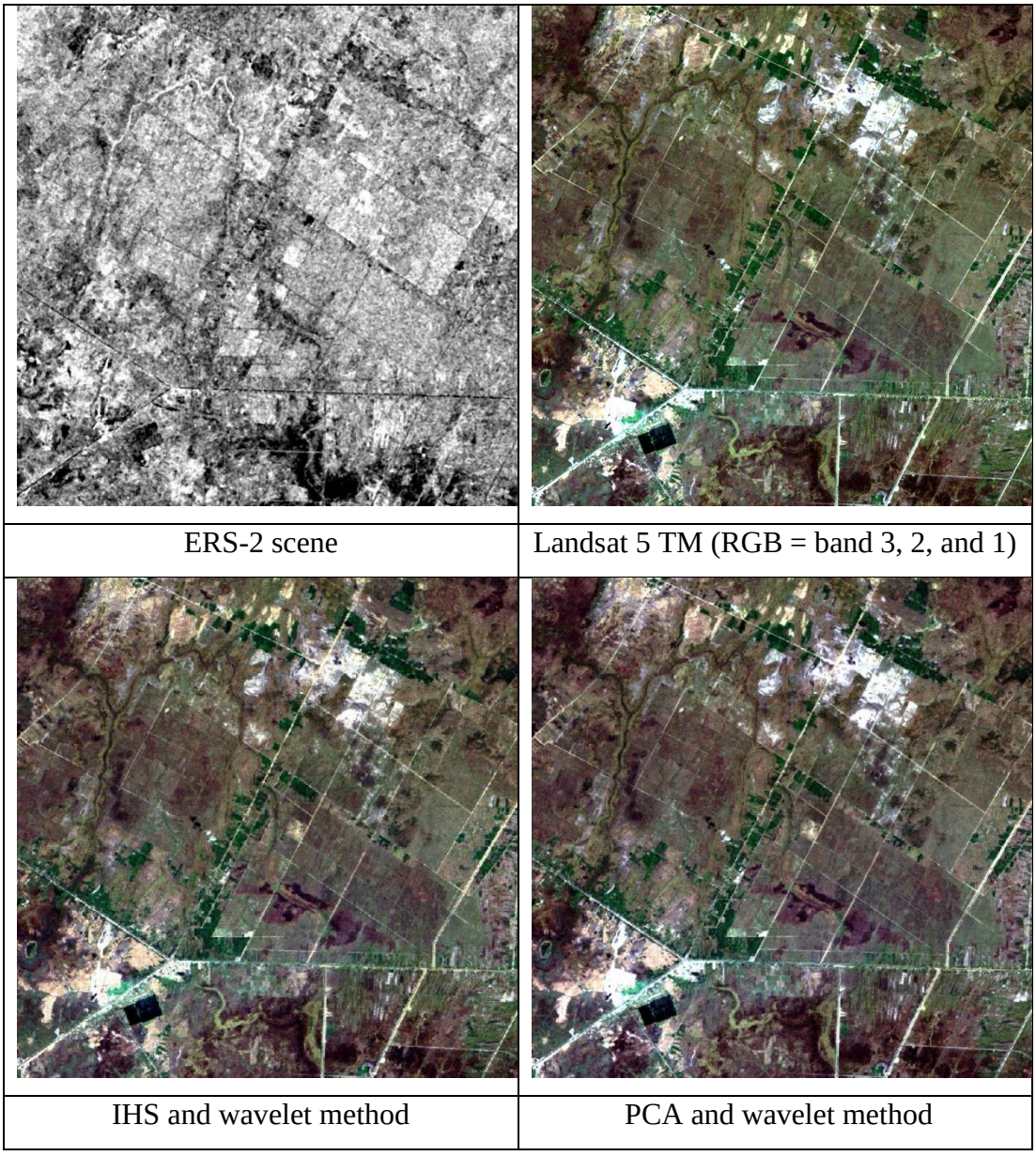

Figure 4.5 Fused images of ERS-2 and Landsat 5 TM data

In terms of the interpretability of the images before and after fusion, Figures 4.5 and 4.6 show that the colour composites in fused images are not different from those of the original MS images. As the spatial resolutions of the fused images are 20 m and 12 m for ERS-2 – Landsat TM and ALOS PALSAR – Landsat TM fused products, they are

more easily and accurately identified than the SAR data. This is obviously clear in the case of ALOS PALSAR (Figures 4.6 c and d). In addition, the fused results by PCA-wavelet are sharper than those by IHS-wavelet method.

While it might be simple to assess the quality of fused results by visual inspection, the statistical comparison can quantitatively assess the performance of each image fusion method (Chibani, 2006). It can be observed from Table 4.2 that all the ERS-2 and Landsat TM images fused using the two methods have high CC values. This underpins the obvious similarity in the appearance of the fused results and original MS images. However, after fusing the detail of ERS-2 image into MS images using the PCA-wavelet method, the CC between the merged products and the original MS images are higher than those fused by using the IHS-wavelet method in almost all bands. ERS2-Band 1 and ERS2-Band 2 images fused using the PCA-wavelet method have much higher CC values than those fused by the IHS-wavelet method, whereas only the CC value from ERS2-Band 5 image fused by the latter method is slightly larger than that by the former method. In terms of BM and SDD values, almost all the BM and SDD of images fused using the PCA-wavelet method are lower than those fused using the IHS-wavelet method. A similar figure is seen in the case of ALOS PALSAR and Landsat TM fusion (Table 4.3).

Table 4.2 Statistical evaluation of ERS-2 and Landsat 5 fusion

Band	IHS and wavelet			PCA and wavelet		
	CC	BM (10^-4)	SDD (10^-4)	CC	BM (10^-4)	SDD (10^-4)
Ideal	**1**	**0**	**0**	**1**	**0**	**0**
1	0.7917	4.4	7.5	0.9681	1.6	0.4
2	0.8981	4.1	0.3	0.9604	2.3	0.6
3	0.9445	4.4	4.6	0.9556	3.3	0.9
4	0.9204	8	8.5	0.9772	5.3	0.3
5	0.9315	10	0.7	0.9216	10	0.3
6	0.9536	6.2	3.4	0.9291	7.4	0.1

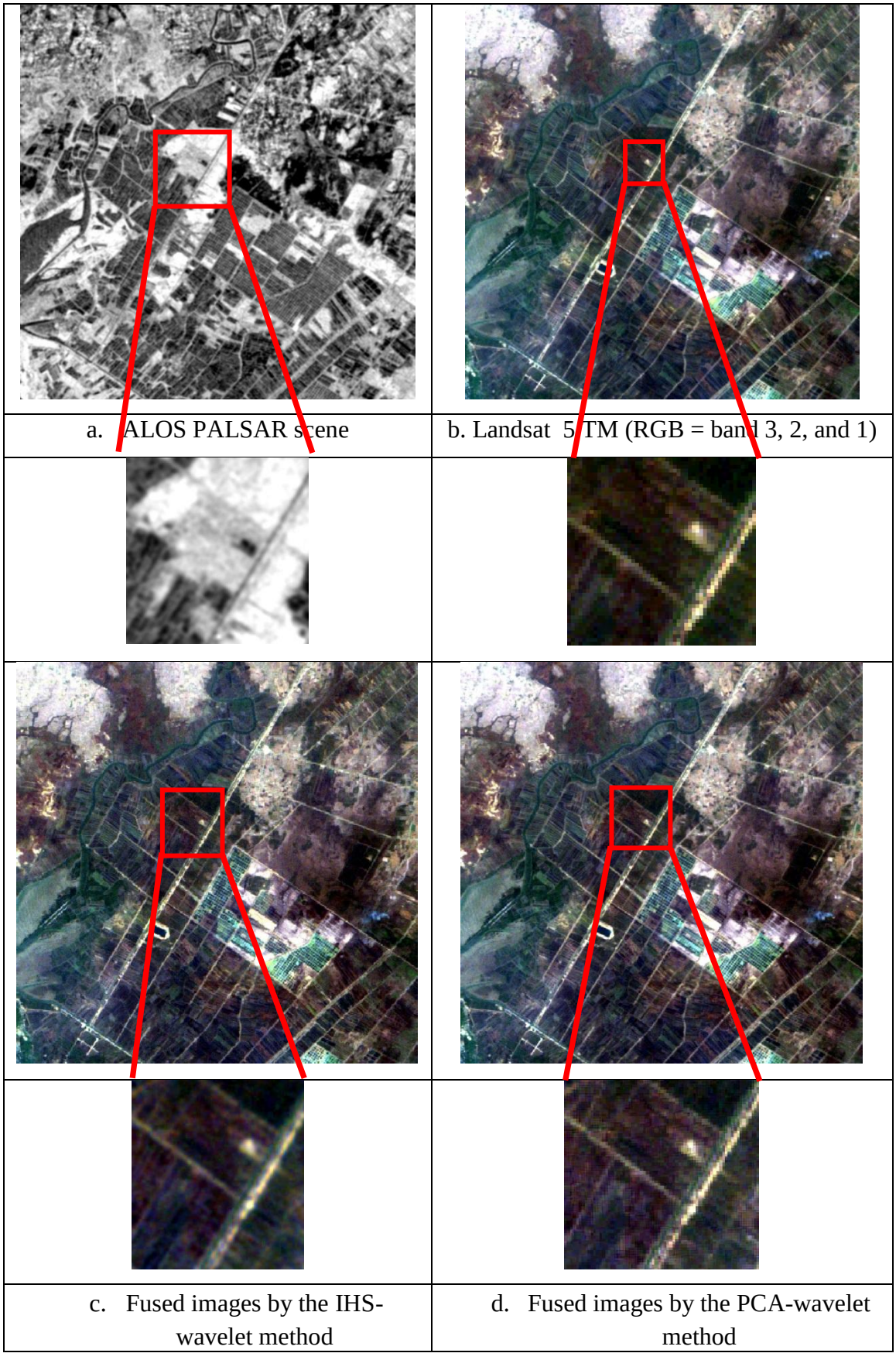

a. ALOS PALSAR scene

b. Landsat 5 TM (RGB = band 3, 2, and 1)

c. Fused images by the IHS-wavelet method

d. Fused images by the PCA-wavelet method

Figure 4.6 Fused images of ALOS PALSAR and Landsat 5 TM data

Table 4.3 Statistical evaluation of ALOS PALSAR and Landsat 5 TM fusion

Band	IHS and Wavelet			PCA and Wavelet		
	CC	BM (10^-4)	SDD (10^-4)	CC	BM (10^-4)	SDD (10^-4)
Ideal	**1**	**0**	**0**	**1**	**0**	**0**
1	0.8947	2.8	4.4	0.9935	0.6	0.1
2	0.9628	2.6	0.6	0.9925	1	0.3
3	0.9850	2.6	1.9	0.9889	1.8	0.6
4	0.9457	6.6	13	0.9855	5.0	0.2
5	0.9855	10	1.4	0.9797	11	0.6
6	0.9878	6.6	2.8	0.9803	7.9	0.2

Both visual and quantitative assessments show that the PCA-wavelet method gives better results with less spectral distortion and sharpened features. Therefore, in this study, the PCA-wavelet fusion method was the choice for integrating optical and SAR imagery.

4.1.3 Pansharpening MS images using the PAN-Sentinel 1 fused image

In this study, the Landsat 8 MS images were pansharpend with the PAN-Sentinel 1 fused image, using the PCA-wavelet fusion method. The spatial resolutions of MS, PAN, and Sentinel 1 images were 30, 15, and 20 m respectively. Therefore, before image fusion, the Sentinel 1 and MS images were resampled by using the nearest neighbour method to the same spatial resolution as the PAN image.

Figure 4.7 shows the result of integrating PAN and Sentinel 1 images using two models, namely full combination model and weighted combination model. The two PAN-Sentinel 1 scenes fused by the two models were used to pansharpen MS images using the PCA-wavelet fusion method (Figures 4.8 d and 4.8 e). Generally, it can be seen from Table 4.4 that all fused images have high CC values. Furthermore, the CC between the images fused by using the full combination mode and original MS images is slightly lower than those by the weighted combination model. When comparing the CC and BM values among fused bands, fused bands 1, 2, and 3 have CC values higher than fused bands 4, 5, and 6, whereas the first three fused bands have BM values much lower than the last three. These larger distortions in spectral values of the fused bands 4, 5, and 6 are caused by the difference in the wavelength of the PAN image and the

last three bands. The smaller spectral distortion of the fused images by the weighted combination model compared to that by the full integration model is due to the former model injecting fewer details from the SAR image into the MS image than the latter does. As the amount of information an image contains is normally measured by entropy information (Chibani and Houacine, 2003), entropy values from Table 4.5 underpin this point as the larger the entropy value is the more information from the SAR image introduced in MS images. Moreover, the difference in the wavelength of SAR data and MS data creates the spectral distortion of fused data.

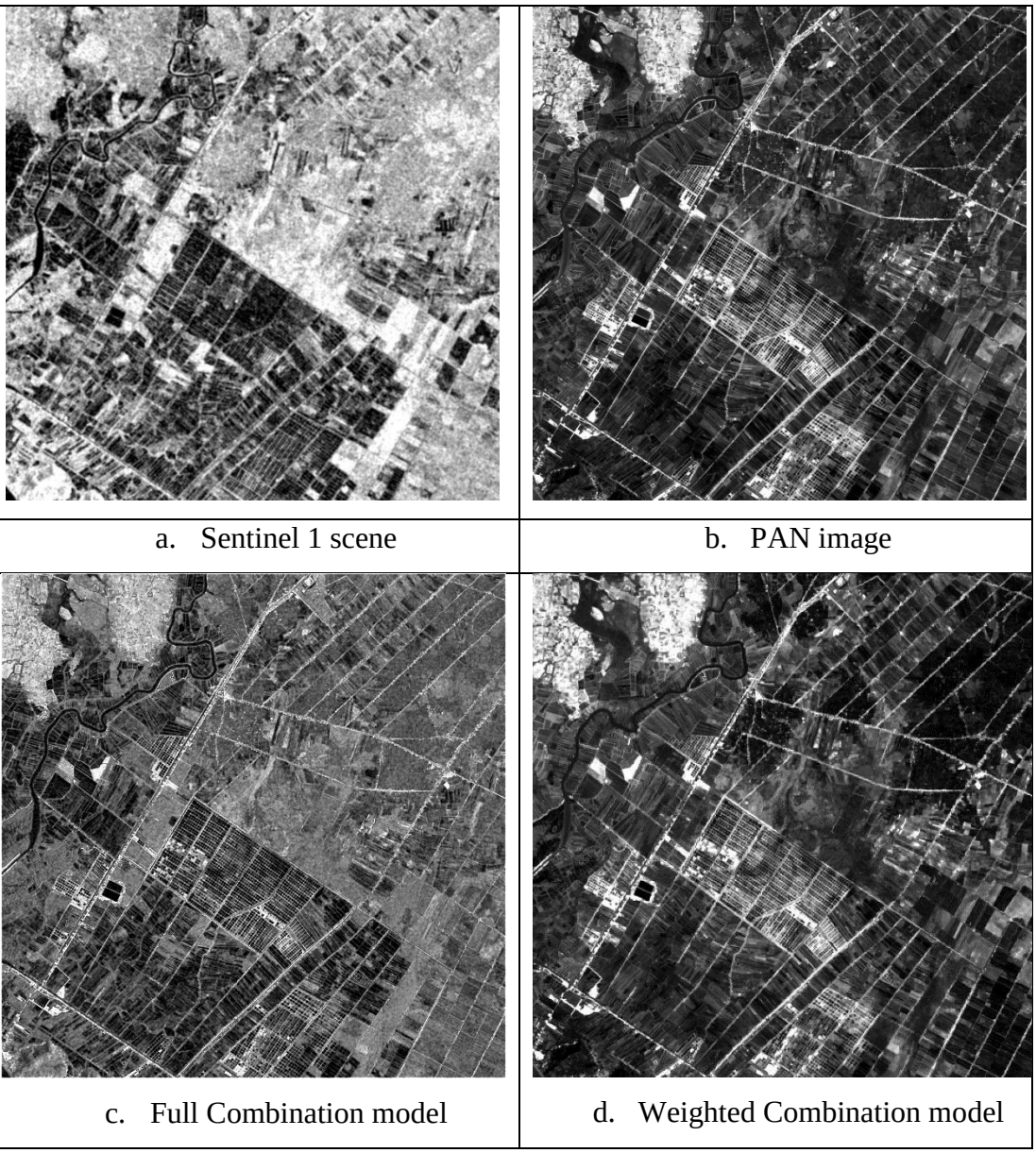

a. Sentinel 1 scene

b. PAN image

c. Full Combination model

d. Weighted Combination model

Figure 4.7 PAN-Sentinel 1 result fused by the ‘a trous’ wavelet method

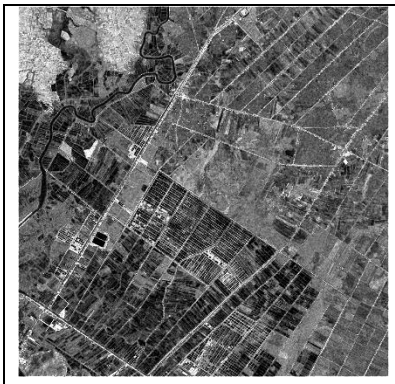

a. PAN-Sentinel 1 fused scene by full integration model

d. Full integration model

b. PAN-Sentinel 1 fused scene by weighted integration model

c. Landsat 8 (RGB = band 4, 3, and 2)

e. Weighted integration model

Figure 4.8 Pansharpening results by the PCA-wavelet method using the PAN-Sentinel 1 fused image

Table 4.4 Statistical evaluation results of Sentinel 1 and Landsat 8 fusion

Band	Full Integration (FI) model			Weighted Combination (WC) model		
	CC	BM (10^-4)	SDD (10^-4)	CC	BM (10^-4)	SDD (10^-4)
Ideal	**1**	**0**	**0**	**1**	**0**	**0**
1	0.9976	0.2	0.08	0.9980	0.2	0.2
2	0.9828	0.7	0.5	0.9856	0.6	0.9
3	0.9962	0.5	0.2	0.9968	4.6	0.6
4	0.8999	13	0.6	0.9158	12	1.5
5	0.9137	7.8	0.5	0.9276	7.2	1.5
6	0.9379	3.8	0.2	0.9480	3.5	1.7

Table 4.5 Entropy information of images

Band	Entropy Information		
	Original	WC	FI
1	2.9024	2.9186	2.9219
2	3.5729	3.5750	3.5757
3	4.1123	4.1344	4.1396
4	6.6230	6.6672	6.6717
5	6.0129	6.0484	6.0483
6	5.1276	5.1531	5.1532

Since the spectral distortion of the images fused by the full integration model is small and the images obtain more information from Sentinel 1, for the purpose of classification, full integration was the best model as it might help to improve the separability of classes (Chibani, 2007).

4. 2 Wetland change detection

4.2.1 Land cover classification using fused images

In order to see the benefits of image fusion, a comparison of classification results achieved from Landsat images with the ones obtained from fused data was made.

The two land cover maps produced by using a Landsat 5 TM image and the fused image of ERS-2 and Landsat 5 TM are shown in Figure 4.9, the results of accuracy evaluation are illustrated in Tables 4.6 and 4.7

For the classification of original MS images, the overall accuracy was 82.73, 82.07, and 75.67% for the 1998, 2008, and 2016 classification, respectively. The image fusion procedure successfully increased the overall accuracy of classification to 85.61, 88.76%, and 86.31% for the 1998, 2008, and 2016, respectively. The same figure was seen for the kappa coefficient as it was increased from 0.72 to 0.83 for year 1998, from 0.76 to 0.85 for year 2008, and from 0.68 to 0.82 for year 2016.

Table 4.6 Confusion matrix 1998 – Classification using Landsat 5 TM images

Landsat 5 image		Reference pixels						
Classified pixels	Land cover	Forest	Artificial Surface	Water	Agriculture	Grassland	Total	User Accuracy
	Forest	39	2	1	1	3	46	84.78
	Artificial Surface	2	23	0	2	4	31	74.19
	Water	0	2	26	1	0	29	89.66
	Agriculture	0	7	0	27	3	37	72.97
	Grassland	10	4	5	1	115	135	85.19
Total		51	38	32	32	125	278	
Producer Accuracy		76.47	60.53	81.25	84.38	92.00		
Overall accuracy		82.73%			Kappa coefficient		0.72	

Table 4.7 Confusion matrix 1998 – Classification using fused images

Landsat 5 image		Reference pixels						
Classified pixels	Land cover	Forest	Artificial Surface	Water	Agriculture	Grassland	Total	User Accuracy
	Forest	40	0	1	0	4	45	88.9
	Artificial Surface	0	30	1	5	2	38	78.9
	Water	1	1	29	0	4	35	82.8
	Agriculture	0	4	1	27	3	35	77.1
	Grassland	10	3	0	0	112	125	89.6
Total		51	38	32	32	125	278	
Producer Accuracy		78.43	78.94	90.62	84.38	89.60		
Overall accuracy		85.61 %			Kappa coefficient		0.83	

Table 4.8 Confusion matrix 2008 - Classification using Landsat 5 TM images

Landsat 5 image		Reference pixels						
Classified pixels	Land cover	Forest	Artificial Surface	Water	Agriculture	Grassland	Total	User Accuracy
	Forest	40	2	1	0	8	51	78.4
	Artificial Surface	1	17	3	5	2	28	60.7
	Water	3	5	71	2	0	81	87.7
	Agriculture	1	4	2	107	8	122	87.7
	Grassland	4	1	1	11	58	75	77.3
Total		49	29	78	125	76	357	
Producer Accuracy		81.63	58.62	91.03	85.60	76.32		
Overall accuracy		82.07 %			Kappa coefficient		0.76	

Table 4.9 Confusion matrix 2008 – Classification using fused images

Fused image		Reference pixels						
Classified pixels	Land cover	Forest	Artificial Surface	Water	Agriculture	Grassland	Total	User Accuracy
	Forest	44	0	2	1	3	50	88.0
	Artificial Surface	1	27	3	6	1	38	71.1
	Water	2	1	72	0	2	77	93.5
	Agriculture	0	1	0	108	5	114	94.7
	Grassland	2	0	1	9	65	77	84.4
Total		49	29	78	124	76	356	
Producer Accuracy		89.80	93.10	92.31	87.10	85.53		
Overall accuracy		88.76 %			Kappa coefficient		0.85	

Table 4.10 Confusion matrix 2016 - Classification using Landsat 8 images

Landsat 8 image		Reference pixels						
Classified pixels	Land cover	Forest	Artificial Surface	Water	Agriculture	Grassland	Total	User Accuracy
	Forest	28	0	6	2	2	38	73.7
	Artificial Surface	3	38	11	6	5	63	60.3
	Water	1	1	36	1	3	42	85.7
	Agriculture	4	2	2	82	5	95	86.3
	Grassland	0	3	2	5	15	25	60.0
Total		36	44	57	96	30	263	
Producer Accuracy		77.78	86.36	63.16	85.42	50.00		
Overall accuracy		75.67 %			Kappa coefficient		0.68	

Table 4.11 Confusion matrix 2016 – Classification using fused images

Fused image		Reference pixels						
Classified pixels	Land cover	Forest	Artificial Surface	Water	Agriculture	Grassland	Total	User Accuracy
	Forest	32	0	4	1	1	38	84.2
	Artificial Surface	1	40	3	3	0	47	85.1
	Water	1	0	46	5	1	53	87.0
	Agriculture	2	4	1	83	3	93	89.2
	Grassland	0	0	3	4	25	32	80.6
Total		36	44	57	96	30	263	
Producer Accuracy		88.89	90.91	82.46	86.46	83.33		
Overall accuracy		86.31 %			Kappa coefficient		0.82	

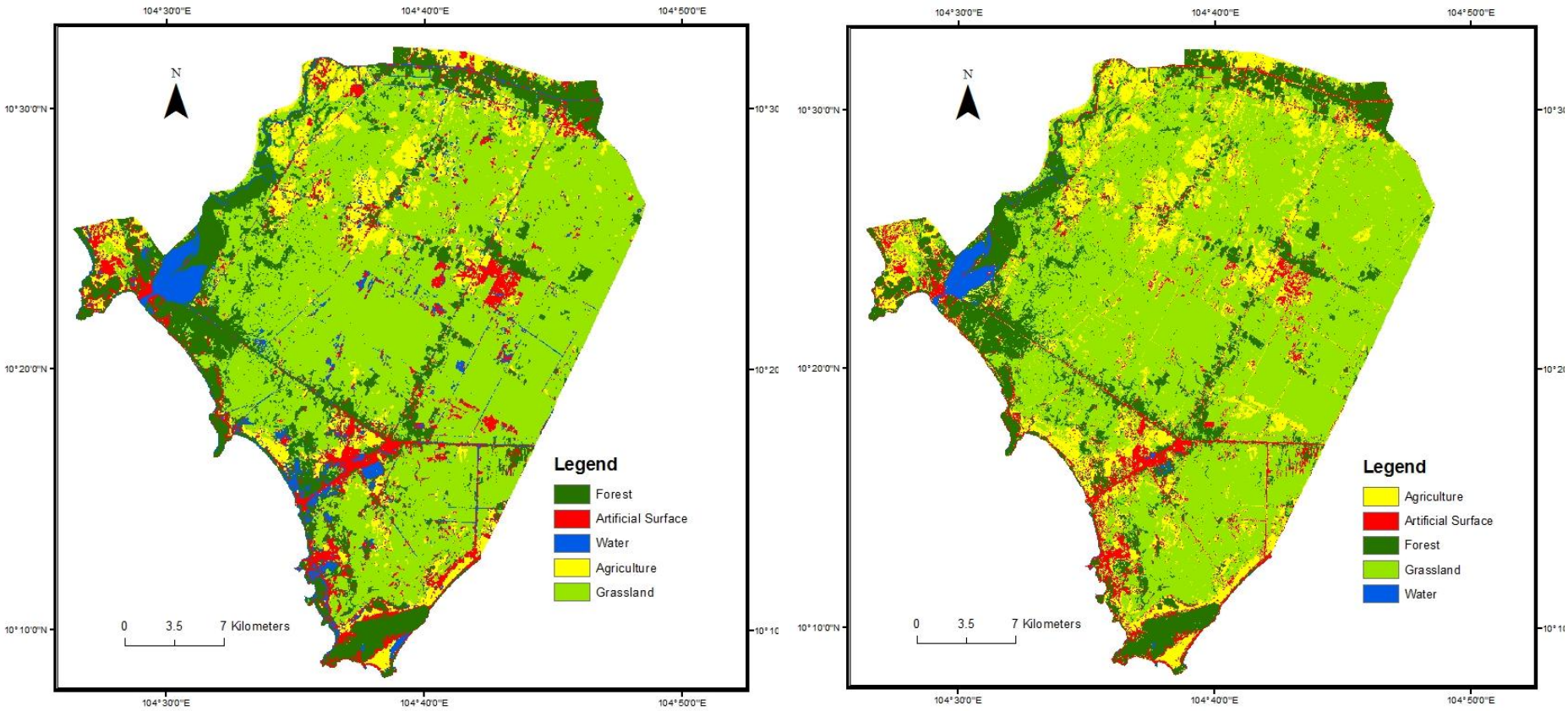

Figure 4.9 Land cover classification 1998 (a) Fused ERS-2 and Landsat 5 TM data (b) Original Landsat 5 TM

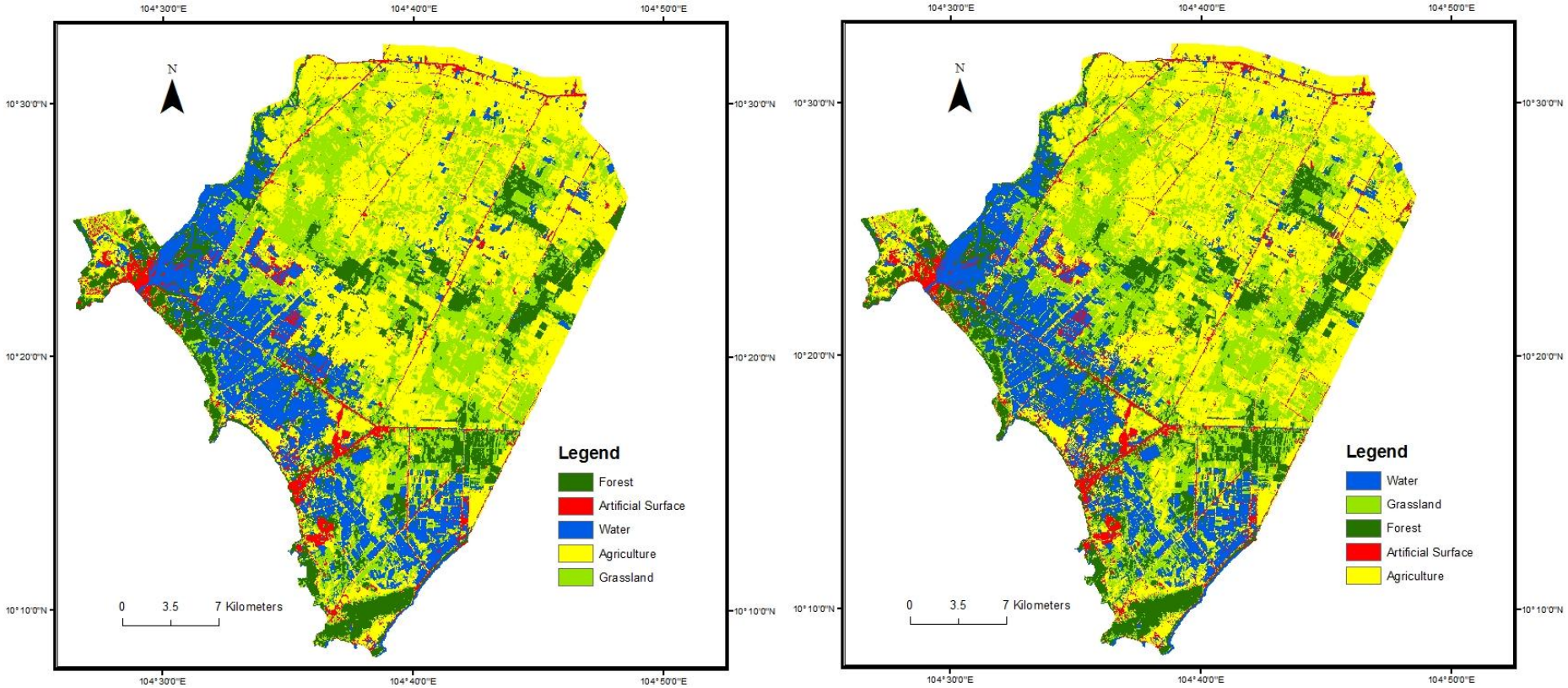

Figure 4.10 Land cover classification 2008 (a) Fused ALOS PALSAR and Landsat 5 TM image (b) Original Landsat 5 TM

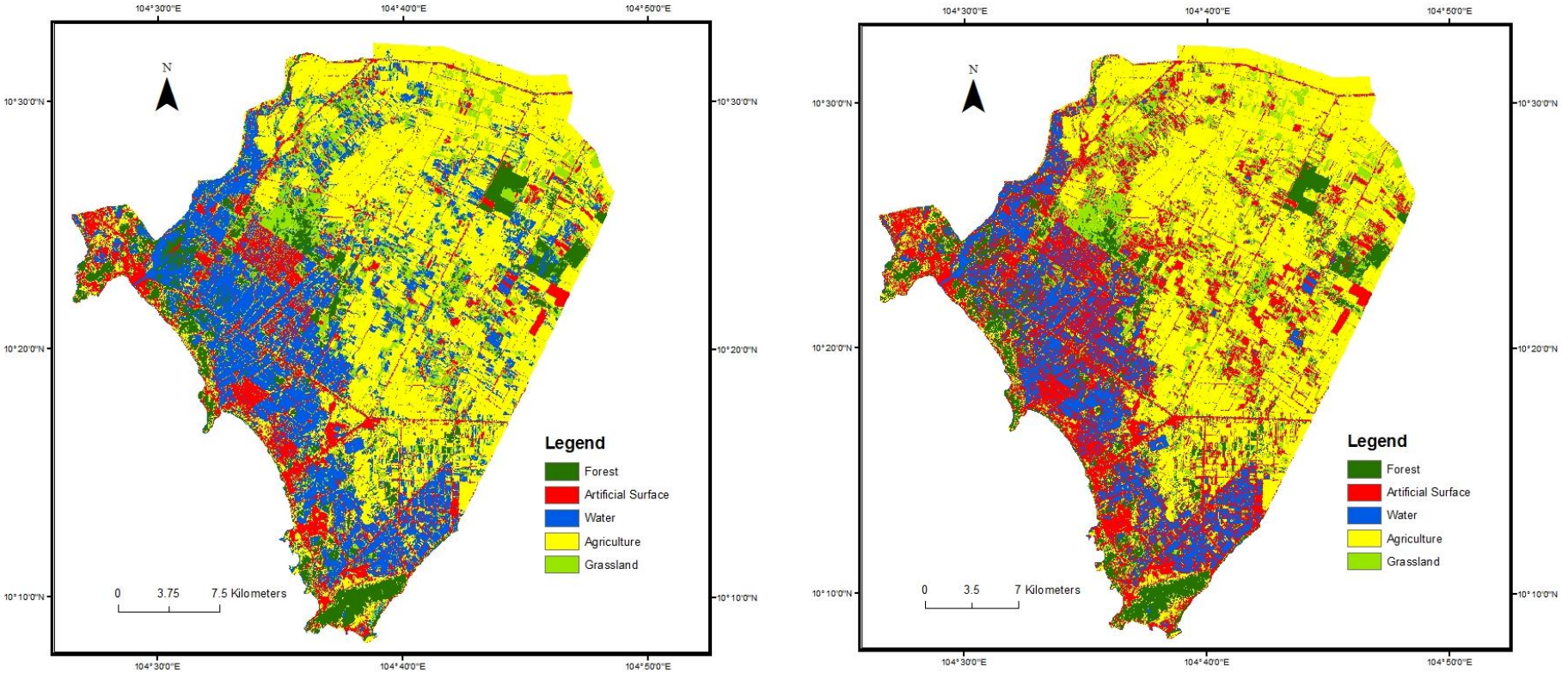

(a) (b)

Figure 4.11 Land cover classification 2016 (a) Fused Sentinel and Landsat 8 OLI fused image (b) Original Landsat 8 OLI

4.2.2 Wetland change over the period from 1998 to 2016

As the land cover maps derived from fused images were more accurate than those produced by the original MS images, they were used to detect wetland changes over the study period. The study period was divided into two periods: 1998-2008 and 2008-2016. As seen from Figure 4.9, the area of grassland was the largest in 1998 with 59.43 %, followed by forest, agriculture, artificial surface, and water with 17.53 %, 9.49 %, 8.17 %, and 5.38 % respectively. While forest was mainly found in the southern, western, and northern fringes of the study area, agriculture was mainly distributed in the northern study area. Moreover, water bodies were confined to the western and southwestern edges of the study area. There was a significant increase in agriculture, water, and artificial surface from 1998 to 2016. This trend continued in the second period with a higher rate of increase for all land cover types except water. The annual rate of the area of each land cover type is demonstrated in Table 4.12.

Table 4.12 Annual rate of land cover change (%)

Period	Forest	Artificial Surface	Water	Agriculture	Grassland
1998-2008	- 7.2	7.3	6.0	3.8	- 7.2
2008-2016	- 8.0	7.5	5.2	3.9	- 9.8

Tables 4.13 and 4.14 suggest that the period between 1998 and 2008 identified a loss of 71.92% (406.24 km^2) in grassland area (Figure 4.12 a). This loss was due to the conversion of over 31 % (178.06 km^2) and almost 19% (106.8 km^2) of grassland into agriculture and water (mainly aquaculture) respectively. The same figure was recorded for the status of forest. Over 26% and near 24% of forest was converted into water and agriculture respectively. Figure 4.12 shows that these decreases were experienced mainly in the northern and western portions of the study area.

It is observed from Tables 4.13 and 4.14 that agriculture covers the largest area with over 40% (388.25 km^2), followed by water bodies, and artificial surface with 23.58% (224.11 km^2), and 14.13% (134.31 km^2) respectively. The areas of grassland and forest are the smallest with 12.15% and 9.29% respectively. This is a result of nearly two

decades of a strong conversation from grassland and forest into agriculture, aquaculture, and built-up in the region.

Table 4.13 Land cover conversions between 1998 and 2008 (%)

Land cover types		1998					
		Forest	Artificial Surface	Water	Agriculture	Grassland	Class total
2008	Forest	27.82	11.99	15.24	2.73	13.66	15.05
	Artificial Surface	11.73	27.07	18.51	10.73	7.83	10.93
	Water	26.62	12.71	39.47	8.59	18.91	19.88
	Agriculture	23.91	30.64	18.97	62.33	31.52	32.37
	Grassland	9.92	17.59	7.81	15.62	28.08	21.77
	Class total	17.53	8.17	5.38	9.49	59.43	
	Class Changes	72.18	72.93	60.53	37.67	71.92	

Table 4.14 Land cover conversions between 1998 and 2008 (km^2)

Land cover types		1998					
		Forest	Artificial Surface	Water	Agriculture	Grassland	Class total
2008	Forest	**46.35**	9.31	7.80	2.47	77.16	143.08
	Artificial Surface	19.54	**21.01**	9.47	9.68	44.22	103.91
	Water	44.34	9.86	**20.20**	7.75	106.80	188.96
	Agriculture	39.84	23.79	9.71	**56.23**	178.06	307.62
	Grassland	16.52	13.65	4.00	14.10	**158.63**	206.89
	Class total	166.59	77.62	51.17	90.22	564.87	950.47
	Class Changes	120.24	56.61	30.97	33.99	406.24	

From 2008 to the present, both grassland and forest continued reducing by 162.69 km^2 and 91.41 km^2 respectively (Tables 4.15 and 4.16), much smaller than in the 1998-2008 period, but with higher annual rates of 9.8% and 8.0% compared to a rate of 7.2% for both in the first ten years (Table 4.12). These attribute to an expansion in agriculture and water from 307.76 km^2 and 188.77 km^2 to 388.25 km^2 in 2016 for the former and to 224.11 km^2 in 2016 for the latter. An expansion is recorded in artificial surface from 103.83 km^2 in 2008 to 134.31 km^2 in 2016.

Table 4.15 Land cover conversions between 2008 and 2016 (%)

Land cover types		2008					
		Forest	Artificial Surface	Water	Agriculture	Grassland	Class total
2016	Forest	36.09	3.43	5.06	2.04	8.36	9.29
	Artificial Surface	9.75	40.24	15.36	8.68	11.04	14.13
	Water	16.04	15.35	58.77	10.35	20.50	23.58
	Agriculture	26.46	31.25	13.96	68.73	38.68	40.85
	Grassland	11.67	9.72	6.85	10.20	21.43	12.15
	Class total	15.05	10.92	19.86	32.38	21.78	
	Class Changes	63.91	59.76	41.23	31.27	78.57	

Table 4.16 Land cover conversions between 2008 and 2016 (km^2)

Land cover types		2008					
		Forest	Artificial Surface	Water	Agriculture	Grassland	Class total
2016	Forest	51.61	3.56	9.55	6.27	17.31	88.31
	Artificial Surface	13.94	41.78	28.99	26.72	22.87	134.31
	Water	22.93	15.94	110.95	31.85	42.44	224.11
	Agriculture	37.85	32.45	26.35	211.52	80.08	388.25
	Grassland	16.68	10.09	12.93	31.40	44.36	115.47
	Class total	143.02	103.83	188.77	307.76	207.05	950.43
	Class Changes	91.41	62.05	77.82	96.24	162.69	

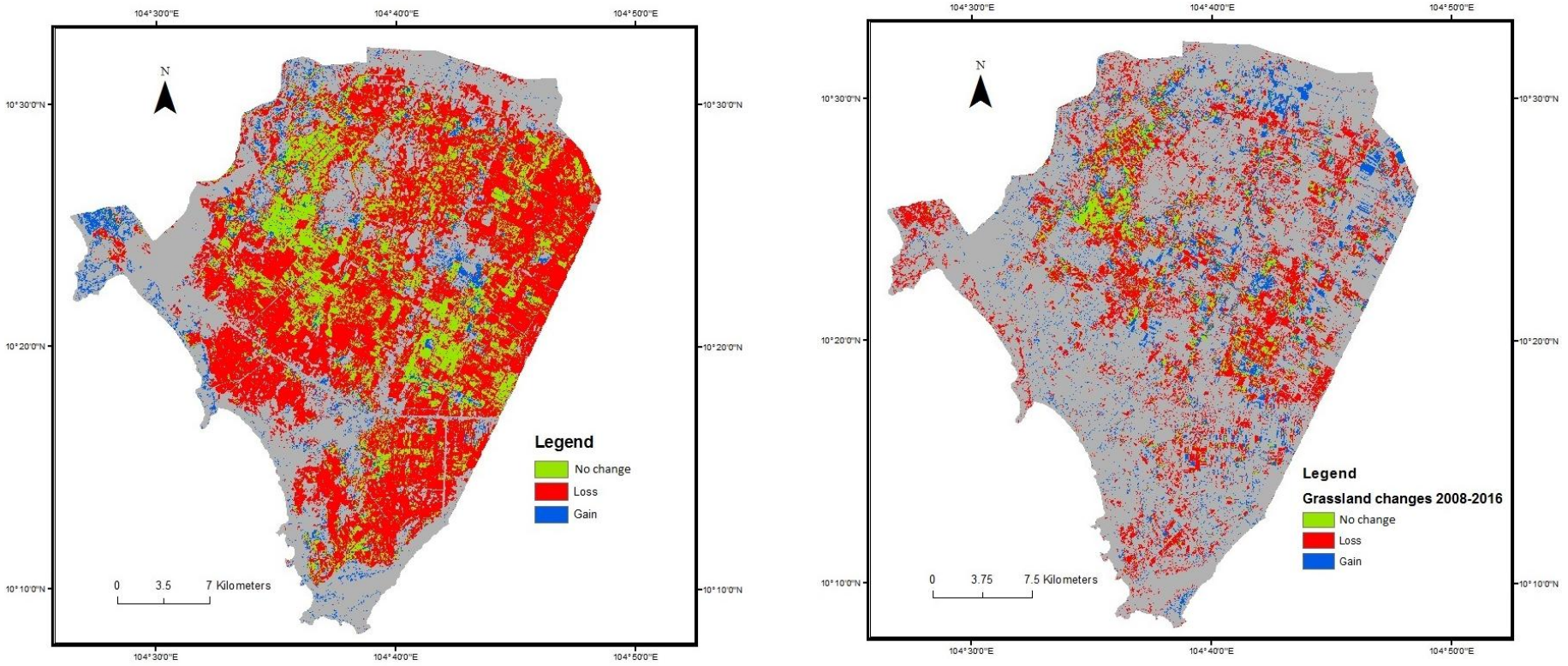

(a) (b)

Figure 4.12 Change of grassland: (a) 1998 - 2008 period (b) 2008 - 2016 period

4.2.3 Flood extent change

4.2.3.1 Performance of MFCM in MNDWI for water extraction

Figures 4.14 and 4.15 illustrate the MNDWI of Landsat data and the results of applying MFCM to MNDWI bands. In addition, Figures 4.16a and 4.16b show the two sub-images of MNDWI and MFCM-MNDWI. It is seen from the histogram of MNDWI that there are many pixels with water index values ranging from 0.2 to 0.4, which constitute mixed pixels (Figure 4.16a). In contrast, the histogram of MFCM-MNDWI illustrates the number of mixed pixels is dramatically decreased. By visual inspection, there is a much sharper contrast between water and non-water classes in the MFCM-MNDWI band (Figure 4.16b).

4.2.3.2 Flood extent map and validation

a. Flood extent maps

Flood extent mapping in 1999 and 2013 are presented in Figure 4.18. The two years were chosen because their floods were normal – that is, neither extreme nor drought relative to long-term average water level. Figure 4.17 illustrates the water level recorded at Tan Chau gauging station in 1999 was equal to the average water level of the 1977-2000 period, roughly 410 cm. In addition, the Mekong River Commission noted that the flood season throughout the Mekong region in 2013 was average (MRC, 2013a). The highest water level recorded at Tan Chau on 8 October 2013 by the Regional Flood Management and Mitigation Centre was 422 cm (MRC, 2013b). It is observed from Table 4.17 that 75.26 % (714.61 km^2) of the study area was inundated at the flood peak in 1999, whereas it was 51.04 % (484.64 km^2) in 2013. In addition, permanent water bodies found in 1999 were just over 4% (38.59 km^2) compared to more than 14 % (135.28 km^2) in 2013, whereas the area of non-flood increased from 20.68% (196.36 km^2) to 34.72% (329.64 km^2). Permanent water bodies in both years were mainly distributed in the southern, southwestern and western areas of the study area. Furthermore, the areas with many limestone hills could not be affected by flood water.

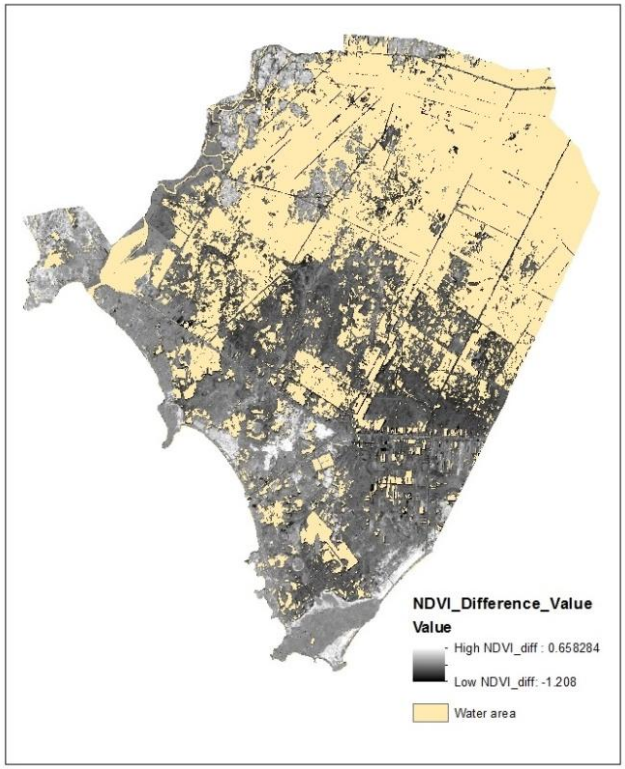

Figure 4.13 Differences in NDVI

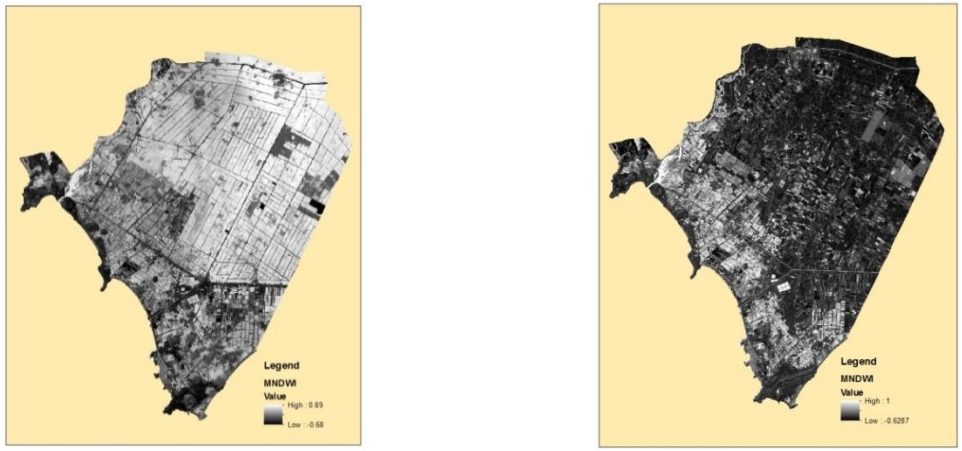

Figure 4.14 MNDWI calculated from Landsat 8 OLI images

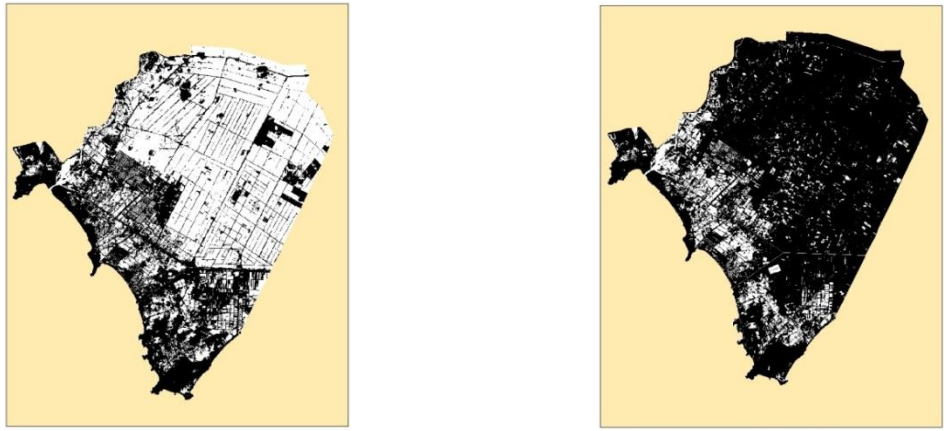

Figure 4.15 Water cluster by MFCM

MNDWI result

MFCM-MNDWI result

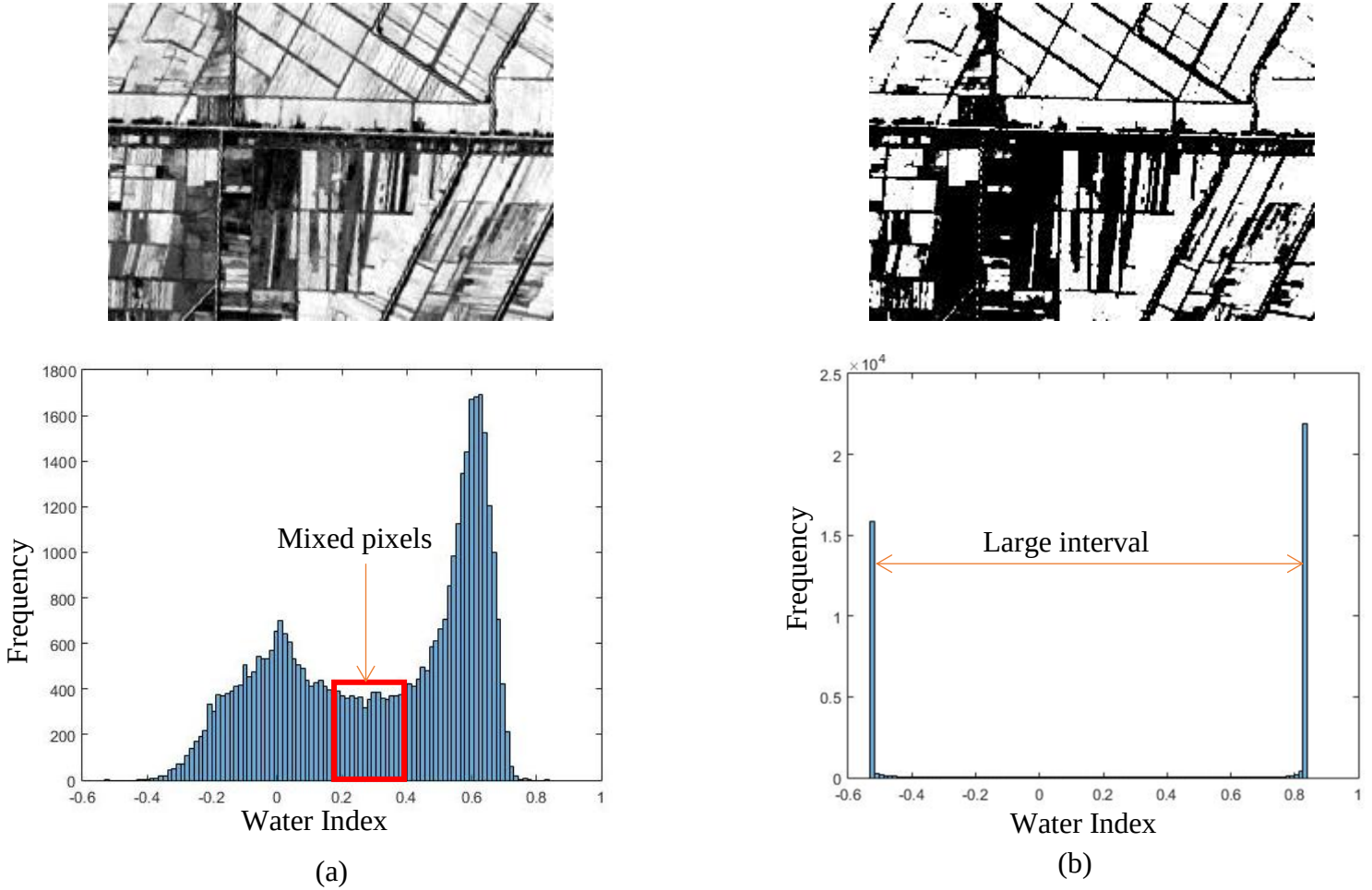

Figure 4.16 (a) Histogram of MNDWI and (b) MFCM-MNDWI results

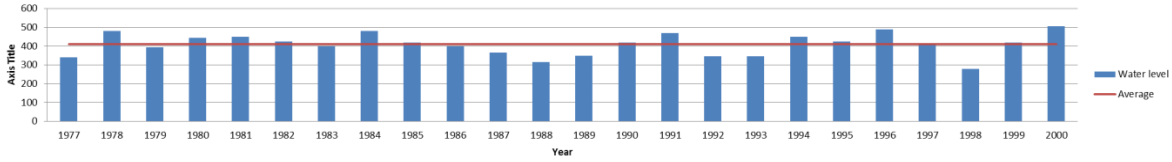

Figure 4.17 Flood peaks in Tan Chau gauging stations during 1977-2000 (Le et al., 2007)

Table 4.17 Flood-inundated matrix showing the change of flooded area during peak flood of 1999 and 2013 (%)

		Flood extent in 1999				
		Flood Water	Permanent Water	Non-flood	Sum	Total Class
Flood extent in 2013	Flood Water	484875	4202	49412	538489	51.04
	Permanent Water	98283	22256	29773	150312	14.25
	Non-flood	210848	16425	138996	366269	34.72
	Total	794006	42883	218181	1055070	
	Stable	61.07	51.90	63.71		
	Total class	75.26	4.06	20.68		

Table 4.18 Flood-inundated matrix showing the change of flooded area during peak flood of 1999 and 2013 (km^2)

		Flood extent in 1999			
		Flood Water	Permanent Water	Non-flood	Total class
Flood extent in 2013	Flood Water	436.39	3.78	44.47	484.64
	Permanent Water	88.45	20.03	26.80	135.28
	Non-flood	189.76	14.78	125.10	329.64
	Total class	714.61	38.59	196.36	

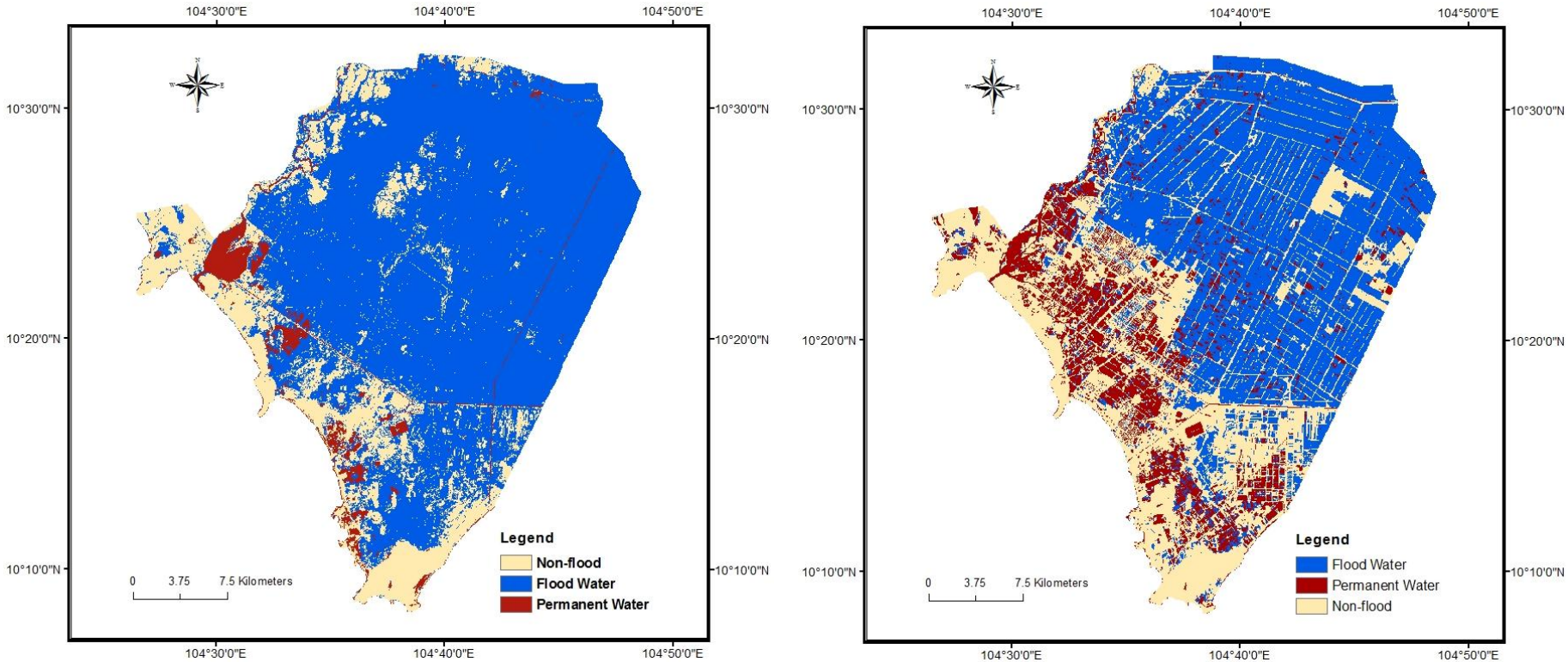

Figure 4.18 Peak flood inundation maps (a) 1999 and (b) 2013

b. Validation of flood-inundated maps

In order to validate the flood extent map of 2013, 60 reference samples with 26,159 pixels for water and non-water were randomly created by digitizing 15 m resolution pan-sharpened MS images. In addition, a quantitative comparison of MFCM-MNDWI and Maximum Likelihood (ML) was undertaken at per-pixel level for a complete method evaluation.

Table 4.19 Confusion matrix of classifying flooded area by using the Maximum Likelihood method (%)

		Reference data			
		Water	Non-water	Total	User Accuracy
Classification	Water	13976	147	14123	99.0
	Non-water	4452	7584	12036	63.0
	Total	18428	7731	26159	
	Producer Accuracy	75.8	98.1		
	Overall accuracy	82.4			
	Kappa coefficient	0.6			

Table 4.19 shows that overall accuracy and kappa coefficient of the ML method were 82.4% and 0.6, respectively. Moreover, nearly one third of water areas were misclassified which in turn leads to an underestimation of the flood-inundated area. This is due to the incapacity of an optical sensor like TM to detect water under thick forest canopies. Another reason is mixed pixels with a low contrast. These pixels deteriorated the performance of ML classifier. For the flood extent map produced by MFCM-MNDWI method, the overall accuracy and kappa coefficient were 91.1% and 0.9, respectively (Table 4.20). Only 7.4 % of water areas were not detected.

Table 4.20 Confusion matrix of classifying flooded area using the modified fuzzy c-mean MNDWI based approach

In %	Water	Non-water	Total	User Accuracy
Water	17066	958	18024	94.7
Non-water	1362	6773	8135	83.3
Total	18428	7731	26159	
Producer Accuracy	92.6	87.6		
Overall Accuracy	91.1			
Kappa Coefficient	0.8			

For the validation of the flood map of 1999, the classification result derived from Landsat 7 ETM scenes were utilized. Two Landsat 7 ETM + acquired on 8th September and 10th October 1999 were pansharpened to achieve the higher spatial resolution of 15 m before being used to map the flood extent. The result of accuracy assessment is illustrated in Table 4.21

Table 4.21 Validation of the flood map of 1999 using the flood map produced by classifying pansharpened Landsat 7 ETM as reference

In %	Water	Non-water	Total	User Accuracy
Water	18795	1682	20477	91.8
Non-water	723	4951	5674	87.2
Total	19518	6633	26151	
Producer Accuracy	96.3	74.6		
Overall Accuracy	90.8			
Kappa Coefficient	0.74			

5 DISCUSSIONS

One of the main targets of this research was to assess the degradation of wetlands in the VMRD. The experimental results revealed rates of grassland cover decreased at 7.2% $year^{-1}$ and 9.8% $year^{-1}$ during the 1998-2008 period and the 2008-2016 period, respectively. The 1998-2008 period experienced a decrease of 72% in grassland. This is comparable to that observed by Funkenberg *et al.* (2014). They indicated 77% grassland lost from 1991 to 2009. The loss of wetland could be due to the *Doi Moi* (renovation) reform in general and the environmental policy in particular. Under the renovation, the Land Law promulgated in 1993 recognizes grassland areas for unused land which were allowed to be converted to agriculture, forest plantation, and aquaculture (Law, 1993). Also, the government of Vietnam approved a planning for developing irrigation, transport and communication systems in rural areas of Vietnam Mekong River Delta over the period 1996-2000 (Decision 99/TTg of the Prime Minister 1996). As a result, dyke system, roads, and buildings have been constructed. These facilitate agricultural intensification during the first period and diversification later to be undertaken. Grassland areas, therefore, have been converted into agriculture and aquaculture. The results indicated a large loss of grassland in the study area since 1998. Agricultural diversification with aquaculture sector which experienced a much faster growth than rice and other crops (Garschagen et al., 2012) may lead a higher rate of decrease in grassland during the 2008-2016 period (9.8%). Furthermore, according to Funkenberg et al. (2014), forest wetlands have received many efforts for protection, while non-forest wetlands like grassland in the study area are neglected. This is confirmed through the results of this research, which indicate that the loss of forest happened at a smaller rate than that of grassland.

The better performance of classification using fused images over original data was confirmed by this research. There are several important points to note about the accuracy of classifying the wetland by using original Landsat data. Wetlands are considered as one of the most diverse environments with many small communities of species which build a heterogeneous pattern. The usage of Landsat data with limited spatial resolution to map the wetland area might therefore lead to unsatisfactory classification accuracy. Visual inspection illustrated that several land cover types such as vegetation along canals and recently cleared forest plantations could not be detected

because of their too small extent. In addition, the confusion between ploughed fields and bare areas, and post-harvested rice parcels and grassland led to further misclassification. Information about the crop calendar can be useful to clarify the source of classification errors in this research. As double-rice cropping is mainly planted in the Vietnam Mekong River Delta (VMRD) (Kuenzer et al., 2013; Nguyen et al., 2015), the crop calendar of the study area shows that the first rice cropping season, called Winter-Spring, is from late November to early February and the second season called Spring-Summer, is from April to June. Between the two seasons are two periods of crop transition in which land fields are normally ploughed. In 1998, agriculture was in early development and grassland and forest were cleared for the conversion to agriculture. The ancillary data and high resolution images from Google Earth proved that they were bare areas, but were identified as ploughed fields by the classifier. This led to the commissioning of artificial surface and agriculture. In 2008, on the date of image acquisition 1 April, the study area was in the late crop transition, from Winter-Spring to Spring-Summer. Some rice fields were sowed but several others were still ploughed. Thus, the confusion of bare soil with ploughed field could result in low accuracy for artificial surface.

The comparison between two wavelet-based fusion schemes, IHS and wavelet, and PCA and wavelet, demonstrated that the PCA-wavelet method performed better than the IHS-wavelet when they were applied to integrate Landsat data and SAR data. Furthermore, two models of injecting spatial information extracted from SAR data into MS images, namely full combination and weighted combination models, were utilized in the fusion procedure. Experimental results illustrated that the two fusion methods with both injection models performed well with fast processing time and low complexity. However, spectral distortion occurred in all cases. Colour distortion was introduced into the resulting products because of significant differences in gray values between SAR and MS images. This inevitable issue is due to different characteristics of sensors. The efficiency of colour preservation depends on the amount of fusion data. As the relationship between the spectral and spatial resolutions is inverse (El-Mezouar et al., 2011), the more spatial information to be fused, the more spectral distortion occurs. It is noted that PCA is a data reduction technique. Although the IHS smoothly integrated the spatial resolution information, it could not reduce the amount of

redundancy in information of adjacent MS bands. In addition, a comparison between the two models of injection revealed that the fused images produced by the full combination model were more distorted in spectral value than those produced by the weighted integration model. This could be due to the former injecting more spatial information extracted from SAR data into fused products than the latter. However, the spectral distortion in fused products obtained by using both models was satisfactory. In addition, the full combination model performed maximal integration of SAR features. It is noted that the full combination model is to improve class distinctiveness (Chibani, 2007). Therefore, this model was chosen to integrate SAR and MS images in this research.

Experimental results showed that Landsat and SAR fused images improved the accuracy of classification results of wetlands. This is comparable to other studies. For example, the fusion of SPOT and Radarsat images improved the correct classification rate when being compared to initial images (Chibani, 2007), whilst ASTER and ALOS PALSAR fused images improved the overall accuracy of classifying the wetland in the Tonle Sap, Cambodia by 5.9% (Nguyen, 2012). In order to explain the improvement of classification accuracy, the enhancement of spatial resolution and SAR's texture features were taken into account. The higher spatial resolution of fused products facilitates the process of defining ROIs for classification. In addition, while the similarities in spectral value of some classes could lead to the abovementioned confusions when using optical data, texture features extracted from SAR images before injecting into MS images may tackle this. The results demonstrated that fused images facilitated the discrimination between ploughed fields and bare land. Furthermore, more water pixels were detected from fused images. This is likely due to the gamma backscatter coefficient of water being much lower than that of other classes. In spite of certain improvements as mentioned above, rates of classification accuracy increase were not significant. The improvement of spatial resolution was probably insufficient to have a higher thematic differentiation of land cover types. In addition, the fusion products have both strengths and weaknesses of each image source (Furtado et al., 2015). One of the weaknesses could be the remaining noise from SAR data injected into fused images. When using the pixel based classification method, this noise and the increase of spatial resolution produced maps with a "pepper and salt" problem

(Ouyang et al., 2011). Therefore, the object based classification method can potentially be an approach to correct this problem.

The physical boundary of water and non-water is continuous and ambiguous (Yang et al., 2015). Therefore, a hard threshold method may produce uncertainty in drawing this boundary (Comber et al., 2012; Foody et al., 2005). In this study, such a boundary was identified using a fuzzy c-means (FCM) method, which offers a flexible approach to separate water and non-water categories. Physically, this boundary is unlikely in a hard line and the map producer can determine what extent it is unlikely on a scale of '0' to '1', thus it can be identified as a continuum of water and non-water boundary. While FCM is sensitive to noise, a modified fuzzy c-means (MFCM) in which a spatial weight is incorporated in the calculation of membership value can fix the noise related problems. The experimental results indicated that the application of MFCM on the modified normalized difference water index (MNDWI) could tackle the problems of mixed pixels which are common in medium resolution remote sensing images over wetlands. Mixed pixels are the representation of the spectral and spatial variability of wetland environment. This problem may be more serious for the condition of flooding. Mixed pixels represent areas where land cover types such as vegetation and bare soil are under shallow inundated flood. In addition, flood water from Mekong River has a high level of turbidity which leads to the inundated flood area with mixed pixels in its covering images. While the NIR band is affected by the high level of turbidity (Ryu et al., 2002), the SWIR band can reduce the effect of turbid flood water (Frazier and Page, 2000), therefore MNDWI, a band ratio of SWIR band, was more appropriate than the normalized difference water index (NDWI) in this study. Experimental results showed that the ML method could not classify floodwater effectively, whereas the MFCM-MNDWI method successfully extracted floodwater. As the optical sensor cannot penetrate forest canopy both methods had the same limitation of underestimation of flooded areas. In addition, some canals have a width of less than 30 m, which makes Landsat images harder to classify accurately. The MFCM might consider these pixels as noise, causing them to be ignored. This could lead to the underestimation of inundated flood area using the MFCM-MNDWI method. To address this issue, missing canals were digitised as they are linear objects. Another

approach could be a new modified fuzzy c-means algorithm in which such narrow linear objects are identified.

For the year 1999, the limitation of data collection due to clouds leads to an unavailability of Landsat 5 TM images covering flood peak. However, with a free cloud scene captured a few weeks after peak flood event, the flood extent was delineated successfully. The study area was covered mainly by grassland which was inundated by flood during the rainy season. After flood water receded, the inundated flood vegetation was covered by sediment or mud which in turn reduced the NDVI value. The change in the NDVI value before and after flood event was used to estimate flooding areas. The flood regime in the VMRD is extremely complicated and requires a large amount of earth observation data and ancillary data to visualize, interpret, and understand it (Kuenzer et al., 2013). Thus, the limitation of data in this research posed difficulties in understanding the relationship between flood regime and wetlands over the study area. Geographically, the study area is the furthest away from the west of the VMRD. Floods in the area are categorized into less impacted or downstream flood (Kuenzer et al., 2013; Tran, 2005). Therefore, the positive side effects of floods outweigh the negative effects. However, the changes of land cover in the area during the study period caused a significant shift of the flood regime in terms of its extent. The result of this study showed the conversion of grassland into agriculture, forest plantations, and water. In addition, several studies noted that the conversion of grassland to water was due to the development of aquaculture, mainly shrimp ponds (BirdLife International, 2004; Buckton et al., 1999; Triet et al., 2000). The extension of the canal system, indicated by dykes, roads, and buildings along the canals (Funkenberg et al., 2014) are to help farmers control floodwaters (Kuenzer et al., 2013). The result of the study demonstrated an extension of aquaculture over the southern and south-western parts of the study area which was previously inundated by floodwater during the rainy season. As floodwater could not naturally reach these areas, they may not benefit the flood's positive side effects. Such benefits include fertilizing farming land with sediments, seasonal fishing, and flushing of fields to tackle diseases, algae, and agro-chemicals (Tran, 2005).

6 CONCLUSIONS AND RECOMMENDATIONS

6. 1 Conclusions

Wetlands in the VMRD play an important role in the preservation of biodiversity. In order to protect wetlands, it is necessary to have detailed information on which to base protection and management actions. While laborious field surveys are expensive and less practical, remote sensing is an effective method to collect information on wetlands. The research presented in this thesis identified four main findings based on temporal Landsat data, SAR data acquired by various sensors, and further ancillary information:

(i) Multi-sensor images fused by using a hybrid method of wavelet and PCA can be used to map wetland areas over time;

(ii) Grassland in wetlands in the VMRD have been reducing at an increasing rate in recent decades due to the intensification of agriculture and aquaculture;

(iii) A modified fuzzy c-means algorithm can be applied to optical data to map flood-inundated areas with satisfactory accuracy; and

(iv) The change of wetland's land cover reduces the extent of natural floods.

The study has performed the integration of three pairs of multi-source images being; Landsat 5 TM and ERS-2, Landsat 5 TM and ALOS PALSAR, and Landsat 8 OLI and Sentinel 1 images, over a wetland in the VMRD. Two hybrid fusion methods of wavelet were used, namely IHS-wavelet and PCA-wavelet. The study revealed that PCA-wavelet is better than IHS-wavelet in reducing spectral distortion. When spatial details derived from SAR data were injected into MS images, weighted combination and full integration models were employed. Images fused by the weighted combination model were less distorted in spectrum than those by the full integration model but they contained less spatial information. While both models preserved spectral values, the full integration model was the best choice for the model of injection in PCA-wavelet method. The Landsat and SAR fused images were used to map the wetland's land cover and improve the classification accuracy.

The study reveals that grassland in the study area has been decreasing due to the conversion into agriculture, forest plantation, and aquaculture. Specifically, the period

from 1998 to 2008 experienced a significant loss of 72% with an annual rate of 7.2%. The area of grassland continues reducing but with a higher annual rate of 9.8%. This corresponds to an increasing intensification, and then diversification in agriculture in the area.

This study introduced a modified fuzzy c-means based approach for mapping the inundated flood area using Landsat data. The modified fuzzy c-means implemented on MNDWI band of Landsat data attempted to overcome problems caused by mixed pixels that are common in images covering flood inundated wetlands. By comparing to the flood map produced by the ML method, the method produced more accurate classification of the flood water. The study showed that the change of wetland's land cover impacts on the flood extent. Furthermore, natural floods cannot inundate several areas due to the canal systems such as dykes, channels, and roads.

6. 2 Recommendations

The research utilized three different SAR images with spatial resolutions ranging from 12-25 m. Therefore, the fusing products' spatial resolutions were increased to these resolutions. Given that the higher resolution SAR data might become more available with low cost and easier access in the near future, the integration of these high resolution images and the medium resolution optical data such as Landsat, ASTER, and SPOT are recommended for trial. This would enable the discrimination of more classes in a complex wetland environment. As fused images contain texture features from SAR data, an object oriented method might be more robust as it includes such variables as shape, size, scale, and colour.

During the flood season, the area is normally covered by cloud, which limits the flood inundation mapping by optical data. In addition, the temporal resolution of Landsat data is not sufficient to derive flood occurrence and flood progression. Therefore, it is recommended that high temporal resolution and weather independent SAR data should be used.

The proposed modified fuzzy c-means based flood-mapping method has a disadvantage of omitting narrow canals as the modified c-means algorithm considers

their pixels as noise. The development of an algorithm in which small linear objects like canals can be identified will be ideal for future works.

The reasons for the degradation of the study wetland are mainly the intensification of agriculture and aquaculture. In order to preserve the remaining wetland areas, the conservation of the remaining grassland patches should be given more attention. The positive role of floodwater on the area is undeniable, therefore the canal system with gates of dykes should be controlled wisely. This might help to reduce negative impacts of the canal system.

APPENDIX A

IMAGE FUSION MATLAB CODE

1. The PCA-wavelet fusion

```
SAR =double(imread('Sentinel1.tif'));
B1 = double(imread('B1.tif'));    % blue band ;
B2 = double(imread('B2.tif'));    % green band
B3 = double(imread('B3.tif'));    % red band
B4 = double(imread('B4.tif'));  % near infrared band
B5 = double(imread('B5.tif'));
B6 = double(imread('B7.tif'));
% Creation of the data matrix, containing different layer as columns
% that will be submitted to PCA. Image vectors creation:
[nrow,ncol] = size(B1);
B1_v = reshape(B1,nrow*ncol,1);
B2_v = reshape(B2,nrow*ncol,1);
B3_v = reshape(B3,nrow*ncol,1);
B4_v = reshape(B4,nrow*ncol,1);
B5_v = reshape(B5,nrow*ncol,1);
B6_v = reshape(B6,nrow*ncol,1);
dt_matrix = [B1_v B2_v B3_v B4_v B5_v B6_v];
covariance = cov(dt_matrix);
% eigenvectors and eigenvalues:
[Va,D] = eig(covariance);
Va_c = zeros(size(Va));
Va_c(:,1) = Va (:,6);
Va_c(:,2) = Va (:,5);
Va_c(:,3) = Va (:,4);
Va_c(:,4) = Va (:,3);
Va_c(:,5) = Va (:,2);
Va_c(:,6) = Va (:,1);
D_c = [D(6,6) 0 0 0 0 0; 0 D(5,5) 0 0 0 0; 0 0 D(4,4) 0 0 0; 0 0 0 D(3,3) 0 0; 0 0 0 0
D(2,2) 0; 0 0 0 0 0 D(1,1)];
```

```
y = (D_c*Va_c'*dt_matrix')';
% Extraction of the obtained principal components:
PC1_v = y(:,1);
PC1 = reshape(PC1_v,nrow,ncol);
PC2_v = y(:,2);
PC2 = reshape(PC2_v,nrow,ncol);
PC3_v = y(:,3);
PC3 = reshape(PC3_v,nrow,ncol);
PC4_v = y(:,4);
PC4 = reshape(PC4_v,nrow,ncol);
PC5_v = y(:,5);
PC5 = reshape(PC5_v,nrow,ncol);
PC6_v = y(:,6);
PC6 = reshape(PC6_v,nrow,ncol);
% Computation of mean and standard deviation of band PC1:
PC1_mean = mean(PC1(:));
PAN_std = std(PC1(:));
% Computation of mean and standard deviation of the
S_mean = mean(SAR(:));
S_std = std(SAR(:));
[Snrow,Sncol] = size(SAR);
S_mod = zeros(size(SAR));
for k = 1:Snrow
   for m = 1:Sncol
      S_mod(k,m) = (PAN_std/S_std)*(SAR(k,m)-S_mean)+PC1_mean;
   end
end
min(S_mod(:))
max(S_mod(:))
% Apply ATW to new PAN and PC1 image: Undecimated algorithm
[SA SD] = a_trous_dwt(S_mod,2);
[PANA PC1D] = a_trous_dwt(PC1,2);
% Weighted combination
```

```
PSA = std2(SA)^2 /(std2(SA)^2 + std2(PANA)^2) *PANA + std2(PANA)^2
/(std2(SA)^2 + std2(PANA)^2)*SA;
DF(:,:,1) = SD(:,:,1);
DF(:,:,2) = SD(:,:,2);
% Inverse transform to obtain fused PC1 component:
PC1F2 = a_trous_idwt(PSA, DF);
% Fused PC1 component band substitutes the band PC1 in the transformed data matrix
PC2F2_v = reshape(PC1F2, nrow*ncol,1);
y(:,1) = PC2F2_v;
% Principal component anti-transformation of matrix y (bands are taken back in
% their original positions in the 6-dimensional space):

w = (V_c*inv(D_c)*y')';
% Extraction of the 6 fused bands:
 B1_final_v = w(:,1);
 B1_final = reshape(B1_final_v,nrow,ncol);
%
 B2_final_v = w(:,2);
 B2_final = reshape(B2_final_v,nrow,ncol);
%
 B3_final_v = w(:,3);
 B3_final = reshape(B3_final_v,nrow,ncol);
%
 B4_final_v = w(:,4);
 B4_final = reshape(B4_final_v,nrow,ncol);
%
 B5_final_v = w(:,5);
 B5_final = reshape(B5_final_v,nrow,ncol);
%
 B6_final_v = w(:,6);
 B6_final = reshape(B6_final_v,nrow,ncol);
```

APPENDIX B

THE MODIFIED FUZZY C-MEANS MATLAB CODE

1. The code of the main program:

```
InputIm = imread('MNDWI.tif');
InputIm = double(InputIm);
ncluster=2;
[r,c] = size(InputIm);
[MFV, Cent]= SWFCM(InputIm,2);
cc = sum(MFV);
tt = MFV'*Cent;
imag = tt./cc';
% Write the output image files:
path = 'H:\ MNDWI_Results\';
fileformat = '.tif';
mainname = 'CltMNDWI_Test';
for i = 1 : ncluster
    filenames = [path int2str(ncluster) mainname int2str(i) fileformat];
    Reshp_MF = reshape(MFV(i,:),r,c);
    Reshp_MF = (Reshp_MF - min(Reshp_MF(:))) ./ (max(Reshp_MF(:)) -
min(Reshp_MF(:)));
    imwrite(Reshp_MF, filenames);
end
```

2. The code of the modified fuzzy c-means

```
function [U_joint,Cent_W]=SWFCM(img,ncluster,max_it,expo,spw,mfw,nwin)
% Written by CXC
%   img: image;       ncluster: the number of desired cluster;
%   U_joint: partition matrix;       Cent_W: cluster centers
if nargin<4
   expo=2;    spw =2;     mfw =2;     nwin =3;
   if nargin<3
      max_it=100;
   end
```

```
end
[r,c]=size(img);
imgv= reshape(double(img),r*c,1);
Cent_v = int_c(imgv,ncluster);
Cent_W = Cent_v;
% Main loop
epmin=1e-6;
iter=1;
while iter < max_it
   dist = distfcm(Cent_v,imgv);
   U = mf_u(dist,ncluster,expo);
   U_joint = mf_joint(U,[rn,cn],spw,mfw,nwin,ncluster);
   Cent_joint =upd_c(imgv,U_joint,expo);
   Cent_v = upd_c(imgv,U,expo);
   e =Cent_joint-Cent_W;
   e =max(abs(e(:)));
   if e <= epmin
      iter=max_it;
   else
      Cent_W=Cent_joint;
      iter = iter+1;
   end
end
```

APPENDIX C

LAND CODES ON CURRENT LAND USE MAPS

(Decision 23/2007/QD-BTNMT of Ministry of Natural Resources and Environment)

Code	Description
LUC	Land for cultivation of main rice crops
LUK	Land for cultivation of other rice crops
COC	Grazing land
HNK	Land for cultivation of other annual crops
BHK	Lowland for cultivation of other annual crops
NHK	Upland for cultivation of other annual crops
CLN	Land for cultivation of perennial trees
LNC	Land for cultivation of perennial trees used for industrial production
LNQ	Land for fruit trees
LNK	Land for cultivation of other perennial trees
RSN	Land with natural production forests
RST	Land for planting forests
RSK	Land for replanting forests
RSM	Land for planting production forests
RPH	Land for protection forests
RPT	Land with planting protection forests
RPK	Land for replanting protection forests
RDN	Land with natural forest for special purposes
RDT	Land with planting forest for special purposes
RDK	Land with replanting forest for special purposes
NTS	Land for aquaculture
TSL	Land for saline aquaculture
TSN	Land for freshwater aquaculture
NKH	Land for other agricultural production
PNN	Non-agricultural land
ONT	Rural residential land
ODT	Urban residential land
CTS	Land for construction of offices of non-business units
TSC	Land for construction of offices
TSK	Land for construction of other offices
SKK	Land for industrial parks
SKC	Land for trading and service
SKS	Land used for mining activities
SKX	Land for production of building materials, and pottery
CCC	Land used for public purposes
DGT	Land used for transport
DTL	Land for irrigation
DBV	Land for post and telecommunications facilities
DVH	Land for construction of cultural facilities

DYT	Land for construction of health facilities
DGD	Land for construction of education and training facilities
DTT	Land for construction of sport facilities
DXH	Land for construction of social service facilities
DCH	Land for construction of markets
DDT	Land with historical-cultural relics or scenic spots
DRA	Land for waste dumping and treatment
TTN	Land used by religious institutions
TON	Land used for religious purposes
TIN	Land used for beliefs
NTD	Land used for cemeteries, funeral service centers and cremation centers
SMN	Land with rivers, streams, canals, springs and special-use water surface
SON	Land with rivers, streams, canals, springs
MNC	Land with special-use water surface
PNK	Land for non-agricultural production
BCS	Unused lowland
NCS	Rocky mountains
MVK	Coastal land with water surface for other purposes

REFERENCES

Abdikan, S., Balik Sanli, F., Sunar, F., & Ehlers, M. (2014). A comparative data-fusion analysis of multi-sensor satellite images. *International Journal of Digital Earth, 7*(8), 671-687. doi:10.1080/17538947.2012.748846

Adam, E., Mutanga, O., & Rugege, D. (2009). Multispectral and hyperspectral remote sensing for identification and mapping of wetland vegetation: a review. *Wetlands Ecology and Management, 18*(3), 281-296. doi:10.1007/s11273-009-9169-z

Adhikari, S. K., Sing, J. K., Basu, D. K., & Nasipuri, M. (2015). Conditional spatial fuzzy C-means clustering algorithm for segmentation of MRI images. *Applied Soft Computing, 34*, 758-769. doi:http://dx.doi.org/10.1016/j.asoc.2015.05.038

Agency, E. S. (2014). Sentinel 1 Overview. Retrieved from https://earth.esa.int/web/sentinel/missions/sentinel-1/overview

Alparone, L., Wald, L., Chanussot, J., Thomas, C., Gamba, P., & Bruce, L. M. (2007). Comparison of Pansharpening Algorithms: Outcome of the 2006 GRS-S Data-Fusion Contest. *IEEE Transactions on Geoscience and Remote Sensing, 45*(10), 3012-3021. doi:10.1109/TGRS.2007.904923

Amarsaikhan, D., Saandar, M., Ganzorig, M., Blotevogel, H. H., Egshiglen, E., Gantuyal, R., . . . Enkhjargal, D. (2012). Comparison of multisource image fusion methods and land cover classification. *International Journal of Remote Sensing, 33*(8), 2532-2550. doi:10.1080/01431161.2011.616552

Amolins, K., Zhang, Y., & Dare, P. (2007). Wavelet based image fusion techniques — An introduction, review and comparison. *ISPRS Journal of Photogrammetry and Remote Sensing, 62*(4), 249-263. doi:http://dx.doi.org/10.1016/j.isprsjprs.2007.05.009

Anh Tuan Le, Thai Hoang Chu, F Miller, & Bach, T. S. (2007). Flood and salinity management in the Mekong Delta, Vietnam. In T. S. B. Thanh Be Tran, F Miller (Ed.), *Challenges to sustainable development in the Mekong Delta: regional and national policy issues and research needs* (pp. 15-68). Bangkok.

Bartsch, A., Wagner, W., Scipal, K., Pathe, C., Sabel, D., & Wolski, P. (2009). Global monitoring of wetlands – the value of ENVISAT ASAR Global mode. *Journal of Environmental Management, 90*(7), 2226-2233. doi:http://dx.doi.org/10.1016/j.jenvman.2007.06.023

Behera, M. D., Chitale, V. S., Shaw, A., Roy, P. S., & Murthy, M. S. R. (2012). Wetland Monitoring, Serving as an Index of Land Use Change-A Study in Samaspur Wetlands, Uttar Pradesh, India. *Journal of the Indian Society of Remote Sensing, 40*(2), 287-297. doi:10.1007/s12524-011-0139-6

BirdLife International. (2004). *Sourcebook of Existing and Proposed Protected Areas in Vietnam* (2 ed.): Cambridge: Birdlife International.

Brivio, P. A., Colombo, R., Maggi, M., & Tomasoni, R. (2002). Integration of remote sensing data and GIS for accurate mapping of flooded areas. *International Journal of Remote Sensing, 23*(3), 429-441. doi:10.1080/01431160010014729

Buckton, S. T., N. Cu, H. Q. Quynh, & Tu, a. N. D. (1999). *The Conservation of Key Wetland Sites in the Mekong Delta* (12). Retrieved from Hanoi: https://data.opendevelopmentmekong.net/dataset/fd1e8de3-f284-4466-b72e-0232a02b5728/resource/da53ec24-ee67-461a-a953-5b8754be6fef/download/report12.pdf

Byun, Y., Choi, J., & Han, Y. (2013). An Area-Based Image Fusion Scheme for the Integration of SAR and Optical Satellite Imagery. *Selected Topics in Applied*

Earth Observations and Remote Sensing, IEEE Journal of, 6(5), 2212-2220. doi:10.1109/JSTARS.2013.2272773

Castañeda, C., & Ducrot, D. (2009). Land cover mapping of wetland areas in an agricultural landscape using SAR and Landsat imagery. *Journal of Environmental Management, 90*(7), 2270-2277. doi:http://dx.doi.org/10.1016/j.jenvman.2007.06.030

Chadde, J. (2006). Wetland ecosystems. *Michigan Environmental Education Curriculum.*

Chibani, Y. (2006). Additive integration of SAR features into multispectral SPOT images by means of the à trous wavelet decomposition. *ISPRS Journal of Photogrammetry and Remote Sensing, 60*(5), 306-314. doi:http://dx.doi.org/10.1016/j.isprsjprs.2006.05.001

Chibani, Y. (2007). Integration of panchromatic and SAR features into multispectral SPOT images using the 'à trous' wavelet decomposition. *International Journal of Remote Sensing, 28*(10), 2295-2307. doi:10.1080/01431160600606874

Chibani, Y., & Houacine, A. (2003). Redundant versus orthogonal wavelet decomposition for multisensor image fusion. *Pattern Recognition, 36*(4), 879-887. doi:http://dx.doi.org/10.1016/S0031-3203(02)00103-6

Comber, A., Fisher, P., Brunsdon, C., & Khmag, A. (2012). Spatial analysis of remote sensing image classification accuracy. *Remote Sensing of Environment, 127*, 237-246. doi:http://dx.doi.org/10.1016/j.rse.2012.09.005

Danaher, T., Xiaoliang, W., & Campbell, N. (2001, 2001). *Bi-directional reflectance distribution function approaches to radiometric calibration of Landsat ETM+ imagery.* Paper presented at the Geoscience and Remote Sensing Symposium, 2001. IGARSS '01. IEEE 2001 International.

Dao, D. P., & Liou, Y.-A. (2015). Object-Based Flood Mapping and Affected Rice Field Estimation with Landsat 8 OLI and MODIS Data. *Remote Sensing, 7*(5). doi:10.3390/rs70505077

Dewan, A. M., Yamaguchi, Y., & Rahman, Z. M. (2012). Dynamics of land use/cover changes and the analysis of landscape fragmentation in Dhaka Metropolitan, Bangladesh. *GeoJournal., 77*(3), 315-330. Retrieved from http://search.proquest.com/docview/1431613467?accountid=10382

http://link.library.curtin.edu.au/openurl??url_ver=Z39.88-2004&rft_val_fmt=info:ofi/fmt:kev:mtx:journal&genre=article&sid=ProQ:ProQ%3Aagricolamodule&atitle=Dynamics+of+land+use%2Fcover+changes+and+the+analysis+of+landscape+fragmentation+in+Dhaka+Metropolitan%2C+Bangladesh&title=GeoJournal.&issn=03432521&date=2012-06-01&volume=77&issue=3&spage=315&au=Dewan%2C+Ashraf+M%3BYamaguchi%2C+Yasushi%3BRahman%2C+Ziaur%2C+Md&isbn=&jtitle=GeoJournal.&btitle=&rft_id=info:eric/&rft_id=info:doi/

Do, T. N., & Bennett, J. (2009). Estimating wetland biodiversity values: a choice modelling application in Vietnam's Mekong River Delta. *Environment and Development Economics, 14*(02), 163-186.

Dutilleux, P. (1989). An Implementation of the "algorithme à trous" to Compute the Wavelet Transform *Wavelets* (pp. pp 298-304). Germany: Springer Berlin Heidelberg.

El-Mezouar, M. C., Taleb, N., Kpalma, K., & Ronsin, J. (2011). An IHS-Based Fusion for Color Distortion Reduction and Vegetation Enhancement in IKONOS Imagery. *IEEE Transactions on Geoscience and Remote Sensing, 49*(5), 1590-1602. doi:10.1109/TGRS.2010.2087029

Feng, Q., Gong, J., Liu, J., & Li, Y. (2015). Flood Mapping Based on Multiple Endmember Spectral Mixture Analysis and Random Forest Classifier—The Case of Yuyao, China. *Remote Sensing, 7*(9). doi:10.3390/rs70912539

Ferreira, L. G., & Huete, A. R. (2004). Assessing the seasonal dynamics of the Brazilian Cerrado vegetation through the use of spectral vegetation indices. *International Journal of Remote Sensing, 25*(10), 1837-1860. doi:10.1080/0143116031000101530

Finlayson, C. M., Davidson, N. C., & Stevenson, N. J. (1998). *Wetland inventory, assessment and monitoring : practical techniques and identification of major issues.* Paper presented at the International Conference on Wetlands and Development Dakar and Senegal.

Fisher, A., & Danaher, T. (2013). A Water Index for SPOT5 HRG Satellite Imagery, New South Wales, Australia, Determined by Linear Discriminant Analysis. *Remote Sensing, 5*(11). doi:10.3390/rs5115907

Foody, G. M., Muslim, A. M., & Atkinson, P. M. (2005). Super-resolution mapping of the waterline from remotely sensed data. *International Journal of Remote Sensing, 26*(24), 5381-5392. doi:10.1080/01431160500213292

Frazier, P. S., & Page, K. J. (2000). Water body detection and delineation with Landsat TM data. *Photogrammetric Engineering and Remote Sensing, 66(12),* 1461-1467.

Frost, V. S., Stiles, J. A., Shanmugan, K. S., & Holtzman, J. C. (1982). A Model for Radar Images and Its Application to Adaptive Digital Filtering of Multiplicative Noise. *IEEE Transactions on Pattern Analysis and Machine Intelligence, PAMI-4*(2), 157-166. doi:10.1109/TPAMI.1982.4767223

Funkenberg, T., Binh, T. T., Moder, F., & Dech, S. (2014). The Ha Tien Plain – wetland monitoring using remote-sensing techniques. *International Journal of Remote Sensing, 35*(8), 2893-2909. doi:10.1080/01431161.2014.890306

Furtado, L. F. d. A., Silva, T. S. F., Fernandes, P. J. F., & Novo, E. M. L. d. M. (2015). Land cover classification of Lago Grande de Curuai floodplain (Amazon, Brazil) using multi-sensor and image fusion techniques. *Acta Amazonica, 45,* 195-202.

Garg, J. K. (2013). Wetland assessment, monitoring and management in India using geospatial techniques. *Journal of Environmental Management*(0). doi:http://dx.doi.org/10.1016/j.jenvman.2013.12.018

Garschagen, M., Diez, J. R., Nhan, D. K., & Krass, F. (2012). Scocio-Economic Development in the Mekong Delta: Between the Prospects for Progress and the Realms of Reality. In F.G. Renaud & C. Kuenzer (Eds.), *The Mekong Delta System: Interdisciplinary Analyses of a River Delta* (pp. 83-132): Springer Environmental Science and Engineering.

Gong, P. N., ZhenGuo Cheng, Xiao Zhao, KuiYi Zhou, DeMin Guo, JianHong Liang, Lu Wang, XiaoFeng Li, DanDan Huang, HuaBing Wang, Yi Wang, Kun Li, WenNing Wang, XianWei Ying, Qing Yang, ZhenZhong Ye, YuFang Li, Zhan Zhuang, DaFang Chi, YaoBin Zhou, HuiZhen Yan, Jun. (2010). China's wetland change (1990–2000) determined by remote sensing. *Science China Earth Sciences, 53*(7), 1036-1042. doi:10.1007/s11430-010-4002-3

Gonzalez-Audicana, M., Saleta, J. L., Catalan, R. G., & Garcia, R. (2004a). Fusion of multispectral and panchromatic images using improved IHS and PCA mergers based on wavelet decomposition. *Geoscience and Remote Sensing, IEEE Transactions on, 42*(6), 1291-1299. doi:10.1109/tgrs.2004.825593

Gonzalez-Audicana, M., Saleta, J. L., Catalan, R. G., & Garcia, R. (2004b). Fusion of multispectral and panchromatic images using improved IHS and PCA mergers based on wavelet decomposition. *IEEE Transactions on Geoscience and Remote Sensing, 42*(6), 1291-1299. doi:10.1109/TGRS.2004.825593

Gonzalez, R. C., & Woods, R. E. (2002). *Digital image processing*. USA: Upper Saddle River, N.J. : Pearson/Prentice Hall

Henry, J. B., Chastanet, P., Fellah, K., & Desnos, Y. L. (2006). Envisat multi-polarized ASAR data for flood mapping. *International Journal of Remote Sensing, 27*(10), 1921-1929. doi:10.1080/01431160500486724

Hess, L. L., Melack, J. M., Filoso, S., & Yong, W. (1995). Delineation of inundated area and vegetation along the Amazon floodplain with the SIR-C synthetic aperture radar. *Geoscience and Remote Sensing, IEEE Transactions on, 33*(4), 896-904. doi:10.1109/36.406675

Hirooka, Y., Homma, K., Maki, M., & Sekiguchi, K. (2015). Applicability of synthetic aperture radar (SAR) to evaluate leaf area index (LAI) and its growth rate of rice in farmers' fields in Lao PDR. *Field Crops Research, 176*, 119-122. doi:http://dx.doi.org/10.1016/j.fcr.2015.02.022

Hong, G., Zhang, Y., & Mercer, B. (2009). A Wavelet and IHS Integration Method to Fuse High Resolution SAR with Moderate Resolution Multispectral Images. *Photogrammetric Engineering & Remote Sensing, 75*(10), 1213-1223. doi:10.14358/PERS.75.10.1213

Hope, A. S., Boynton, W. L., Stow, D. A., & Douglas, D. C. (2003). Interannual growth dynamics of vegetation in the Kuparuk River watershed, Alaska based on the Normalized Difference Vegetation Index. *International Journal of Remote Sensing, 24*(17), 3413-3425. doi:10.1080/0143116021000021170

Hossain, & Islam, M. A. (2015). Utilization of Mangrove Forest Plant: Nipa Palm (Nypa fruticans Wurmb.). *American Journal of Agriculture and Forestry, 3*(4), 156-160. doi:10.11648/j.ajaf.20150304.16

Huang, S.-q., Liu, D.-z., Gao, G.-q., & Guo, X.-j. (2009). A novel method for speckle noise reduction and ship target detection in SAR images. *Pattern Recognition, 42*(7), 1533-1542. doi:http://dx.doi.org/10.1016/j.patcog.2009.01.013

Hung, N. N., Delgado, J. M., Güntner, A., Merz, B., Bárdossy, A., & Apel, H. (2014). Sedimentation in the floodplains of the Mekong Delta, Vietnam Part II: deposition and erosion. *Hydrological Processes, 28*(7), 3145-3160. doi:10.1002/hyp.9855

Ibrahim, K., & Jusoff, K. (2009). Assessment of wetlands in Kuala Terengganu district using Landsat TM. *Journal of Geography and Geology, 1*, 33-40. doi: http://dx.doi.org/10.5539/jgg.v1n2p33

Inoue, Y., Kurosu, T., Maeno, H., Uratsuka, S., Kozu, T., Dabrowska-Zielinska, K., & Qi, J. (2002). Season-long daily measurements of multifrequency (Ka, Ku, X, C, and L) and full-polarization backscatter signatures over paddy rice field and their relationship with biological variables. *Remote Sensing of Environment, 81*(2–3), 194-204. doi:http://dx.doi.org/10.1016/S0034-4257(01)00343-1

Islam, M. A. T., P. S. Kulawardhana, R. W. Alankara, R. Gunasinghe, S. Edussriya, C.Gunawardana, A. (2008). Semi-automated methods for mapping wetlands using Landsat ETM+ and SRTM data. *International Journal of Remote Sensing, 29*(24), 7077-7106. doi:10.1080/01431160802235878

Jensen, J. R. (2005). *Introductory digital image processing: a remote sensing perspective* (3rd ed.): Upper Saddle River, N.J.: Prentice Hall.

Kaufman, Y. J., & Sendra, C. (1988). Algorithm for automatic atmospheric corrections to visible and near-IR satellite imagery. *International Journal of Remote Sensing, 9*(8), 1357-1381. doi:10.1080/01431168808954942

Kaufman, Y. J., Wald, A. E., Remer, L. A., Bo-Cai, G., Rong-Rong, L., & Flynn, L. (1997). The MODIS 2.1-μm channel-correlation with visible reflectance for use in remote sensing of aerosol. *IEEE Transactions on Geoscience and Remote Sensing, 35*(5), 1286-1298. doi:10.1109/36.628795

Kersten, P. R., Jong-Sen, L., & Ainsworth, T. L. (2005). Unsupervised classification of polarimetric synthetic aperture Radar images using fuzzy clustering and EM clustering. *IEEE Transactions on Geoscience and Remote Sensing, 43*(3), 519-527. doi:10.1109/TGRS.2004.842108

Kuenzer, C., Guo, H., Huth, J., Leinenkugel, P., Li, X., & Dech, S. (2013). Flood Mapping and Flood Dynamics of the Mekong Delta: ENVISAT-ASAR-WSM Based Time Series Analyses. *Remote Sensing, 5*(2), 687-715. Retrieved from http://www.mdpi.com/2072-4292/5/2/687

Land Law. (1993). *Land law of Vietnam 1993*.

Le, T. V. H., Nguyen, H. N., Wolanski, E., Tran, T. C., & Haruyama, S. (2007). The combined impact on the flooding in Vietnam's Mekong River delta of local man-made structures, sea level rise, and dams upstream in the river catchment. *Estuarine, Coastal and Shelf Science, 71*(1–2), 110-116. doi:http://dx.doi.org/10.1016/j.ecss.2006.08.021

Lee, J.-S. (1983). Digital image smoothing and the sigma filter. *Computer Vision, Graphics, and Image Processing, 24*(2), 255-269. doi:http://dx.doi.org/10.1016/0734-189X(83)90047-6

Liang, S., Fallah-Adl, H., Kalluri, S., JáJá, J., Kaufman, Y. J., & Townshend, J. (1997). An operational atmospheric correction algorithm for Landsat Thematic Mapper imagery over the land. *Journal of Geophysical Research, 102* 17 ,173-117 ,186. doi:10.1029/97JD00336

Liang, S., Fang, H., & Chen, M. (2001). Atmospheric correction of Landsat ETM+ land surface imagery. I. Methods. *IEEE Transactions on Geoscience and Remote Sensing, 39*(11), 2490-2498. doi:10.1109/36.964986

Lopes, A., Touzi, R., & Nezry, E. (1990). Adaptive speckle filters and scene heterogeneity. *IEEE Transactions on Geoscience and Remote Sensing, 28*(6), 992-1000. doi:10.1109/36.62623

MacAlister, C., & Mahaxay, M. (2009). Mapping wetlands in the Lower Mekong Basin for wetland resource and conservation management using Landsat ETM images and field survey data. *Journal of Environmental Management, 90,* 2130-2137.

Mallinis, G., Gitas, I. Z., Giannakopoulos, V., Maris, F., & Tsakiri-Strati, M. (2013). An object-based approach for flood area delineation in a transboundary area using ENVISAT ASAR and LANDSAT TM data. *International Journal of Digital Earth, 6*(sup2), 124-136. doi:10.1080/17538947.2011.641601

Mendoza, E. H., Santos, J. R., Rosa, A. N. C. S., & Silva, N. C. (2004). *Land use/land cover mapping in Brazilian Amazon using neural network with ASTER/Terra data*. Paper presented at the International Archives of the Photogrammetry, Remote Sensing and Spatial Information Sciences-ISPRS Archives, Melbourne, Australia.

Mitsch, W. J., Gosselink, J.G. . (2007). *Wetlands*. New Jersey: John Wiley & Sons.

Moffett, K. B., & Gorelick, S. M. (2013). Distinguishing wetland vegetation and channel features with object-based image segmentation. *International Journal of Remote Sensing, 34*(4), 1332-1354. doi:10.1080/01431161.2012.718463

MRC. (2013a). *Annual Mekong Flood Report 2013*. Retrieved from

MRC. (2013b). *Weekly flood situtation report for the Mekong River Basin-Week 7 Octorber 2013*. Retrieved from

Munyati, C. (2004). Use of Principal Component Analysis (PCA) of Remote Sensing Images in Wetland Change Detection on the Kafue Flats, Zambia. *Geocarto International, 19*(3), 11-22. doi:10.1080/10106040408542313

Nagao, M., & Matsuyama, T. (1979). Edge preserving smoothing. *Computer Graphics and Image Processing, 9*(4), 394-407. doi:http://dx.doi.org/10.1016/0146-664X(79)90102-3

Nguyen, B. D., Clauss, K., Cao, S., Naeimi, V., Kuenzer, C., & Wagner, W. (2015). Mapping Rice Seasonality in the Mekong Delta with Multi-Year Envisat ASAR WSM Data. *Remote Sensing, 7*(12). doi:10.3390/rs71215808

Nguyen, T. V. (2012). *A Land Cover Variation Model Accommodating Flood Dynamics in the Tonle Sap, Cambodia, Derived From ALOS PALSAR and Optical Data.* (Doctor of Philosophy), Yonsei University Yonsei University

Nunez, J., Otazu, X., Fors, O., Prades, A., Pala, V., & Arbiol, R. (1999). Multiresolution-based image fusion with additive wavelet decomposition. *IEEE Transactions on Geoscience and Remote Sensing, 37*(3), 1204-1211. doi:10.1109/36.763274

Nyoungui, A. N., Tonye, E., & Akono, A. (2002). Evaluation of speckle filtering and texture analysis methods for land cover classification from SAR images. *International Journal of Remote Sensing, 23*(9), 1895-1925. doi:10.1080/01431160110036157

Otsu, N. (1979). A Threshold Selection Method from Gray-Level Histograms. *Systems, Man and Cybernetics, IEEE Transactions on, 9*(1), 62-66. doi:10.1109/TSMC.1979.4310076

Ouma, Y. O., & Tateishi, R. (2006). A water index for rapid mapping of shoreline changes of five East African Rift Valley lakes: an empirical analysis using Landsat TM and ETM+ data. *International Journal of Remote Sensing, 27*(15), 3153-3181. doi:10.1080/01431160500309934

Ouyang, Z.-T., Zhang, M.-Q., Xie, X., Shen, Q., Guo, H.-Q., & Zhao, B. (2011). A comparison of pixel-based and object-oriented approaches to VHR imagery for mapping saltmarsh plants. *Ecological Informatics, 6*(2), 136-146. doi:http://dx.doi.org/10.1016/j.ecoinf.2011.01.002

Ozesmi, S. L., & Bauer, M. E. (2002). tSatellite remote sensing of wetlands. *Wetlands Ecology and Management, 10*(5), pp 381-402. doi:10.1023/A:1020908432489

Pelkey, N. W., Stoner, C. J., & Caro, T. M. (2003). Assessing habitat protection regimes in Tanzania using AVHRR NDVI composites: Comparisons at different spatial and temporal scales. *International Journal of Remote Sensing, 24*(12), 2533-2558. doi:10.1080/01431160210155929

Phan, T. M., & Jacques, P. (2007). Status and changes of mangrove forest in Mekong Delta: Case study in Tra Vinh, Vietnam. *Estuarine, Coastal and Shelf Science, 71*(1–2), 98-109. doi:http://dx.doi.org/10.1016/j.ecss.2006.08.007

Pohl, C., & Van Genderen, J. L. (1998). cReview article Multisensor image fusion in remote sensing: Concepts, methods and applications. *International Journal of Remote Sensing, 19*(5), 823-854. doi:10.1080/014311698215748

Popp, T. (1995). Correcting atmospheric masking to retrieve the spectral albedo of land surfaces from satellite measurements. *International Journal of Remote Sensing, 16*(18), 3483-3508. doi:10.1080/01431169508954642

Renaud, F. S., & Kuenzer, C. (2012). *The Mekong Delta System* (C. K. Fabrice G. Renaud Ed.): Springer Netherlands.

Richards, J. A. (2013). *Remote Sensing Digital Image Analysis*. Germany: Springer Berlin Heidelberg.

Rodrigues, S. W. P., & Souza-Filho, P. W. M. (2011). Use of Multi-Sensor Data to Identify and Map Tropical Coastal Wetlands in the Amazon of Northern Brazil. *Wetlands, 31*(1), 11-23. doi:10.1007/s13157-010-0135-6

Russi, D., Brink, P. t., Farmer, A., Badura, T., Coates, D., Förster, J., . . . Davidson, N. (2013). *The Economics of Ecosystems and Biodiversity for Water and Wetlands*. Retrieved from London, Brussels, Gland: http://www.ramsar.org/pdf/TEEB/TEEB_Water&Wetlands_Report_2013.pdf

Ryu, J.-H., Won, J.-S., & Min, K. D. (2002). Waterline extraction from Landsat TM data in a tidal flat: A case study in Gomso Bay, Korea. *Remote Sensing of Environment, 83*(3), 442-456. doi:http://dx.doi.org/10.1016/S0034-4257(02)00059-7

Sakamoto, T., Van Nguyen, N., Kotera, A., Ohno, H., Ishitsuka, N., & Yokozawa, M. (2007). Detecting temporal changes in the extent of annual flooding within the Cambodia and the Vietnamese Mekong Delta from MODIS time-series imagery. *Remote Sensing of Environment, 109*(3), 295-313. doi:http://dx.doi.org/10.1016/j.rse.2007.01.011

Secretariat, R. C. (Ed.) (2013). *The Ramsar Convention Manual: a guide to the Convention on Wetlands (Ramsar, Iran, 1971)* (6 ed.). Gland, Switzerland.

Shah, V. P., Younan, N. H., & King, R. L. (2008). An Efficient Pan-Sharpening Method via a Combined Adaptive PCA Approach and Contourlets. *IEEE Transactions on Geoscience and Remote Sensing, 46*(5), 1323-1335. doi:10.1109/TGRS.2008.916211

Sun, F., Sun, W., Chen, J., & Gong, P. (2012). Comparison and improvement of methods for identifying waterbodies in remotely sensed imagery. *International Journal of Remote Sensing, 33*(21), 6854-6875. doi:10.1080/01431161.2012.692829

Teillet, P. M., & Fedosejevs, G. (1995). On the Dark Target Approach to Atmospheric Correction of Remotely Sensed Data. *Canadian Journal of Remote Sensing, 21*(4), 374-387. doi:10.1080/07038992.1995.10855161

Thome, K., Palluconi, F., Takashima, T., & Masuda, K. (1998). Atmospheric correction of ASTER. *IEEE Transactions on Geoscience and Remote Sensing, 36*(4), 1199-1211. doi:10.1109/36.701026

Tong, P. H. S., Auda, Y., Populus, J., Aizpuru, M., Habshi, A. A., & Blasco, F. (2004). Assessment from space of mangroves evolution in the Mekong Delta, in relation to extensive shrimp farming. *International Journal of Remote Sensing, 25*(21), 4795-4812. doi:10.1080/01431160412331270858

Töyrä, J. P., Alain Martz, Lawrence W. Prowse, Terry D. (2002). A multi-sensor approach to wetland flood monitoring. *Hydrological Processes, 16*(8), 1569-1581. doi:10.1002/hyp.1021

Tran, H. N. (2005). *Assessment of impacts of dykes on the sustainabe development of Vietnam Mekong River Delta* (6049-2). Retrieved from Ho Chi Minh City:

Triet, T., R. J, S., P. Tran Duy, N. Duong Van, & Maltby, E. (2000). Wetland biodiversity overlooked and threatened in the Mekong Delta, Vietnam: Grassland ecosystems in the Ha Tien Plain. *Tropical Biodivesity, 7*, 1-24.

Trung, N. V., Choi, J.-H., & Won, J.-S. (2013). A Land Cover Variation Model of Water Level for the Floodplain of Tonle Sap, Cambodia, Derived From ALOS PALSAR and MODIS Data. *Selected Topics in Applied Earth Observations and Remote Sensing, IEEE Journal of, 6*(5), 2238-2253. doi:10.1109/JSTARS.2012.2226437

Tso, B., & Mather, P. M. (2009). *Classification Methods for Remotely Sensed Data* (2nd ed.). 6000 Broken Sound Parkway NW: Taylor & Francis Group.

Wald, L., Ranchin, T., & Mangolini, M. (1997). Fusion of satellite images of different spatial resolutions: Assessing the quality of resulting images. *Photogrammetric Engineering and Remote Sensing, 63(6)*, 691-699.

Wang, X. Y., & Bu, J. (2010). A fast and robust image segmentation using FCM with spatial information. *Digital Signal Processing, 20*(4), 1173-1182. doi:http://dx.doi.org/10.1016/j.dsp.2009.11.007

Wang, Y. (2004). Using Landsat 7 TM data acquired days after a flood event to delineate the maximum flood extent on a coastal floodplain. *International Journal of Remote Sensing, 25*(5), 959-974. doi:10.1080/0143116031000150022

Wang, Z., Song, Kaishan Ma, Wenhong Ren, Chunying Zhang, Bai Liu, Dianwei Chen, JingMing Song, Changchun. (2011). Loss and Fragmentation of Marshes in the Sanjiang Plain, Northeast China, 1954–2005. *Wetlands, 31*(5), 945-954. doi:10.1007/s13157-011-0209-0

Xu, H. (2006). Modification of normalised difference water index (NDWI) to enhance open water features in remotely sensed imagery. *International Journal of Remote Sensing, 27*(14), 3025-3033. doi:10.1080/01431160600589179

Yang, S., Shen, S., Li, B., Toan, T. L., & He, W. (2008). Rice Mapping and Monitoring Using ENVISAT ASAR Data. *Geoscience and Remote Sensing Letters, IEEE, 5*(1), 108-112. doi:10.1109/LGRS.2007.912089

Yang, Y., Liu, Y., Zhou, M., Zhang, S., Zhan, W., Sun, C., & Duan, Y. (2015). Landsat 8 OLI image based terrestrial water extraction from heterogeneous backgrounds using a reflectance homogenization approach. *Remote Sensing of Environment, 171*, 14-32. doi:http://dx.doi.org/10.1016/j.rse.2015.10.005

Zhang, J. (2010). Multi-source remote sensing data fusion: status and trends. *International Journal of Image and Data Fusion, 1*(1), 5-24. doi:10.1080/19479830903561035

Zhang, Y. (1999). A new merging method and its spectral and spatial effects. *International Journal of Remote Sensing, 20*(10), 2003-2014. doi:10.1080/014311699212317

Zhou, H. J., Hong Zhou, Guomo Song, Xiaodong Yu, Shuquan Chang, Jie Liu, Shirong Jiang, Zishan Jiang, Bo. (2010). Monitoring the change of urban wetland using high spatial resolution remote sensing data. *International Journal of Remote Sensing, 31*(7), 1717-1731. doi:10.1080/01431160902926608